FLORIDA STATE UNIVERSITY

COLLEGE OF ARTS AND SCIENCES

SEARCH FOR NEW AND UNUSUAL STRANGEONIA STATES USING $\gamma p \to p\phi\eta$ WITH GLUEX AT THOMAS JEFFERSON NATIONAL ACCELERATOR FACILITY

By

BRADFORD EMERSON CANNON

A Dissertation submitted to the
Department of Physics
in partial fulfillment of the
requirements for the degree of
Doctor of Philosophy

2017

Bradford Emerson Cannon defended this dissertation on February 19, 2019.
The members of the supervisory committee were:

Paul Eugenio

Professor Directing Dissertation

Ettore Aldrovandi

University Representative

Simon Capstick

Committee Member

Horst Wahl

Committee Member

Volker Crede

Committee Member

The Graduate School has verified and approved the above-named committee members, and certifies that the dissertation has been approved in accordance with university requirements.

Dedication goes here...

ACKNOWLEDGMENTS

This will be the last part that I will write. Let's do this later.

TABLE OF CONTENTS

LIST OF TABLES

LIST OF FIGURES

GLOSSARY OF ACRONYMS

ADC	An analog/amplitude to digital converter.
BCAL	Barrel Calorimeter.
CDC	Central Drift Chamber.
CEBAF	Continuous Electron Beam Accelerator Facility.
DIRC	Detector of Internally Reflected Cherenkov Radiation.
FCAL	Forward Calorimeter.
FDC	Forward Drift Chamber.
GEANT4	The fourth version of GEANT, which is a collection of simulation softwares designed to describe the passage of elementary particles through matter, using Monte Carlo methods.
genr8	An event generator used to generate event four-vectors
GlueX	The name of the experiment and detector located in Hall D of Jefferson Lab.
JLAB	Thomas Jefferson National Accelerator Facility.
Linac	Linear Accelerator; or the linear section of the accelerator track at JLAB.
OZI	Okubo-Zweig-Iizuka Suppression.
QCD	Quantum Chromodynamics.
PS	Pair Spectrometer.
RF	Radio Frequency. More specifically, the frequency at which the electron beam oscillates about the acclerator track.
ST	Start Counter.
TDC	Time to digital converter.
TOF	TIme of Flight detector.
TPOL	Triplet Polarimeter.

ABSTRACT

We perform an analysis dedicated to the search for new and unusual strangeonium states produced in the reaction $\gamma p \to p\phi\eta$. The data used for this analysis was recorded during the Spring 2016 physics run for Hall D of Thomas Jefferson National Accelerator Facility, where the GlueX experiment is located. The GlueX experiment uses a linearly polarized coherent bremsstrahlung beam of up to 12 GeV in energy. This photon beam will interact with a stationary liquid hydrogen target located inside the GlueX detector. The subsequent photoproduction will provide final states ideal for studying both exotic and non-exotic $s\bar{s}$ mesons.

CHAPTER 1

A BRIEF INTRODUCTION TO PARTICLE PHYSICS

1.1 Early Discoveries

One of the most important questions in all of particle physics is "what is matter made of?" That is to say, what are the fundamental building blocks for which all things are comprised of. This question dates all the way back to ancient Greece where philosophers postulated the existence of an atom; or something that is indivisible. This idea resonated throughout time, with the eventual discovery of the electron by J.J Thomson in 1897. Thomson discovered the electron by testing the properties of cathode rays, where he subjected the rays to a magnetic field. When the rays were shown to bend due to the presence of the magnetic field, it was known that the rays must be charged particles with mass. He then applied an external electric field in the opposite direction of the bent particles. Adjusting the electric field strength allowed him to measure the velocity of the particles (approximately ninety percent the speed of light) and to also measure the amount of charge per mass, e/m.

Upon measuring this quantity, Thomson realized that the particle had an e/m of $1.7\text{x}10^7$, or a quantity 1700 times that of hydrogen. This meant that the particle either had an extremely large electrical charge and similar mass in comparison to hydrogen, or the particle had similar charge and an extremely small mass. Thomson correcly determined that the particle possessed the properties of similar charge and an extremely small mass. At the time, Thomson refered to his new discovery as a 'corpuscle'; and indeed he knew that this particle of mass and charge was fundamental. "The corpuscle appear to form a part of all kinds of matter under the most diverse conditions; it seems natural therefore to regard it as one of the bricks of which atoms are built up." [36]. Joseph John Thomson would eventually win the 1906 Nobel Prize in Physics for "recognition of the great merits of his theoretical and experimental investigations on the conduction of electricity by gases".

The mysteries surrounding the nature of matter were no where near settled, however. If Thomson was correct in that electrons were everywhere in nature, then why was so much ordinary matter

electrically neutral? Thomson attempted to explain this phenomena with his famous 'plum pudding' model. In his plum pudding model he envisioned the electrons were attached to a paste that was electrically positive, but with no internal structure. This hypothesis would eventually be shown inaccurate by Ernest Rutherford's gold foil experiment. Rutherford conducted this experiment by shooting charged helium particles towards a stationary sheet of gold foil. The idea of the experiment was simple. If matter is made of pudding as Thomson suggested, then the helium particle will pass through the gold foil slightly perturbed, but in no way greatly deviated from its original direction of motion. However, Rutherford discovered the exact opposite. Most of the time the helium passed through the gold foil completely unscathed. Yet, a small fraction of interactions showed the helium deflecting off of the gold foil at large angles. These discoveries provided a number of interesting insights. First off, that matter was most certainly not made of a paste or a pudding; but instead matter was comprised of compact and heavy objects with vast amount of empty space between them. Additionally, since Thomson had shown that the electron had to be extremely light, it must be the case that the helium particles were bouncing off of an entirely different particle of mass; what Rutherford postulated as the proton.

But the proton could not be the final answer to everything that existed inside the nucleus. The structure of organized matter still had one last void to fill which was now the problem of the periodic table of the elements. Considering the first three elements, we know that hydrogen has one proton and one electron. The next element is Helium, which is four times the weight of the proton, but only has two electrons. Then there is Lithium, seven times larger that the proton but only has three electrons. If each fundamental element in nature has an electron that matches a proton to make it electrically neutral, then why are the masses of the elements not equal to the number of electrons or protons inside the nucleus? This question would be answered in 1932 by the physicist James Chadwick. Chadwick had a similar experimental setup as Rutherford - firing Helium particles towards a stationary target; only this time the target was Berillium. The interaction of the Helium beam with the Berillium target subsequently produced a Carbon-12 and some electrically neutral radiation. Using kinematics and the conservation of momentum, Chadwick was able to determine that the mass of the electrically neutral radiation was almost exactly the same as that of a proton. He would eventually win the 1935 Nobel Prize in physics for his discovery of the neutron. [12]

Once the neutron had been discovered, many physicist believed that all of matter was organized with three fundamental particles - the proton, the neutron and the electron. However, there were still some questions that had not been answered about organized matter such as 'how protons and neutrons remain in a bound state inside the nucleus'? The first significant theory to describe the bound states of protons and neutrons was done by Hideki Yukawa in 1934 where he postulated the existence of a particle that had a mass between the proton and the electron which he named the pion. The pion would eventually be discovered but not without confusion. Multiple charged particles with masses between the proton and electron had been observed in experimentation, especially with cosmic rays. The amount of charged and neutral particles with masses between the proton and electron continued to grow to an absurd amount. This led physicists to wonder if there were different fundamental building blocks of matter other than the proton, the neutron, and the electron. [14]

1.2 The Standard Model of Particle Physics

To date, there are only a handful of what physicists would label as 'fundamental particles'. We typically organize these particles into groups depending on the properties that they possess. The first group of fundamental particles that will be discussed are the neutrinos. Currently there are three species of neutrinos - the electron neutrino, the muon neutrino, and the tau neutrino; or ν_e, ν_μ, and ν_τ, respectively. For each neutrino there exists a corresponding antineutrino as well ($\bar{\nu}_e$, $\bar{\nu}_\mu$, and $\bar{\nu}_\tau$). Neutrinos are unique particles due to the fact that they have no electromagnetic charge, have an extremely small mass, and they can only interact by means of the weak nuclear force. Neutrinos can also oscillate between the three different *flavor* states mentioned above and have an interesting history in the realm of particle physics. However, in order to keep this discussion short, we will not delve into those details.

You may have thought the names of the neutrino species listed above as somewhat random; but in fact, they are not. These names are chosen because they couple to a group of three more particles, all of which share the same names - the electron, the muon, and the tau; or e, μ, and τ, respectively. Just like the neutrinos, these particles all have associated antiparticles ($\bar{e}$, $\bar{\mu}$, and $\bar{\tau}$). The differences between this set of particles and the neutrinos is the fact that they all have much higher masses in comparison to neutrinos, they all possess one unit of negative electromagnetic

charge, and can therefore interact both weakly and electromagnetically. All six of these particles and their associated antiparticles are classified as *leptons* or 'light weights'.

The next set of particles that I would like to discuss are the most important particles for the subject of this thesis: the quarks. Just like the leptons, there are six quarks with mass, electromagnetic charge, and they all have corresponding anti particles as well. There are six *flavors* of quarks: up, down, charm, strange, top, bottom; or u, d, c, s, t, b. You may notice that the names are grouped in pairs of names that seem to be opposite of one another. This naming scheme has some historical significance, but the most important thing to take away is that the 'up' quarks (u,c,t) have a positive electromagnetic charge of +2/3, and the 'down' quarks (d,s,b) have a negative electromagnetic charge of -1/3. Lastly, the quarks can interact by means of three different forces: the weak nuclear force, the electromagnetic force, and the strong nuclear force.

All of the aforementioned quarks and leptons have one very important characteristic in common between them and that is the fact that they are all spin 1/2 particles or *fermions*. There are other fundamental particles that exist which are not fermions. These particles are referred to as *gauge bosons*, or spin 1 particles. All of these particles are described as 'mediators' since they are the particles responsible for communicating force between other fermions. There are currently four mediators known at this time - the W and Z bosons, the photon, and the gluon. The W and Z gauge bosons are the only particles with mass and are responsible for mediating the weak nuclear force. There are two W bosons, one that has a positive electromagnetic charge and one that has a negative electromagnetic charge. There is only one Z boson and that simply has a neutral electromagnetic charge. Since the Z and W bosons mediate the weak nuclear force, they can interact with all of the fermions mentioned in the previous paragraphs. The photon is the most well known of the four gauge bosons and is responsible for mediating the electromagnetic force. Unlike the W bosons, the photon has no mass or electromagnetic charge and can interact with all of the fermions mentioned before except the neutrinos (because they have no electromagnetic charge). Lastly there is the gluon, which much like the photon, has no mass or electromagnetic charge. However, the gluon is special in that it has a charge that is not completely obvious. We call this the *color* charge and it is the way that we explain the interaction of the strong nuclear force between quarks and gluons in the Standard Model. The gluon is special because it does not interact with any of the fermions except for the quarks.

There is one last particle which is the Higgs Boson. The Higgs may sound familiar to the reader due to its recent dicovery on July 4th, 2012 [26]. Although this particle is arguably the most important discovery in particle physics for quite some time, we will not go into details about its nature here. All that the reader needs to know is that it is the particle responsible for giving mass to all of the fundamental particles. Having said this, all of the previously mentioned particles are parts to something that we like to call The Standard Model of Particle Physics. A depiction of these particles in a nicely organized fashion is given in Figure 1.1 below.

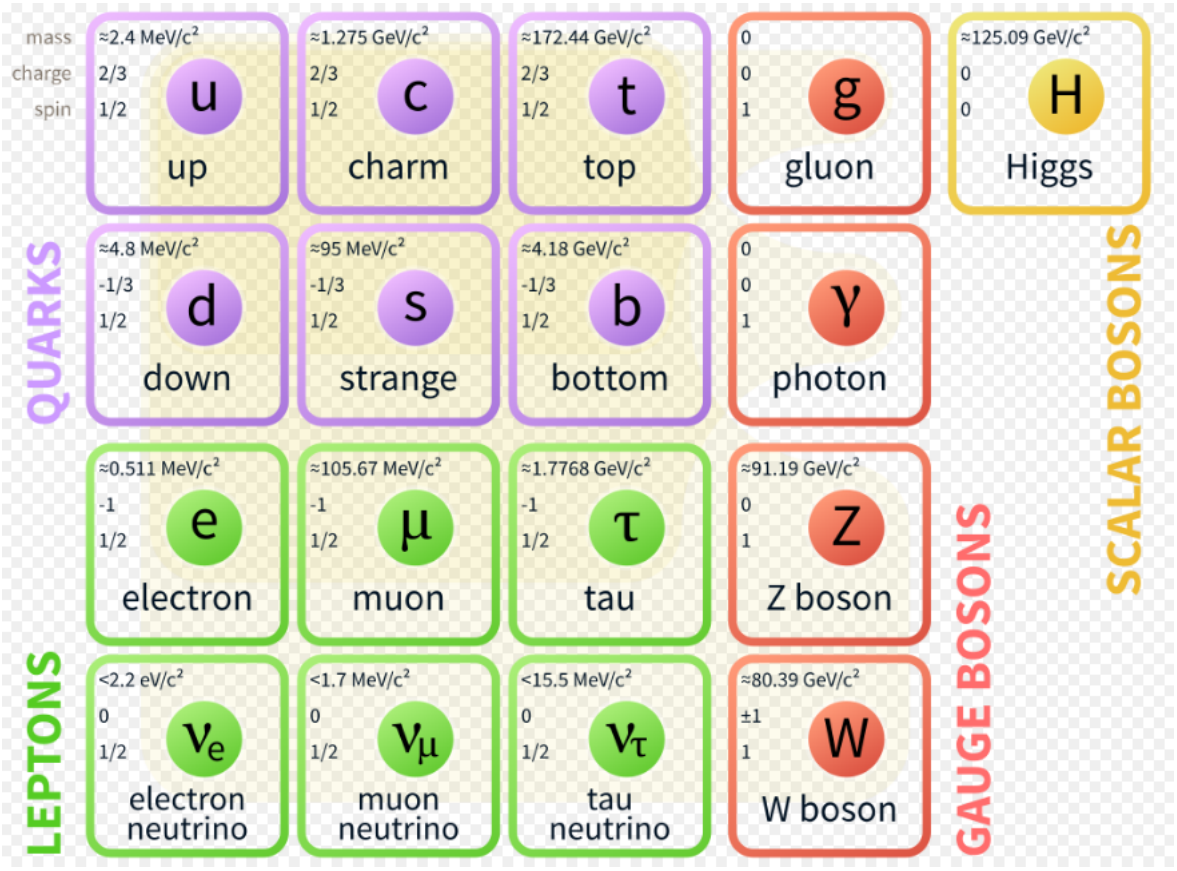

Figure 1.1: An illustration of The Standard Model of Particle Physics. The bottom left (green) boxes contain the six flavors of leptons, and the top left (purple) boxes contain the six flavors of quarks. The middle vertical column (red) displays all of the gauge bosons or mediators in the same row as the particles with which they interact. The far right box (yellow) box contains the Higgs Boson.

1.3 Meson Spectroscopy

We spent a great deal of time describing what we know as the fundamental building blocks of nature in the previous section. However, one thing that I did not mention was that quarks cannot exist individually in nature. That is to say, it is impossible to observe a single quark by its self, it must be in some type of bound state. So the next question that I would like to address is how exactly these quarks can combine to create the plethora of particles that we can observe in out every day world.

To date, there are only two ways that quarks can exist inside bound states. One of the ways that they can combine is in groups of three, with three quarks (qqq) or three antiquarks ($\bar{q}\bar{q}\bar{q}$). These groups of three quarks are called *baryons* or 'heavy weights'; and they are called *antibaryons* when they have three antiquarks. Two well known examples of baryons are protons and neutrons where the proton is comprised of two up quarks and one down quark (uud) and the neutron is comprised of one up quark and two down quarks (udd). It should be easy enough to realize then that the anti proton and anti neutron have the same composition except all of the quarks are antiquarks ($\bar{u}\bar{u}\bar{d}, \bar{u}\bar{d}\bar{d}$). The second way that quarks can exist inside a bound state is when they combine in groups of two, where one is a quark and the other is an antiquark, or $q\bar{q}$. These composite particles are given the name *mesons*, or 'middle weights'. Since there are six quarks and two different primary ways in which they can organize with both matter and antimatter, one quickly realizes that there is an abundant amount of possible hadronic combinations. A fair question that one may have is 'how do particle physicists organize baryons and mesons into groups?'

This question would eventually be answered with the creation of the Eightfold Way by Murray Gell-Mann circa 1961 [13]. Gell-Man introduced a way of organizing all of the known mesons and baryons into groups that shared patterns of strangeness, charge, and isospin. These diagrams helped to show that hadronic matter is comprised of six different quarks and antiquarks which are held together by their interaction via the strong nuclear force. Examples of baryon and meson multiplets are depicted in Figure 1.2 below [30].

The strong nuclear force is described by Quantum Chromodynamics (QCD), which is a theory that predicts the behaviour of particles and their coupling to the color field. These particles include all quarks, antiquarks, and gluons which are the quantized mediators of the strong force. When a quark and an antiquark are in a bound state (ie - a meson) their individual quantum numbers

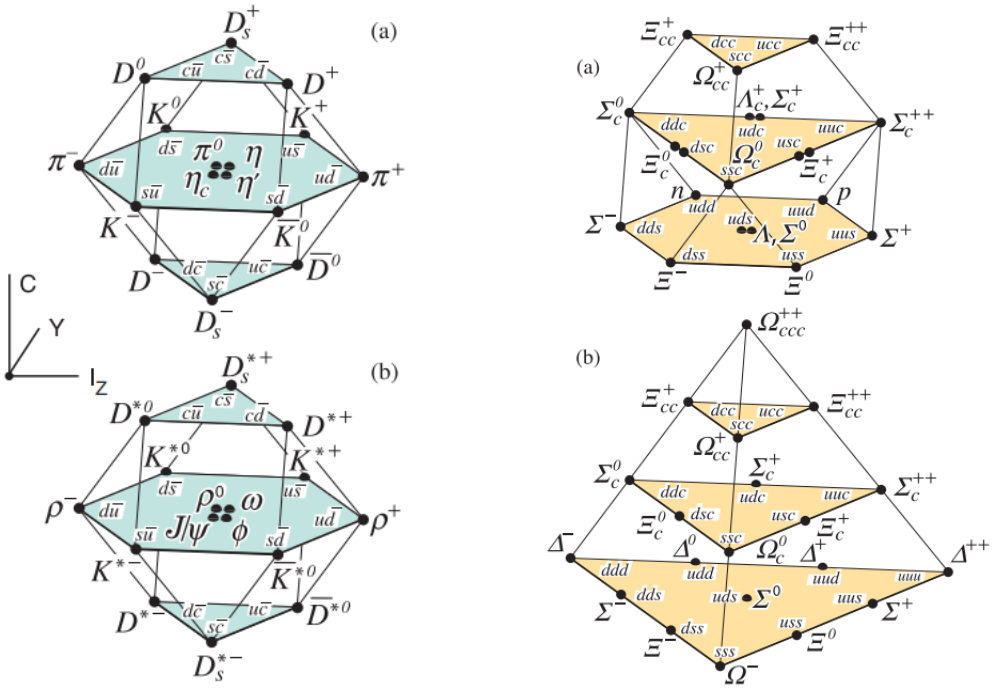

Figure 1.2: (upper-left) $J^{PC} = 0^{-+}$ pseudoscalar meson multiplet. (upper-right) $J^{PC} = 1/2^{+}$ baryon multiplet. (lower-left) $J^{PC} = 1^{--}$ vector meson multiplet. (lower-right) $J^{PC} = 3/2^{+}$ baryon multiplet

combine to make a total bound state with a given J^{PC}; where J is the quantum number for total angular momentum, P is the quantum number for parity, and C is the quantum number for charge conjugation. Knowing that quarks and antiquarks are fermions and therefore have 1/2 spins, it is easy to investigate the allowed quantum mecanical bound states of all $q\bar{q}$ mesons, regardless of their quark antiquark flavor combination. A list of good quantum numbers for all mesons is given below in Table 1.1. If you take a closer look at the resulting J^{PC} states in Table 1.1, you should notice that certain states are missing; such as 0^{--}, 0^{+-}, 1^{-+}, and 2^{+-}. These states are known as *exotic* J^{PC} meson states, or exotic quantum number states. In addition to exotic quantum number sates of mesons, QCD allows other exotic states such as $q\bar{q}q\bar{q}$ (four quark), $qqqq\bar{q}$ (pentaquark), and $q\bar{q}g$ (gluonically excited meson). Interestingly, some experiments have observed structures which resembles some of these exotic states [33]. However, more evidence needs to be provided in order to identify these resonances as undisputed exotic states. Having said that, the primary goal of the GlueX experiment is to unambiguously map all light quark exotic meson multiplets. Discussion of

Table 1.1: List of good quantum numbers for mesons, where s represents the spin of the meson and l represents the relative orbital angular momentum between the quark and antiquark. $Constraints$: $|l-s| <= J <= |l+s|, P = (-1)^{l+1}, C = (-1)^{l+s}$

s	$l=0$	$l=1$	$l=2$
$s=0$	0^{-+}	1^{+-}	2^{-+}
$s=1$	1^{--}	0^{++},1^{++},2^{++}	1^{--},2^{--},3^{--}

the GlueX experiment will be presented in Chapter 2.

1.4 Motivation

At this point in history, there are no universally accepted non $q\bar{q}$ meson states; only observed exotic meson candidates. The primary reason for this is the absence of an established $q\bar{q}g$ nonet. The purpose of the GlueX experiment at Jefferson Lab is to unambiguously map exotic meson states. In order to establish exotic nonets, we need to first understand non exotic meson states. An example of a non exotic state that is poorly understood is $s\bar{s}$, or *strangeonia*. Out of the twenty-two expected $s\bar{s}$ resonances below 2.2 GeV, only seven probable resonances exist : $\eta\eta'$, $\phi(1020)$, $h_1(1386)$, $f_1(1426)$, $f_2'(1525)$, $\phi(1680)$, and $\phi_3(1386)$; where $\eta\eta'$ is counted as one resonance [19]. Of these seven resonances, only three of them are considered pure $s\bar{s}$ states - $\phi(1020)$ $f_2'(1525)$, and $\phi_3(1386)$. Due to the heavy nature of the strange quark in comparison to the up and down quarks, one would expect more pure $s\bar{s}$ states to exist in nature. Historically, there has been some controversy over the identification of $s\bar{s}$ states in the 1600-2200 MeV mass range; specifically the $\phi(1680)$, the $X(1750)$, and the $Y(2175)$ meson states.

1.4.1 $\phi(1680)$

The first observation of $\phi(1680)$ came from the DM1 collaboration at DCI in 1981. The experiment analysed the $K_s^o K_L^o$ final state and observed a small enhancement in the cross section between 1.6-1.8 GeV center of mass energy [25]. Research on the $\phi(1680)$ continued to be done by many collaborations [30], however there is one particular study that stands out due its large sampling of statistics and the fact that it includes $\phi\eta$ as a final state topology. In 2008, the BABAR collaboration published a study containing many different topologies arising from electron-positron

annihilation; most notably: $e^+e^- \to KK^*(892)$ and $e^+e^- \to \phi\eta$. The $KK^*(892)$ signal was studied by means of a Dalitz plot analysis and then showing the isovector and isoscalar components of the cross section (Figure 1.3d), as well as the phase difference plot between the two components (Figure 1.3c). The results strongly suggested that an isoscalar resonance exists at 1.7 GeV/c in the center of mass frame. The paper also provided an invariant mass plot (Figure **??**) and a measured cross section (Figure 1.3b) of the $K_sK\pi$ final state, which was the final state of the $KK^*(892)$ parent state. Once again, both plots provided evidence of a resonance at 1.7 GeV/c.

The $\phi\eta$ analysis provided far fewer statistics in comparison to the $K_sK\pi$ final state. However, the same plots were shown and provided the same conclusion (Figures 1.3e and 1.3f). Furthermore, since the resonance was thought to be an isoscaler that decayed to $\phi\eta$ and $K_sK\pi$, it was concluded that the parent state must have been $s\bar{s}$; more specifially, the radially excited version of the $\phi(1020)$. This enhancement was eventually observed to have a dominant decay into a neutral KK^* final state. An odd feature of the $\phi(1680)$ is that it has only been observed in electron-positron annihilation experiments, and has never been observed in photoproduction [18].

1.4.2 X(1750)

Six months after the discovery of the $\phi(1680)$, the X(1750) meson was observed by the Omega Photon collaboration at CERN [23]. The experiment analysed a K^+K^- final state from photoproduction and found an enhancement in the invariant mass spectrum of the K^+K^- pair. To be clear, the statistics of this study were very low and only produced 100 events in the peak region. The same collaboration produced another paper four years later which provided many more statistics and a matching result [31]. A clear resonance at 1760 MeV/c was observed, however the spin and parity of this state were not well described by angular distributions and therefore could not be confirmed as the radially excited version of the $\phi(1020)$. Significant evidence would eventually become available in the year 2002, when the FOCUS collaboration performed another photoproduction study on a K^+K^- final state [29]. There were three significant findings from this analysis, the first being an observation of a resonance after performing a transverse momentum cut on the K^+K^- system (Figure 1.4a). Second, a study was performed on the same final state as BaBar ($K_sK\pi$) where no significant resonances were found in any invariant mass spectra (Figure 1.4b). Finally, using these two results, branching ratios of $X(1750) \to K^*K$ were compared to $X(1750) \to K^+K^-$.

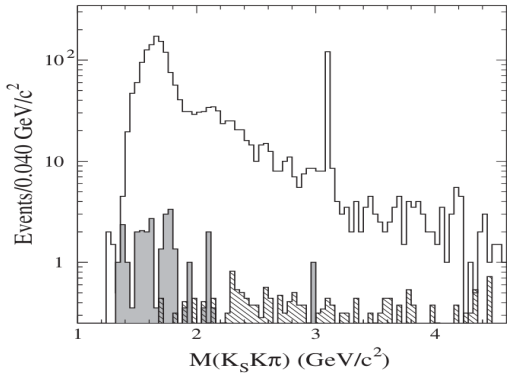

(a) Invariant Mass Spectrum for the $K_sK\pi$ final state.

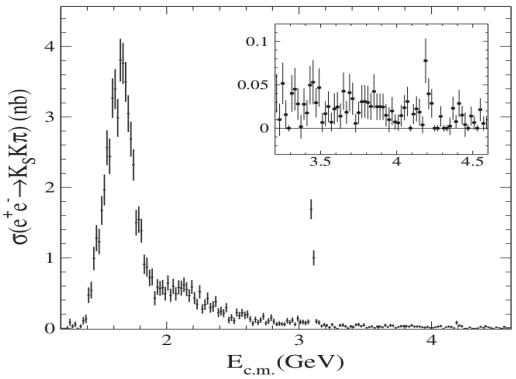

(b) Measured cross section for the $K_sK\pi$ final state.

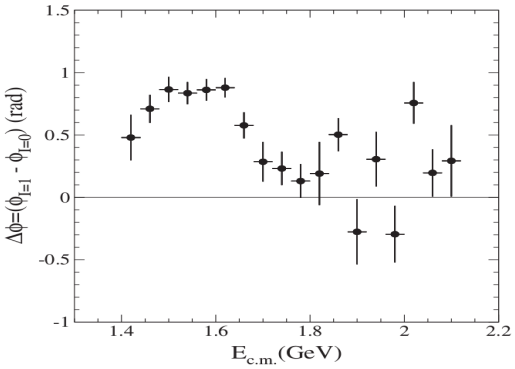

(c) Relative phase difference between the isoscalar and isovector components of the $KK^*(892)$ final state.

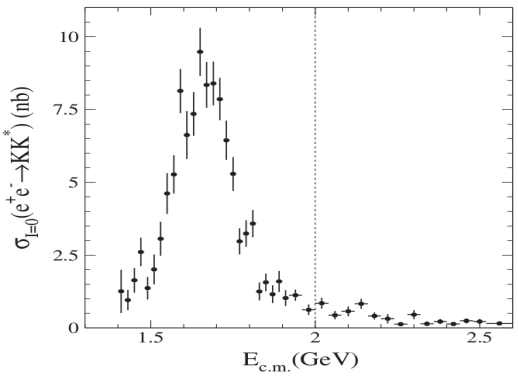

(d) Measured cross section of the isoscalar component of the $KK^*(892)$ final state.

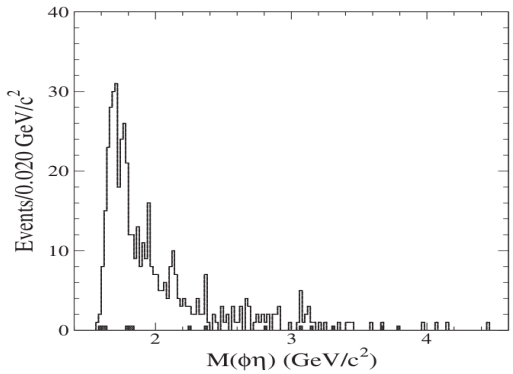

(e) Invariant mass spectrum for the $\phi\eta$ final state.

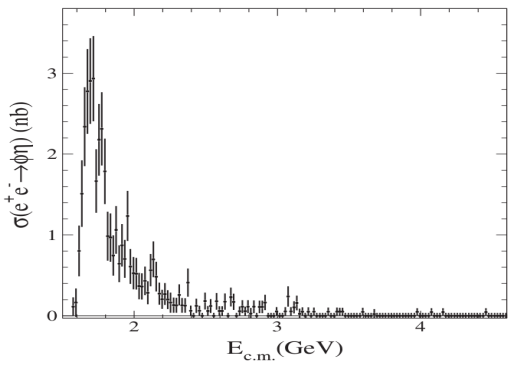

(f) Measured cross section for the $\phi\eta$ final state.

Figure 1.3: Highlighted results from the BaBar detector and collaboration where there is significant evience to suggest that a $\phi(1680)$ has been observed from both $KK^*(892)$ and $\phi\eta$ final states by means of electron positron annihilation. [21]

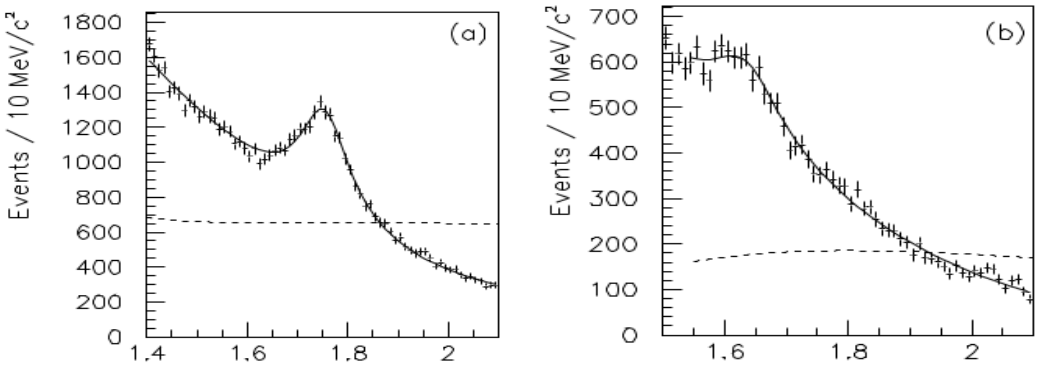

(a) Invariant Mass Spectrum for the K^+K^- final state after transverse momentum cut.

(b) Invariant Mass Spectrum for the K^*K final state after transverse momentum cut.

Figure 1.4: Highlighted results from the FOCUS collaboration where there is significant evience to suggest that an $X(1750)$ has been observed in the K^+K^- invariant mass sepctrum. Additionally, no resonance if found inside the K^*K invariant mass speactrum. [29]

It was found that these ratios were both less that 0.183 with a 90 percent confidence level. The observation of the $X(1750)$ raises many questions and a lot of confusion. In all likelihood, the $\phi(1680)$ probably is the radially excited form of the $\phi(1680)$ since the masses of the other radially excited vector mesons are $\omega(1650)$ and $\rho(1700)$. However, it is a complete mystery as to why the $\phi(1680)$ is seen so clearly in electron positron annihilation with no sign of a resonance at 1750 MeV/c; yet we see a clear $X(1750)$ resonance from photoproduction and observable structure near 1680 MeV/c. To quote the final line from the FOCUS publication "The interpretation of the $X(1750)$ remains uncertain".

1.4.3 Y(2175)

Lastly, the BaBar collaboration at SLAC discovered a structure at 2175 MeV/c in the reaction $e^+e^- \rightarrow \phi f_0(980) \rightarrow K^+K^-\pi\pi$ [22]. Since the $f_0(980)$ decays to a neutral and charged pion final state, both the $\pi^+\pi^-$ and $\pi^0\pi^0$ topologies were studied in the analysis. In each instance, a resonance was obseved inside the cross sections of the charged and neutral final states. Additionally, the $K^+K^-\pi^{\pm,0}\pi^{\mp,0}$ final state invariant mass distributions showed a clear enhancement around 2175 MeV/c. Due to the fact that the structure came from the $\phi f_0(980)$ intermediate state, one can easily deduce that the parent state is both isosiglet and has quantum numbers equivalent to 1^{--}. Furthermore, it has been suggested that this resonance may be a four quark strageonium

hybrid state for serveral reasons. One of the reasons is the fact that no isosinglet vector mesons have been seen to have an invariant mass this large. A second reason is the possibility that this state is analgous to the $Y(4260)$ state which is belived to be either a $c\bar{c}g$ or $cs\bar{c}\bar{s}$ exotic state. It follows naturally that the $Y(2175)$ could either be an $s\bar{s}g$ or an $ss\bar{s}\bar{s}$ exotic state. What makes this resonance even more enticing for this dissertation is that its quantum numbers forbid decay into $\eta\eta^{'}$, $\eta^{'}\eta^{'}$, and $\phi\phi$ final states due to C-parity and G-partiy violations. However, the $\phi\eta$ and $\phi\eta^{'}$ final states are quantum mechanically allowed. Assuming the $Y(2175)$ is a four quark $ss\bar{s}\bar{s}$ resonance, many theoretical models view this bound state as an ss $\bar{s}\bar{s}$ 'diquark' molecule. If this is true, then the primary decays of the $Y(2175)$ should be to the $\phi\eta$ and $\phi\eta^{'}$ final states [27].

The underlying issue with all of the observations previously described is that the production of final state kaons does not necessarily confirm the existence of an $s\bar{s}$ state. The observation of the $Y(2175)$ may be evidence of an $s\bar{s}$ exotic state. However, this cannot be officially resolved due to the fact that the valence quarks and gluons for the $f_0(980)$ are not known or well understood. Therefore, the only way to ensure that a state has $s\bar{s}$ content is to choose an intermediate state in which the parent $u\bar{u}$ / $d\bar{d}$ content is suppressed. One channel that will resolve this ambiguity is $\phi\eta$. If a state is shown to have a significant branching fraction to $\phi\eta$, it will be good evidence that the state is an $s\bar{s}$ state. Furthermore, if a state is not seen in the $\phi\eta$ channel, it will be good evidence that the state has little to no $s\bar{s}$ content. The reason for this will be described in more detail below.

1.5 Proposed Analysis

The purpose of this research is to accomplish at least one out of two goals. The first is to provide a spectrum of excited $s\bar{s}$ states using the $\phi\eta$ channel. The $\phi\eta$ channel is a unique final state to study because it can only be produced from a parent state that is dominantly comprised of $s\bar{s}$ quarks. The reason for this is due to a few different characteristics of the $\phi\eta$ final state. One characteristic is due to the fact that the ϕ meson is almost pure $s\bar{s}$, and that the η meson has a super position of $u\bar{u}$, $d\bar{d}$, and $s\bar{s}$ quark content. Since quark flavor is conserved in hadronic decays, having a strange and anti-strange particle in the final state is an absolute must. Another characteristic that makes $\phi\eta$ a desirable channel to study is because the daughter states are both isosinglet and relatively light in mass. The conservation of isospin in strong decays ensures that the parent state

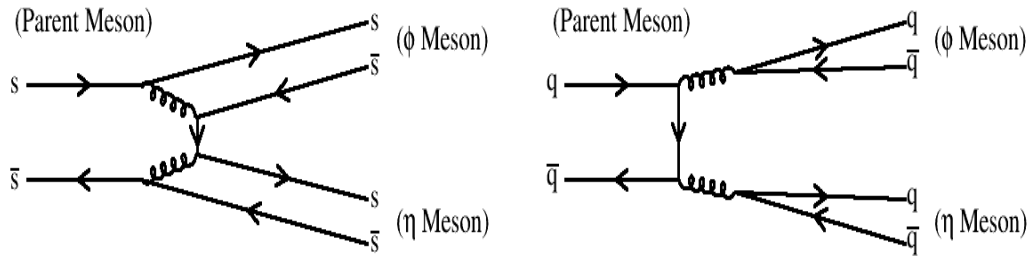

(a) Feynman Diagram for OZI allowed process.

(b) Feynman Diagram for OZI forbidden process.

Figure 1.5: (Figure 1.5a) Feynman Diagram depicting the decay of a parent $s\bar{s}$ state into $\phi\eta$ strangeonia. (Figure 1.5b) Feynman Diagram depicting the decay of an arbitrary $q\bar{q}$ parent state into $\phi\eta$ quarkonia.

of an exclusive $\gamma p \to p\phi\eta$ reaction must be isosinglet as well. The last characteristic is that the $\phi\eta$ channel is Okubo-Zweig-Iizuka (OZI) suppressed from $u\bar{u}$ and $d\bar{d}$ final states. To describe it briefly, OZI suppression exists in nature when a quark and anti-quark bound state annihilate to produce gluons. The subsequent gluons then hadronize into pairs of flavorless $q\bar{q}$ mesons.

OZI suppression is known to exist in particle physics due to two major mesonic examples; the branching fraction of $\phi(1020) \to \pi^+\pi^-\pi^0$ and the lifetime of the J/ψ. As we now know, the $\phi(1020)$ is an $s\bar{s}$ bound state. Since pions only contain up and down quarks, the $s\bar{s}$ pair would have to annihilate in order to create a three pion final state; thus making a low branching fraction due to OZI suppression. The J/ψ has an abnormally long lifetime beause it's mass is too low to decay into a pair of D mesons. Since the only remaining particles to decay into are leptons or hadrons with up down and strange quarks, the J/ψ decay is OZI suppressed, giving it a longer lifetime. Example Feynman diagrams for $s\bar{s}$ and OZI suppressed hadronic decays into $\phi\eta$ final states are given in Figure 1.5 [17] [37] [15].

As previously stated, an observation of a parent state that has a large branching fraction to $\phi\eta$ will be good evidence of a dominant $s\bar{s}$ excited state. Conversely, if there is an absence of a state in $\phi\eta$, it should have little to no $s\bar{s}$ content. Understanding and establishing dominant $s\bar{s}$ states is an important aspect to meson spectroscopy because there are only three well known states to date; the $\phi(1020)$, the $f_2'(1525)$, and the $\phi_3(1854)$. The second goal of this research will be to search for

Table 1.2: List of good quantum numbers (J^{PC}) for the parent stare of $\phi\eta$, where l represents the relative orbital angular momentum between the ϕ meson and the η meson.

l	J^{PC}
$l = 0$	1^{+-}
$l = 1$	0^{--}, 1^{--}, 2^{--}
$l = 2$	1^{+-}, 2^{+-}, 3^{+-}

exotic mesons using the $\phi\eta$ channel. Knowing that the ϕ meson has $J^{PC} = 1^{--}$, and that the η meson has $J^{PC} = 0^{-+}$, it is easy to derive what parent states can produce $\phi\eta$ with different relative angular momentum. A table of possible parent states is given in Table 1.2.

There are three states in Table 1.2 that are of particular interest, the most obvious being the 0^{--} and the 2^{+-} quantum states since they are inherently J^{PC} exotic for mesons. The other state of interest is the 2^{--} since it is not well understood for $s\bar{s}$ bound states [30].

CHAPTER 2

GLUEX

The data in this thesis came from the Spring 2017 run period which was recorded by the GlueX experiment located at Thomas Jefferson National Accelerator Facility in Newport News, Virginia (Figure 2.1). The Spring 2017 run started on January 23rd, 2017 and ended on March 13th 2017. The conditions for this run were fairly stable and the only major change was increasing the beam current by 50% on February 24th, 2017. The run consisted of five different radiator settings including an amorphous radiator, and four different diamond radiator orientations. The four different diamond radiator orientations included an angle of 0°, 45°, 90°, and 135° relative to the lab floor. There were two reasons for choosing these four different diamond orientations. The first reason is that we need to have a set of data which is perpendicular in photon polarization relative to another set of data. Therefore, the data set which was measured at 0° is perpendicular to the data set which was measured at 90°. Similarly, the 45° data set is perpendicular to the 135° data set. The second reason for choosing four different diamond orientations was to make sure the acceptance inside the spectrometer remained the same for different photon polarization angles.

Over the course of the entire Spring 2017 run, there were $10.4x10^9$ physics triggers recorded for the 0° diamond orientation, $11.0x10^9$ physics triggers recorded for the 90° diamond orientation, $10.0x10^9$ physics triggers recorded for the 45° diamond orientation, $10.2x10^9$ physics triggers recorded for the 135° diamond orientation, and $8.0x10^9$ physics triggers recorded for the amorphous radiator. Therefore, a total of 50 billion physics triggers were recorded for the Spring 2017 run, resulting in 120 TB of reconstructed event files. In addition, data was written at a rate of roughly 50 kHz for the diamond and amorphous radiators. The run conditions were initially set to a "low intensity" beam current of 100 nA for the diamond radiator, and 150 nA for the amorphous radiator. As previously mentioned, the beam current was then increased to 150 nA for the diamond radiator and 200 nA for the amorphous radiator. For the entirety of this run, a 5 mm collimator hole was used for the beam line and a 75 μm Beryllium converter was used to measure photon polarization. As of this date, the Spring 2017 run is the most successful reconstructed physics run

period for GlueX. It should be noted, however, that the Spring 2018 run should have even more statistics once the data is reconstructed an analyzed.

Figure 2.1: A picture taken from inside Hall D. From this angle, the photon beam would be coming towards the viewer, and eventually interact with the liquid hydrogen target located inside the apparatus. One can easily identify the shell of the superconducting barrel shaped solenoid as well as the back side of the forward calorimeter and some photomulitplier tubes attached to the time of flight detector. [8]

2.1 Jefferson Lab

Thomas Jefferson National Accelerator Facility (JLab) is a U.S. Department of Energy Office of Science national laboratory which contains 1,500 scientists from 30 different countries and a total of 230 institutions world wide (Figure 2.2). The lab has also completed nearly 200 experiments from all of its halls (not counting the new Hall D) and has graduated more than 500 Ph.D's due to the exceptional research conducted there. The primary mission of JLab is to understand the atomic nucleus by utilizing the Continuous Electron Beam Accelerator Facility (CEBAF) and the four experimental halls which receive it's electrons. In addition, JLab also contains advanced computing resources, theoretical, and applied research which will help to educate future generations of scientists. The lab recently received over three hundred million dollars to upgrade the CEBAF from 4 GeV to 12 GeV in energy. The upgrade included many new features of the CEBAF such

as ten new superconducting radio-frequency (SRF) accelerating elements; or five per linear section of the accelerator. There were also ten new RF stations to power the 10 new cryomodules (SRF) which required doubling the refrigeration capacity at JLab. Modifications to the magnets in the recirculation arcs and their power supplies were also an obvious necessity in order to keep the higher energy beam confined to the existing beam path. There was also a tenth magnetic arc added to the curved section of the CEBAF. This extra arc allows us to send beam towards the north linac which will then boost the electron beam to 12 GeV, the amount necessary to accommodate the experimental program in Hall D. All in all, this upgrade will allow scientists and researches at Jefferson Lab to explore a greater amount of detail that may be hidden within the atomic nucleus. This upgrade was also coupled with the construction and creation of a new experimental Hall D, which houses the GlueX experiment and is the ultimate source for the data contained within this thesis [9].

Figure 2.2: A picture taken of the Thomas Jefferson National Accelerator Facility (JLab) in Newport News, Virginia. In this picture, the electron beam from the Continuous Electron Beam Accelerator Facility (CEBAF) will travel in a clockwise motion. The two linear accelerator sections of the CEBAF are near the two parallel lab roads which run towards and away from the picture view. Three circular grass mounds can be observed in the lower part of this picture which represent the locations of Hall A, Hall B, and Hall C. Hall D is located diagonally across the CEBAF from those three halls and somewhat visible in this picture. [8]

2.2 CEBAF

CEBAF is an acronym which stands for Continuous Electron Beam Accelerator Facility (Figure 2.3). The beam is created by shining laser light onto a gallium-arsenide wafer that is roughly the size of a postage stamp. The laser light forces the bound electrons to fly off of the surface of the wafer and towards magnets which confine the electrons into a stream of particles the width of a

human hair. These electrons are then passed into the linear accelerator region of the CEBAF. The linear accelerator contains a series of accelerator cavities called Radio Frequency (RF) cavities which are responsible for increasing the energy and momentum of the electron beam. These cavities are superconducting and therefore cooled by a central helium liquefier which contains approximately 16,500 gallons of liquid helium and also keeps the RF cavities at -456 degrees Fahrenheit, or 2 degrees Kelvin. Attached to the two linear accelerator regions of the CEBAF are two arc regions. These arc regions contain large magnets responsible for steering and focusing the electron beam between the two linear accelerators. In total, the CEBAF is 7/8 of a mile in distance, or 1400 meters long and is 25 feet below ground. The accelerator tunnel itself is 13.5 feet wide and 10 ft tall with 2 feet of concrete for its walls. Electrons travel through the straight section of the track up to 5.5 times which allow them to obtain energies as high as 11.5 GeV for Halls A, B, and C; and up to 12 GeV for Hall D. The CEBAF can also deliver beam to all four of the experimental halls simultaneously, allowing a wide variety of research to be done in concurrently at Jefferson Lab. [1]

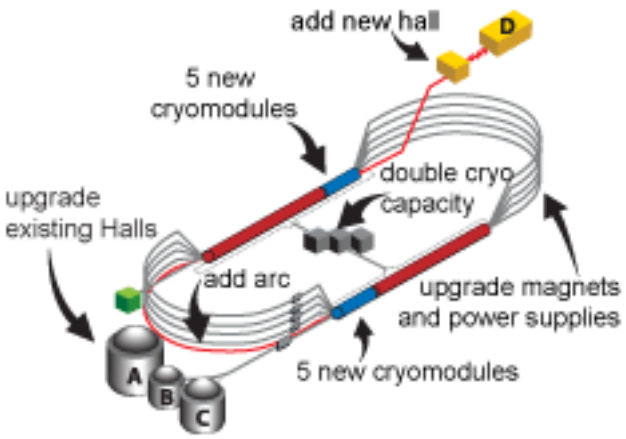

Figure 2.3: An illustration of the 12 GeV CEBAF upgrade at Jefferson Lab. This depiction shows where many of the aforementioned upgrades were physically placed within CEBAF and JLab. [8]

2.2.1 Injector

The CEBAF injector is a unique piece of equipment because it provides beam to the main accelerator at JLab while having to work in sync with two recirculating linear accelerators operating at 1497 MHz. The beam can be delivered to each experimental hall at 499 MHz, one third of the

linear accelerators frequency. This allows simultaneous operation of three halls at JLab; where the three beams are typically at 499 MHz with 120 degrees phase separation. Figure 2.4 shows the general layout of the injector [34]. The beam is created by using one of the 100 keV photo cathodes, the other gun being a hot spare. The next element in the injector is the pre-buncher cavity, followed by emittance limiting apertures A1, A2, and then the three beam chopper system. The three beam chopper system is in charge of initial timing and longitudinal structure of the beam. Just like the three halls that will eventually receive the electron beam, this system operates at 499 MHz with three independently variable slits to define a phase acceptance from 0 to 110 ps for each beam. This part of the apparatus is important because it assures that any beam outside this window would not go correctly through the bunching and acceleration process, and therefore is stopped at the choppers. After the chopper is a device called the buncher which starts the main bunching of the beams. The capture section follows this which simply provides acceleration of the beams to 500 keV in energy. The phase and amplitude of buncher and capture cavities are crucial to the beam bunch length and energy spread. Following the buncher and capture is the bunch length cavity which is a diagnostic system used to tune the beam bunch length by measuring the beam timing. Next are a series of superconducting radio frequency (SRF) cavities which ultimately accelerate the electrons to a final energy or 23 to 68 MeV. There are also three Faraday cups in the injector to measure the beam current at different stages; as well as some magnetic elements which provide transverse focusing and steering of the beam.

Figure 2.4: An illustration of the injector at CEBAF, showing components for photo-producing, bunching and accelerating the beam electrons up to the point where they are ready to be injected into the linear section of the accelerator. [34]

2.2.2 RF Cavities

After the electrons leave the injector, they receive a boost in energy due to several RF cavities that are located inside the linear section of the accelerator. The RF cavities are made with superconducting niobium material and are maintained at 2K using liquid Helium. The cavities have a cycloid geometry in the direction that the electrons travel, and are azimuthally symmetric. The specific design of these cavities are depicted below in Figure[2.5].

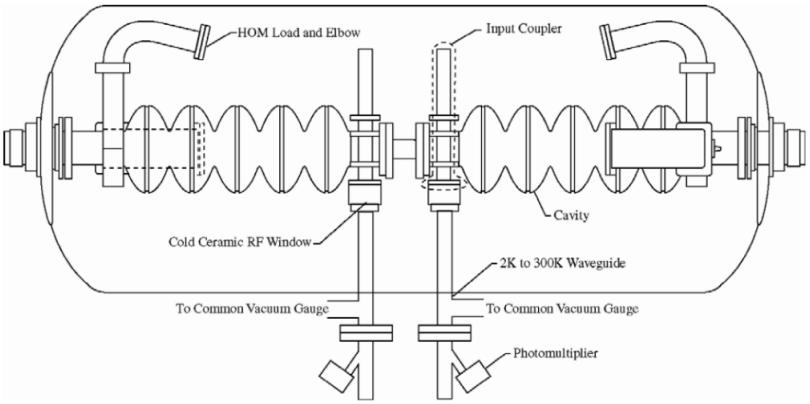

Figure 2.5: An example of th RF cavity design at CEBAF. The electrons would enter the cavity from the left hand side nozzle that is sticking out of the main cavity. Upon entering the cavity, the electrons will have their linear momentum increased inside the cycloid section of the RF cavity. After an increase in linear momentum, the electrons will exit the main cavity to the right. [8]

The electrons will have their linear momentum increased inside the cavities due to a standing radio frequency (RF) electromagnetic wave. The standing waves are kept in phase with the electron beam bunches that are sent from the injector. The acceleration of the electrons is possible due to the changing electric field inside the RF cavities. Once the electrons are inside one of the cavities, the electron is accelerated forward due to an electric field. This field is created by a negative charge collection behind the electron beam bunch, and a positive electric charge ahead of the electron beam bunch. Since the negative charge will repel the electrons and the positive charge will attract the electrons, there is an overall force applied to the beam bunch, causing its linear momentum to increase. An example of this is illustrated in Figure[2.6] below.

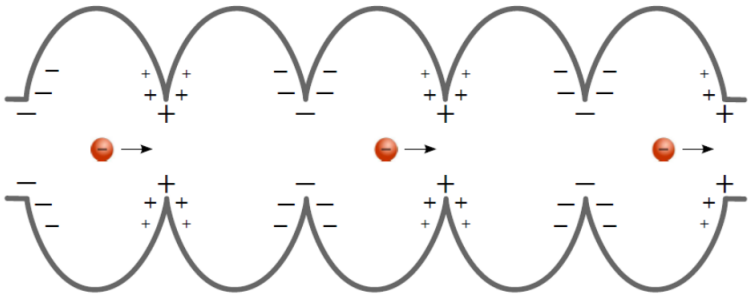

Figure 2.6: An example of how electrons are accelerated inside the CEBAF at Jefferson Lab. The electron beam bunches enter the RF cavities from the right and are immediately repelled away from the negative charge collection on the cavity, while simultaneously are attracted to the positive charge collection farther down stream. As the electrons travel from one cell to the next, the charges will alternate, causing the electron to always maintain a positive acceleration from left to right. [8]

2.2.3 Linac

After the electron beam bunches are accelerated by the RF cavities, they must then turn around by 180° to be accelerated by the other linear section of the accelerator and to ultimately complete one full pass. The steering of the electrons is accomplished by several magnets which are precisely positioned throughout the east and west arcs of the accelerator. The first magnet is responsible for separating the beam into five different mono-energetic beam bunches. Since the linear accelerators will boost the energy of the electrons discretely, the first magnet can be tuned to bend the lower energy electrons more abruptly, while barely affecting the motion of more energetic electrons. This means that the more energetic electrons will bend upward, towards the ceiling of the beam tunnel, while the more energetic electrons will stay relatively level with respect to the beam tunnel floor (Figure[2.7]). In order to turn the beam, a series of magnets are placed along the beam pipes for the different energy levels. After the electron beam has done five passes, it will enter its last turn until it enters Hall D where the GlueX experiment will convert it into a photon beam.

2.3 Hall D

After an electron beam bunch has made 5.5 passes around the JLab accelerator ring and reaches an energy of 12 GeV, it will be passed towards Hall D. This section will follow the electron beam towards the diamond radiator where it will convert some of its momentum to Bremsstrahlung radiation. This radiation will then continue down the beam pipe and into the GlueX spectrometer

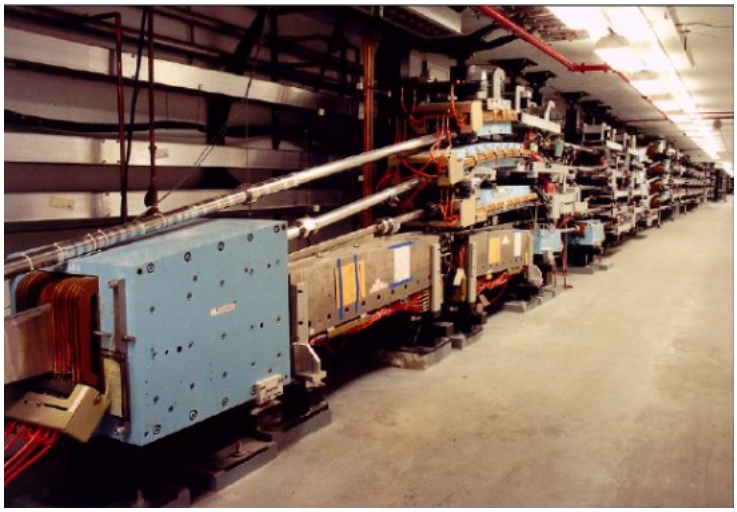

Figure 2.7: A picture inside the acclerator tunnel at Thomas Jefferson National Accelerator Facility; specidically the North Linac section of the accelerator which houses the magnets used to turn the electron beam. The blue box located in the lower left portion of the picture is the magnet responsible for splitting the electron beam into the monoenergetic beam bunches which will eventually continue into one of the five beam pipes in the picture. Farther down steam are several magnets used to steer the beam around the accelerator. Image source [8]

where it will interact with a stationary liquid hydrogen target. All of the relevant sub detectors inside the beam pipe, as well as inside the GlueX spectrometer will be described in the subsections below.

2.3.1 Diamond Radiator

There are four different experimental halls at Jefferson Lab; Hall A, Hall B, Hall C, and Hall D. Halls A, B, and C are located at the south-west section of the accelerator oval, whereas Hall D is located unaccompanied at the opposite end of the accelerator oval. When electrons are approaching the direction of Halls A, B, and C, they can either continue straight into those halls or continue around the track towards Hall D. Once inside the Hall D, the beam collides into a diamond radiator. The diamond radiator is a synthetic material with a nearly perfect lattice structure in order to produce highly polarized photons. It is roughly sixty microns thick and has a square cross sectional area, with each size having a length of 5.6 millimeters. The diamond radiator is mounted onto a goniometer which allows the GlueX experiment to change its orientation relative to the incident electron beam (Figure[2.8]). The orientation of the diamond radiator plane with respect

to the electron beam can change two properties of the coherent Bremsstrahlung radiation. The first property is the energy of the coherent peak, which can be changed by adjusting the transverse angle of the normal of the radiator plane with respect to the beam direction. The second property is the polarization direction of the coherent Bremsstrahlung radiation, which can be adjusted by rotating the radiator in the azimuthal direction with respect to the normal of the radiator plane. Since it is desirable to keep the the energy of the coherent peak a constant throughout an experimental run period, the only property to the beam that will consistently change it the polarization direction.

It should be noted that there is an additional radiator used to collect data at GlueX which does not produce coherent Bremsstrahlung radiation. This radiator is an amorphous radiator and is used intermittently between runs with different diamond radiator orientations. [7]

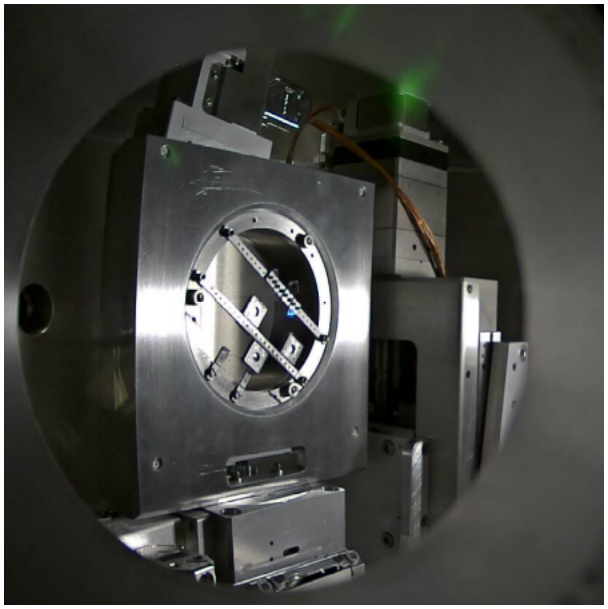

Figure 2.8: A photograph taken from a monitoring camera located inside the beam tunnel. The photograph shows the goniometer which is the disk shaped metal mount in the middle of the square object. Located inside this disk is the diamond radiator which can be seen due to a fain blue light being emitted from its surface. [6]

2.3.2 Photon Beam

Once the linearly polarized photon beam is created by the diamond radiator, it continues straight towards the GlueX detector. Before reaching Hall D, the beam travels through a series collimators which only allow photons traveling with a particular direction to pass. This reduces the amount of

noise from the Bremsstrahlung radiation and ensures that the beam is traveling towards the proton target. In addition, the scattered electrons that are left over from the interaction with the diamond radiator are bent by a magnetic field and are ejected towards a tagger which measures their energy. Knowing the initial energy of the incident electron beam, and then measuring the recoiled energy of the electrons allows us to get an idea of the energy of the photons that are about to enter Hall D. In addition to the energy, the photon tagger can also provide timing information for the photons that arrive into the hall. As previously mentioned, there are two radiators that are used for GlueX; a diamond radiator and an amorphous radiator. The biggest difference between these two radiators is the presence of an organized lattice structure. Since the amorphous radiator has a homogeneous distribution, the photon polarization will be uniform in all directions, while a lattice distribution will only allow photon polarization in one direction. The difference in atomic structure between the two radiators will result in a coherent peak which will be visible in a beam energy distribution. Additionally, the photons contained within the coherent peak will be highly polarized. In the case of GlueX, our radiator is designed to produce a fourty percent linear photon polarization at the edge of the coherent peak. These effects are most easily understood by referencing Figure[2.9], which is from the first GlueX physics publication [28].

2.3.3 Triplet Polarimeter (TPOL)

The triplet polarimeter (Figure [2.10]) is responsible for measuring the degree of polarization from the coherent Bremsstrahlung radiation created by the diamond radiator. The triplet polarimeter measures the degree of photon polarization using the triplet photoproduction process. When an incident photon interacts with the electromagnetic field of an bound state electron, the incident photon can spontaneously convert into an electron-positron pair, in addition to kicking the bound state electron out of its orbital. Since the recoil electron will have a very large polar scattering angle with respect to the incident beam direction, the triplet polarimeter is responsible for measuring the azimuthal distribution of the recoil electron. Conversely, the electron-positron pair will carry most of the longitudinal momentum from the incident photon, therefore causing them to travel farther down stream and eventually detected by the pair spectrometer. The azimuthal angular distribution of the recoil electron will provide information on the polarization of the incident photon. The determination of photon polarization in the triplet polarimeter is similar to the study of beam asymmetries, such that the triplet cross section is proportional to the total cross section multiplied

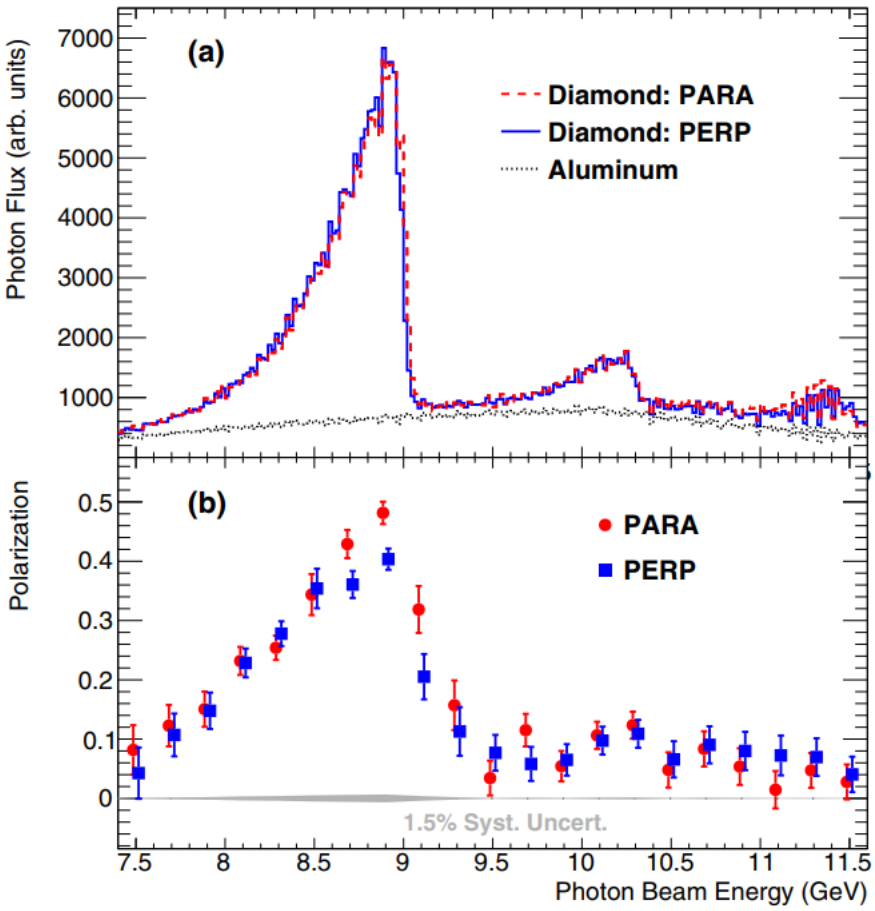

Figure 2.9: (a) Photon beam intensity versus energy as measured by the pair spectrometer (not corrected for instrumental acceptance). (b) Photon beam polarization as a function of beam energy, as measured by the triplet polarimeter, with data points offset horizontally by 0.015 GeV for clarity. [28]

by a factor which involves the cosine of the recoil electron. Measuring the coefficient from a fit of the recoil electron angle will allow GlueX to determine the degree of polarization of photons as a function of beam energy. [32]

2.3.4 Pair Spectrometer (PS)

After a photon interacts with the thin converter of the triplet polarimeter, an electron-positron pair are immediately produced with high longitudinal momentum, causing them to travel downstream. A dipole magnet of 1.8 Tesla is located after the triplet polarimeter in order to separate the

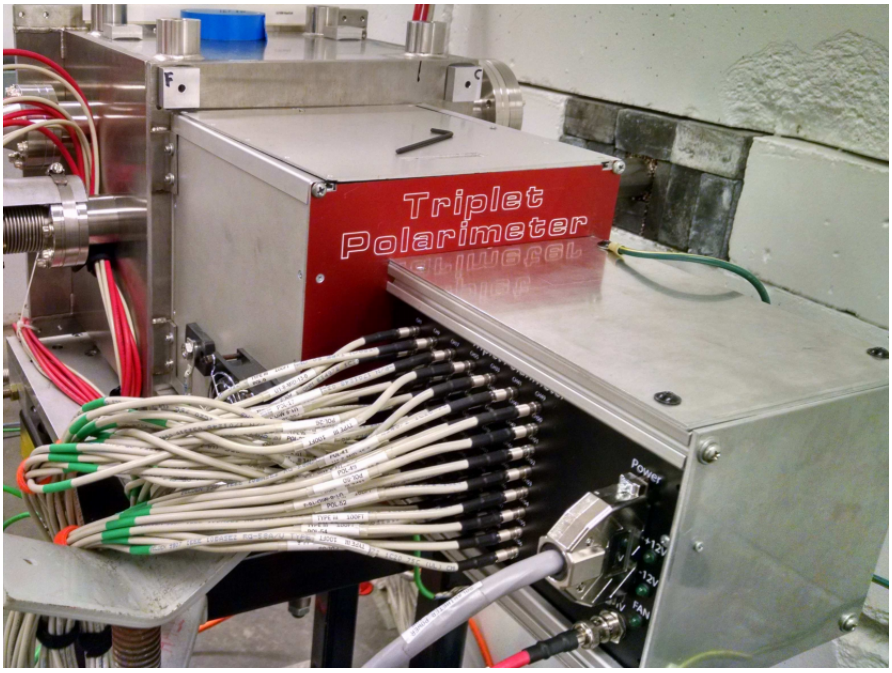

Figure 2.10: A picture of the triplet polarimeter inside the Hall D beamline. The photon beam will enter the triplet polarimeter from the upper left part of the picture and travel to the right. After interaction with the triplet polarimeter, an electron-positron pair will travel beyond the wall on the right portion of the photograph, where pair spectrometer is located; as well as the GlueX spectrometer. [32]

photoproduced electron and positron and to not affect neutral particles such as the beam photons. Upon separation, the electron and positron will eventually be detected by scintillators on the pair spectrometer (Figure[2.11]). The scintillation array on the pair spectrometer consists of sixteen course counters, as well as an additional layer containing a high-granularity hodoscope. Since the electrons and positrons will travel in opposite directions due to the dipole magnetic field, there are two arms on the pair spectrometer, each of which can measure an electron/positron energy between 3 GeV and 6.25 GeV. This electron/positron energy range corresponds to a photon energy between 6 GeV to 12 GeV. The addition of the pair spectrometer allows GlueX to measure two important features about the incident photon beam, the energy and the flux (Figure [2.9a]). As previously mentioned, the pair spectrometer has the ability to reconstruct the energy of the pair produced electron and positron, thus allowing us to measure the energy of the incident photon. Additionally, knowing the radiation length of the diamond or amorphous radiator in conjunction with the amount of hits per beam bunch that the pair spectrometer sees, allows us to estimate the

photon flux entering the GlueX spectrometer. Accurately measuring the beam energy is obviously important for determining the amount of energy allowed in a final state, and measuring the beam flux is important for determining cross sections of final states as well. [20] [7]

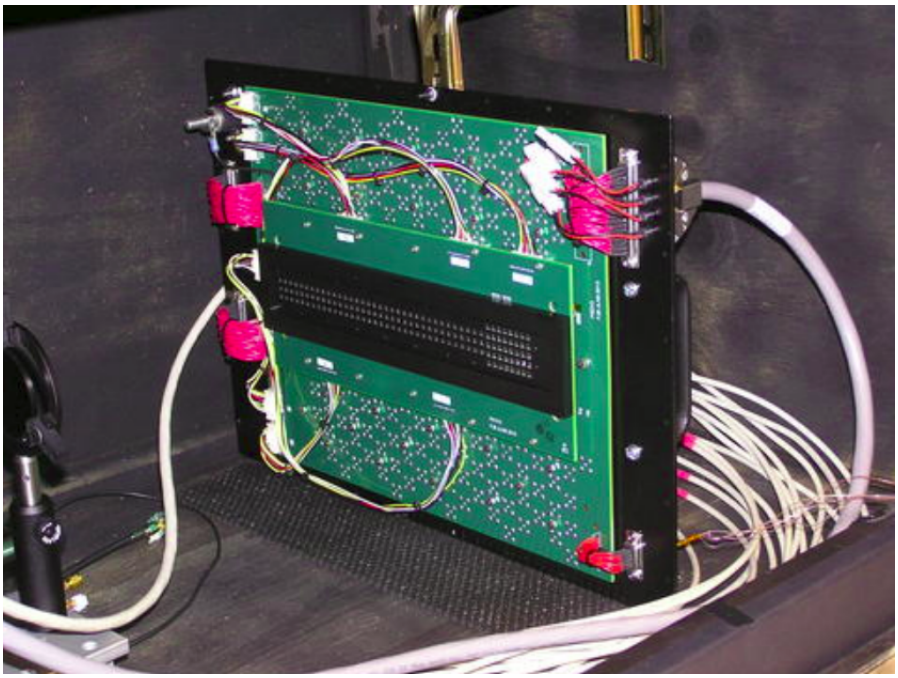

Figure 2.11: A picture of the pair spectrometer. [4]

2.3.5 Target

As the photon beam travels down the beam pipe and enters the GlueX detector, it will eventually interact with the target. The target at GlueX is a proton, so therefore the target chamber is filled with liquid Hydrogen (LH_2) which is stored at roughly 18 degrees Kelvin and at a pressure of 16 psiA. The entrance and exit of the target chamber are made from the polymide film material Kapton [11], and are 75 μm thick. The liquid hydrogen is insulated from the start counter by five layers of aluminized mylar and cerex material. The length of the target is aligned in the direction of the photon beam in order to increase the likelihood of observing an interaction with one of the protons at rest. [16] [7]

2.3.6 Start Counter (ST)

The start counter is the first detector located outside of the target chamber. The purpose of the start counter is to record the time of the photon-proton interaction which took place inside the target chamber, and to ultimately identify which beam bucket caused an event. Due to this, the start counter is designed to handle photon intensities up to $10^8 \frac{\gamma}{s}$, and must also have the ability to differentiate between beam buckets which can be separated by as little as 2 nanoseconds, or 500 MHz. The detector consists of thirty scintillators which are uniformly distributed around the target chamber in the azimuthal direction, which can be seen in the schematic given in Figure [2.12]. The scintillators contain silicon photomultipliers in order to record when the detector fires and to ultimately create a signal. Another important aspect of the start counter is the fact that its components and are not affected by the superconducting solenoid magnet which produces a strong magnetic field where the apparatus is located. The start counter has a timing resolution which ranges from 450 to 700 picoseconds and can correctly identify beam buckets up to a 94 percent accuracy. It also provides a ninety percent solid angle coverage around the target chamber, with the exception of highly back scattered angles with respect to the beam direction, and a hole in the forward direction due to noise from the beam. [24] [7]

2.3.7 Superconducting Solenoid/Magnet

The superconducting solenoid/magnet is the outer most part of the barrel portion of the GlueX detector. It was originally built and used by the Stanford Linear Accelerator (SLAC) in the 1970's for the LASS detector; and was even used for the E-135 experiment in the early 80's. In 1985, the solenoid was moved to Los Alamos National Laboratory (LANL) in order to be used for the MEGA experiment. Eventually, the superconducting magnet was moved to Hall D of Jefferson Lab during April of 2000, and has been housed there ever since. The superconducting solenoid has a diameter of 1.85 meters, and is 4.8 meters in length and can be seen in Figure[2.13]. This barrel shaped geometry contains four separate superconducting toroidal coils connected in series, as well as four cryostats, which all contribute to produce a magnetic field. When operating at the maximum GlueX current, the magnet can produce a magnetic field inside the spectrometer of roughly two Tesla in the direction of the beam direction. The operating current is 1360 Amperes, which produces has an inductance of 26.3 Henry and a stored energy of 24 mega joules inside the

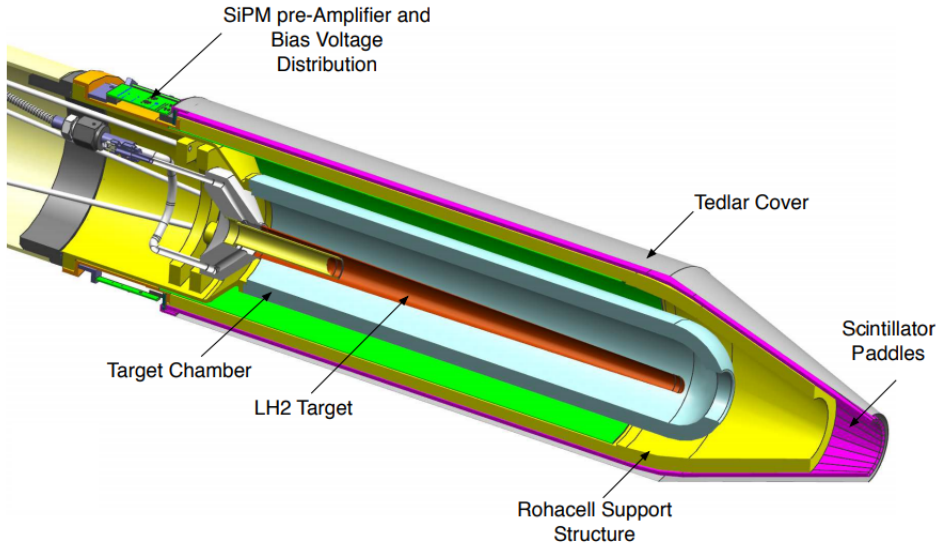

Figure 2.12: A schematic of the start counter located at the center of the GlueX spectrometer. The photon beam enters the detector from the upper left hand corner of the schematic and will exit the lower left hand corner of the schematic, out of the nozzle of the device. The start counter encapsulates the target chamber and makes its measurements using the scintillator paddles labled on the diagram. [24]

coil. In order for the coil of the solenoid to be superconducting, there is a common liquid Helium reservoir located on top of the barrel in order to cool the system. Part of the cooling apparatus can be seen in Figure[2.13]. The purpose of the superconducting solenoid/magnet is to produce a magnetic field responsible for bending charged particles inside the detector. The existence of this magnetic field allows us to determine both the charge of a particle as well as its momentum. The momentum of a charged particle is proportional to the radius of curvature around a magnetic field line. Having the ability to measure both the charge and momentum of charged particles is crucial for any physics analysis at GlueX. [10] [7]

2.3.8 Central Drift Chamber (CDC)

There are two subdetectors inside the GlueX spectrometer which are responsible for tracking charged particles; one of them is the forward drift chamber, and the other is the central drift chamber. The central drift chamber has a cylindrical/barrel geometry, much like the superconducting solenoid, with the exception that the central drift chamber surrounds the target and start counter, and is inside of the barrel calorimeter. The large cylindrical chamber is 1.5 m long and has an

Figure 2.13: A picure taken of the solenoid located inside Hall D. [10]

inner radius of 10 cm and an outer radius of 54 cm. Located within the central drift chamber are twenty four layers of 1.6 cm diameter straw tubes, containing a total of 3522 anode wires made of gold-plated tungsten at their centroid (Figure[2.14]). Between the anode wires and the walls of the straw tubes is a mixture of carbon dioxide and Argonne gas at atmospheric pressure. The purpose of this gas is to become ionized when a charged particle has passed through it. This ionized gas is then attracted to the gold-plated tungsten wires do to the fact that they have a voltage. The charge deposited onto the wire will induce a current inside the anode which and then be read out by electronics in order to record the geometric path that a charged particle has taken within the central drift chamber. This chamber is optimized for charged tracks with highly transverse momentum and therefore covers a polar angle range between 6 and 165 degrees with respect to the beam direction. In addition, the barrel shaped geometry of the central drift chamber provides a full angular coverage in the azimuthal direction. The detector has been optimized for a position resolution perpendicular to the wires of 150 micrometers, and can also provide information on the loss of energy per unit distance. This measurement allows the GlueX spectrometer to separate positively charged pions from protons with momentum as high as 450 MeV/c. In addition to energy loss, the

central drift chamber is also responsible for measuring momentum of charged particles by utilizing the path that a charged particle has taken inside the magnetic field of the spectrometer. Knowing the momentum of charged particles is another crucial measurement for performing physics analyses at GlueX. [7] [3]

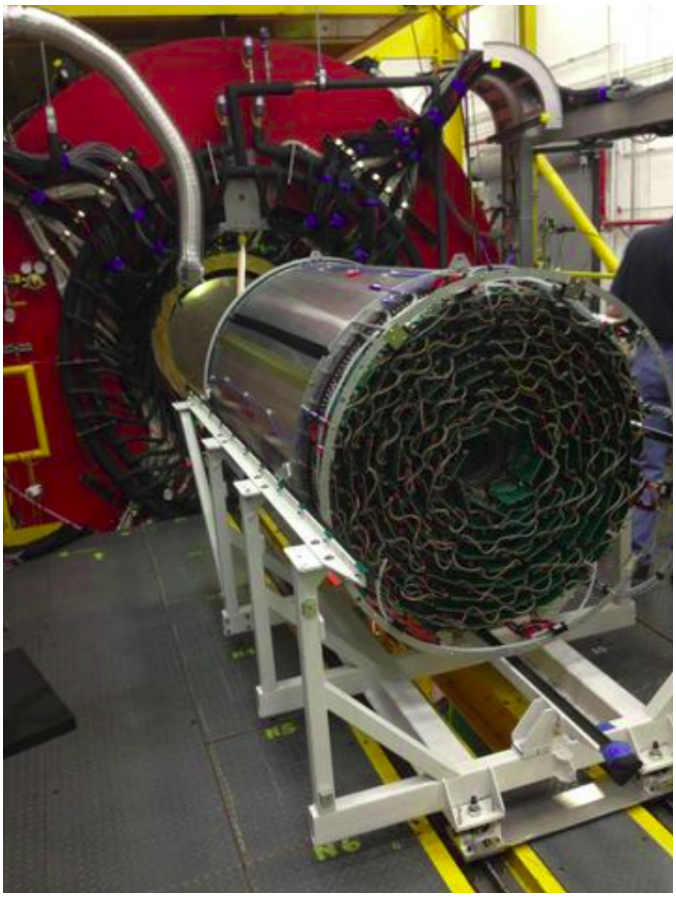

Figure 2.14: A picure taken of the central drift chamber before being installed into the GlueX spectrometer inside Hall D. [4]

2.3.9 Forward Drift Chamber (FDC)

The forward drift chambers (FDC) are located downstream of the central drift chamber and are encapsulated by the superconducting solenoid/magnet and barrel calorimeter. The purpose of the detector is to track charged particles originating from the target chamber with shallow angles relative to the beam direction. Since it is in the downstream direction, the forward drift chamber is designed to provide a large number of measurements in a short amount of time due

to high momentum and the high multiplicity of tracks. Much like the central drift chamber, it must also have good spatial resolution of charged particle paths in order to accurately reconstruct their momentum. To perform these tasks, the forward drift chamber uses two planes comprised of cathode strips which face a wire plane. The cathode strips are analogous to the argon-carbon dioxide gas inside the straws of the central drift chamber; when struck by a particle, a charge is induced onto the strips. This excess of charge is measured by the detector and with timing information, can properly reconstruct the path of a charged particle. The FDC detector includes four separate but identical 62 disk-shaped packages. Each of the disk shaped packages contains six independent planar drift chambers with separate gas volumes. Contained within these gas volumes are an anode wire frame with two cathode strip planes. There are also aluminized mylar planes which act as ground between the electrically charged strips. The four sets of electrical planes with six gas volumes can easily bee seen in Figure[2.15]. [7]

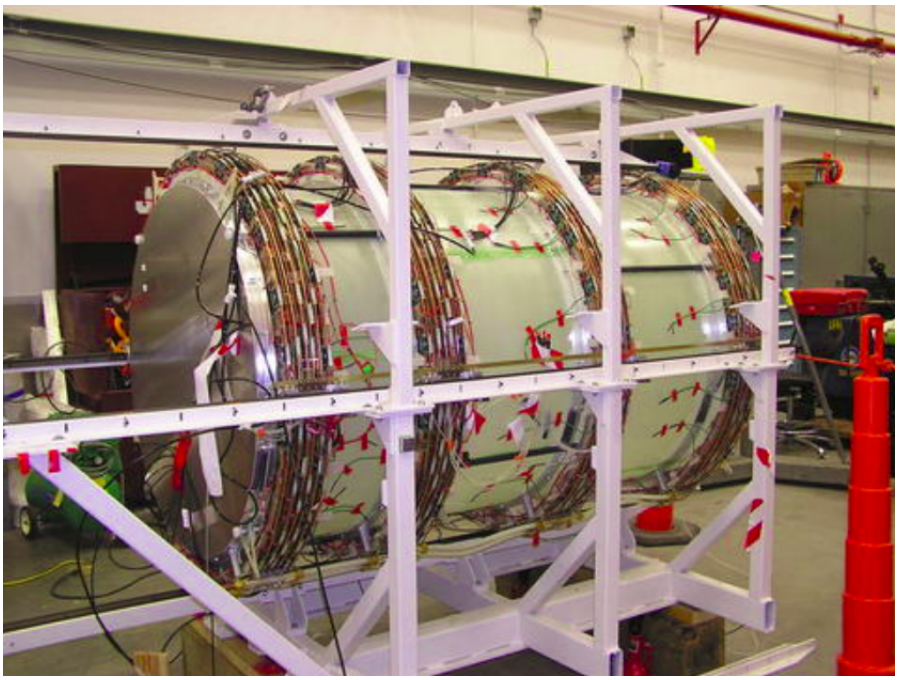

Figure 2.15: A picure taken of the forward drift chamber being surveyed on the floor of Hall D before installation. [4]

2.3.10 Barrel Calorimeter (BCAL)

At this point, a lot has been said about the detection of charged particles, but not a lot has been said about the detection of neutral particles, specifically, photons. One of the devices that is designed to detect photons is the barrel calorimeter. Originally constructed at the University of Regina, the BCAL is a lead scintillating fiber matrix, located immediately inside the super conducting solenoid. This sub detector has an outer radius of 90 cm, an inner radius of 65 cm, and is 390 cm in length, as seen in Figure[2.16]. The primary goal of the barrel calorimeter and the forward calorimeter is to measure photons which originated from the decays of π^0 and η; both of which product two photons as their primary decay branch. When a particle enters the BCAL, it excites several electrons inside the scintillation material, which then radiate energy in the form of photons. The photons travel down the scintillation wires until they reach the endpoints of the barrel where they are then collected by light guides which then leads to photo multiplier tubes (PMT). The PMT's collect the light signals and convert them into amplified electrical pulses. The barrel calorimeter performs this duty by accurately reconstructing the positions and energies of photons within the GlueX spectrometer. The BCAL can measure individual photon energies as low as 60 MeV and as high as 2.5 GeV, and additionally can provide timing information for photons and charged tracks originating from the target chamber. The timing, energy, and position resolution for the barrel calorimeter is somewhat tricky to define, as many of these parameters are a function of the incident photons energy and angle with respect to the lead scintillating blocks. As an example, the energy resolution of the BCAL depends on the number of photo-electrons detected by the photo sensors at the end of the scintillators. The number of photo electrons produced within a lead block is directly proportional to the energy deposited by the incident photon. The photon position is determined by the readout segmentation in the beam line direction as well as the azimuthal direction. [7] [35] [5]

2.3.11 Forward Calorimeter (FCAL)

Much like the barrel calorimeter, the forward calorimeter is designed to detect photons which were radiated by either π^0 or η mesons; only this detector is placed in the forward direction rather than a direction more transverse to the beam direction. The forward calorimeter is comprised of an array of lead glass scintillators which collectively form a circular pattern to cover the end of

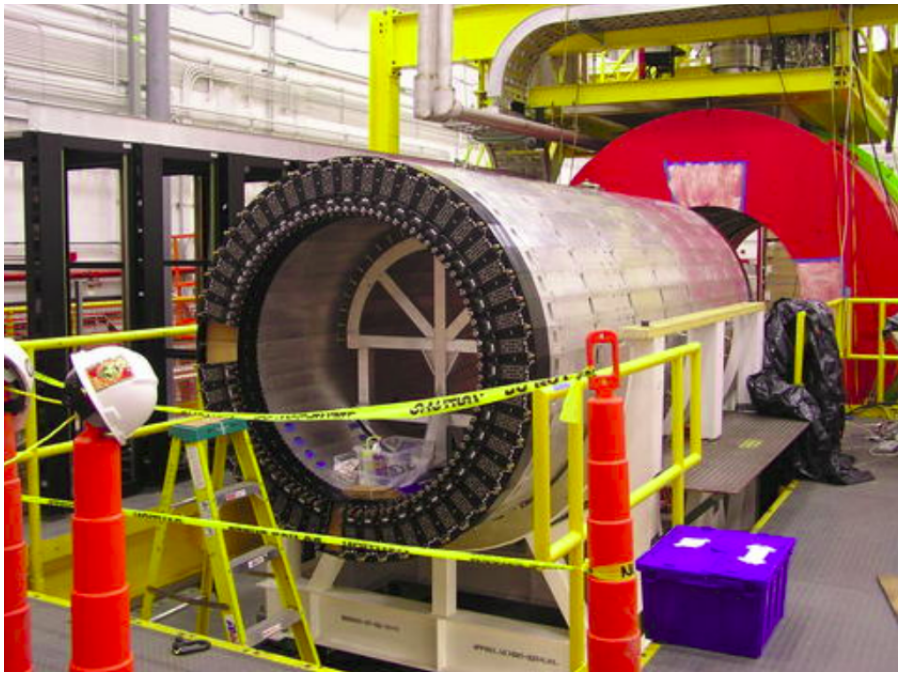

Figure 2.16: A picture of the barrel calorimeter before assembly into the superconducting solenoid. [4]

the barrel segment of the GlueX spectrometer, as seen in Figure[2.17]. The lead glass scintillators detect high energy photons because of their tendency to spontaneously pair produce into an electron-positron pair upon entering the lead glass medium. The resulting electron-positron pairs emit bremsstrahlung radiation, which can then spontaneously pair produce into another electron-positron pair. This process will continue until all of the energy from the original photon has been completely absorbed by the lead glass in a process which is known as showering. When the electron-positron pair travel through the lead glass material at a high enough velocity, they can produce Cherenkov radiation which is collected and measured by photomultiplier tubes attached to the end of the lead blocks. The amound of Cherenkov radiation that is detected by the absorbing lead block is directly proportional to the amount of energy deposited into it. Therefore, knowing the position, energy, and timing of the incident photon allows us to perform particle identification on photons traveling in the forward direction. The forward calorimeter has a circular lead glass array with a diameter of 2.4 meters and has 2800 lead glass blocks. The front face of the forward calorimeter is 560 cm down stream from the center of the target chamber. Each lead glass block has a rectangular geometry, with a 4x4 cm square base and a height of 45 cm. In addition, a 3x3 square array of lead

block located near the beam hole were removed from the detector due to the high rates inherent within that region of the detector. [7] [2]

Figure 2.17: A picture of the forward calorimeter with no cover in front of it. One can clearly see the lead scintillators used to reconstruct photons in the forward direction. [4]

2.3.12 Time of Flight Detector (TOF)

Unlike the aforementioned detectors, the time of flight (TOF) is square in shape and is 252 x 252 centimeters in size. The sub detector has two layers of scintillator paddles, one layer that is parallel to the floor of Hall D, and a second layer that is perpendicular to the floor of Hall D. Each layer contains 38 'standard' paddles, 4 'half width' paddles, and 4 'half length' paddles. The dimensions of the standard paddles is 2.54 x 6 x 252 cm, while the half width paddles are 2.54 x 3 x 252, and the half length paddles are 2.54 x 6 x 120. The purpose of the half width paddles is to compensate for the higher rates that take place closer to the beam hole, and the purpose of the half length paddles is to allow the beam to pass through the beam hole. All of these different paddles can be seen by closely inspecting Figure[2.18].

The time of flight is located downstream of the cylindrical portion of the GlueX detector and is before the forward calorimeter. The time of flight is comprised of transparent scintillating bars that

are wrapped in highly reflective material so that no light can escape. The scintillation material in the TOF is similar to the scintillation material in the BCAL. When a particle hits the time of flight, the electrons inside the scintillation material become excited and radiate photons which travel down the material and are eventually collected by a photomultiplier tube. The purpose of the time of flight is to deduce how long it took a particle to travel from the interaction vertex inside the target chamber, all the way to the wall of the time of flight. Since the distance travelled by a charged particle is known from the reconstructed drift chamber paths, we can divide this by the flight time in order to calculate a velocity. In addition to the path of a charged particle, the momentum of it can also be measured due to the fact that it is proportional to its radius of curvature with respect to the magnetic field within the spectrometer. Measuring the momentum of a charged particle and calculating its velocity within the chamber allows us to approximate the mass of the particle which ultimately leads to a particle identification. [7]

Figure 2.18: A picture of the time of flight after sucessful assembly inside Hall D. [4]

CHAPTER 3

MONTE CARLO

3.0.1 Monte Carlo Features of $\gamma p \to p\phi\eta$

In order to better understand the acceptance of the $\gamma p \to p\phi\eta$ topology in the GlueX spectrometer, a generated Monte Carlo sample was analyzed. More specifically, the exact sample that was produced was $\gamma p \to pX; X \to \phi\eta; \phi \to K^+K^-; \eta \to \gamma\gamma$. This Monte Carlo sample consisted of 170 k generated events for each of the run numbers 030408, 030620, 030802, and 031029. There run numbers were chosen because the first two have beam polarizations in the PARA/PERP directions at low intensity, and the second two have PARA/PERP orientations at high intensity. The total number of generated $\phi\eta$ events is therefore 680 k. The events were generated using a coherent bremsstrahlung beam energy spectrum and a t-slope of 4 $(GeV/c^2)^2$. To be more clear, the thrown beam particles were not polarized in this sample; only the beam energy spectrum matched that of a polarized beam spectrum (Figure [3.1]). All final state particle kinematics were generated using the ROOT object TGenPhaseSpace. The generated final state phase space was flat and therefore did not include any spin information from parent or daughter states. The $\gamma, K^+, K^-, \phi, \eta$, and p particles were generated using the invariant mass values provided in the PDG. The photo-produced X mass was randomly distributed between the lower kinematic limit $m_\phi + m_\eta$ and the upper kinematic limit which is a function of the thrown beam energy.

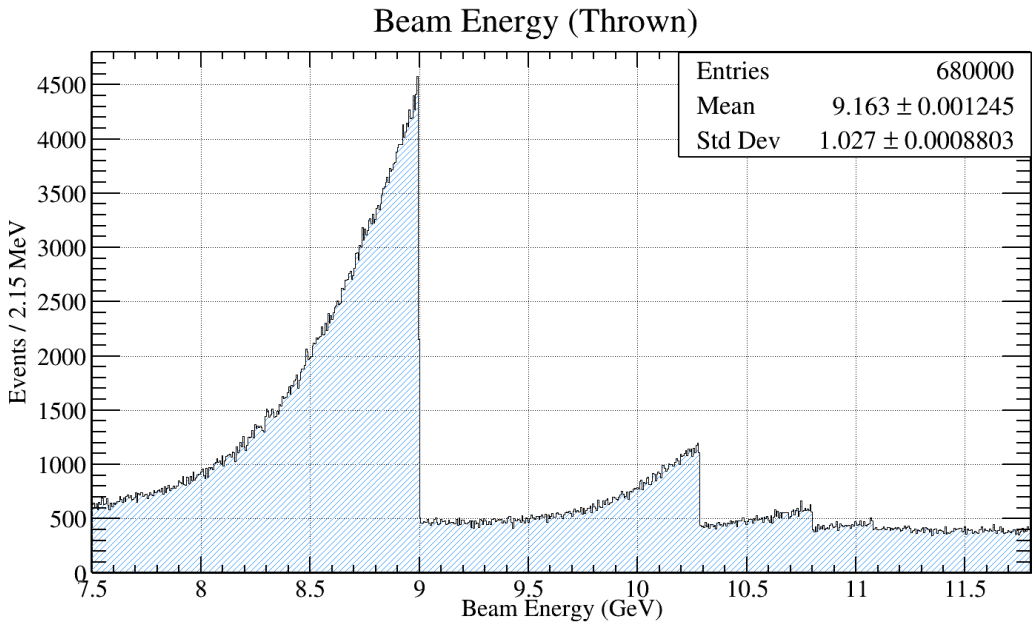

Figure 3.1: A histogram which includes the thrown beam statistics from the generated Monte Carlo example. In the figure one can easily see the coherent peak which maximizes at 9 GeV. Additionally, one can also see other secondary peaks at higher energy.

An example of what the generated beam energy distribution looks like for this Monte Carlo sample is given in Figure [3.1]. It should be noted that this particular Monte Carlo sample only generated beam energies between the values of $7.5 - 11.8$ GeV. The reason for the lower energy boundary of the beam energy spectrum is to both cut out potential areas of background due to low energy beam photons and to allow a larger sampling of polarized photons when a beam asymmetry study is performed with actual data. The high energy cut off of 11.8 GeV is simply there to match the high energy cut off of the Spring 2017 run.

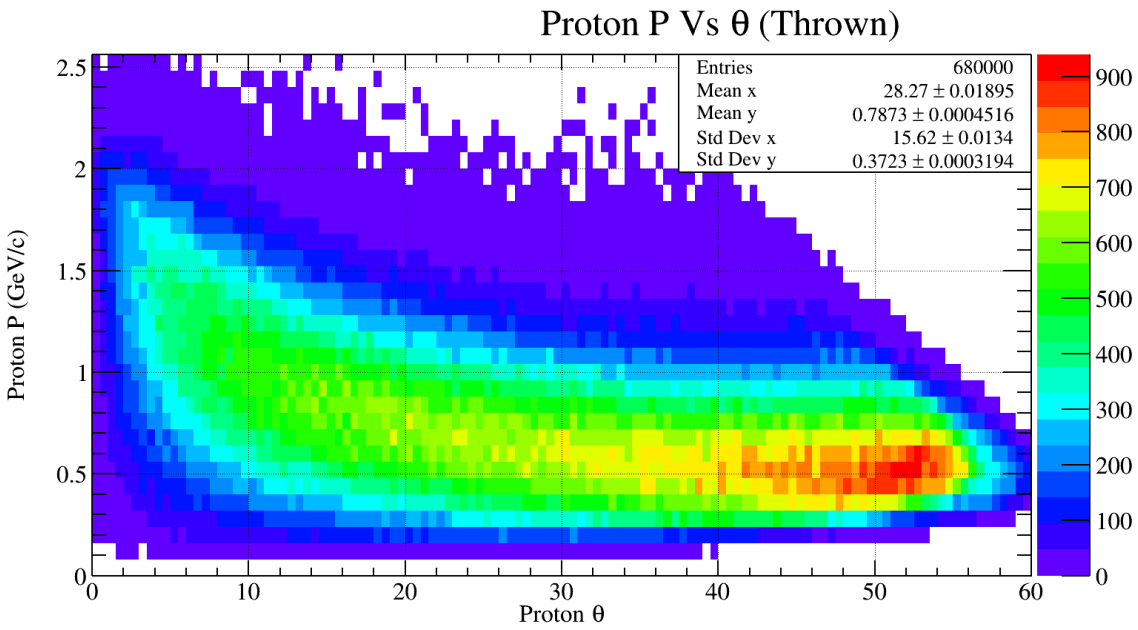

Figure 3.2: A two dimensional histogram which includes the thrown kinematic information of the recoil proton. In the histogram, the horizontal axis represents the generated θ angle in the lab frame, and the vertical axis represents the generated momentum magnitude in the lab frame. One interesting feature of this Monte Carlo data is that the protons kinematics appear to be constrained between $[0.2 - 2.0] GeV/c$ in momentum, and $[0.0 - 60.0]$ in angle.

Momentum versus theta distributions are also provided in Figures [3.2], [3.3], [3.4], and [3.5]. These figures are not accepted Monte Carlo, they are only the generates four vectors of the final state particles before running hdgeant, mcsmear, or `hd_root`. Still, the figures provide some insight into the expected kinematic distributions of the final state particles. For example, Figure [3.2] displays the momentum versus theta distribution for the recoil proton. This figure shows that we should expect the proton to have a very low momentum and high recoil angle relative to the beam direction for this final state.

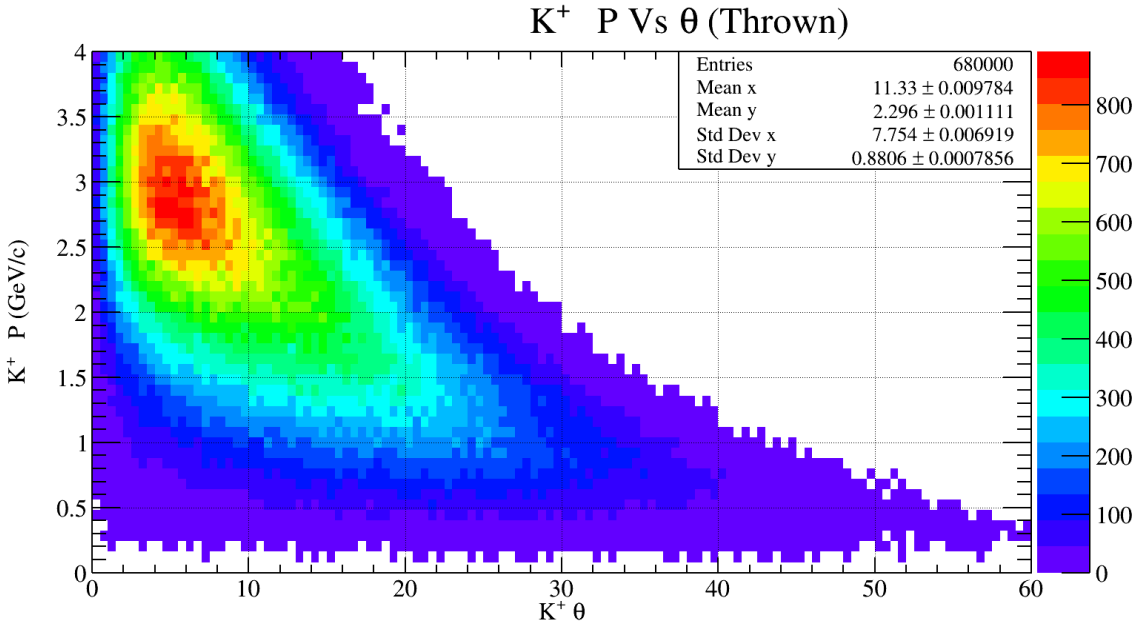

Figure 3.3: A two dimensional histogram which includes the thrown kinematic information of the generated K^+. In the histogram, the horizontal axis represents the generated θ angle in the lab frame, and the vertical axis represents the generated momentum magnitude in the lab frame.

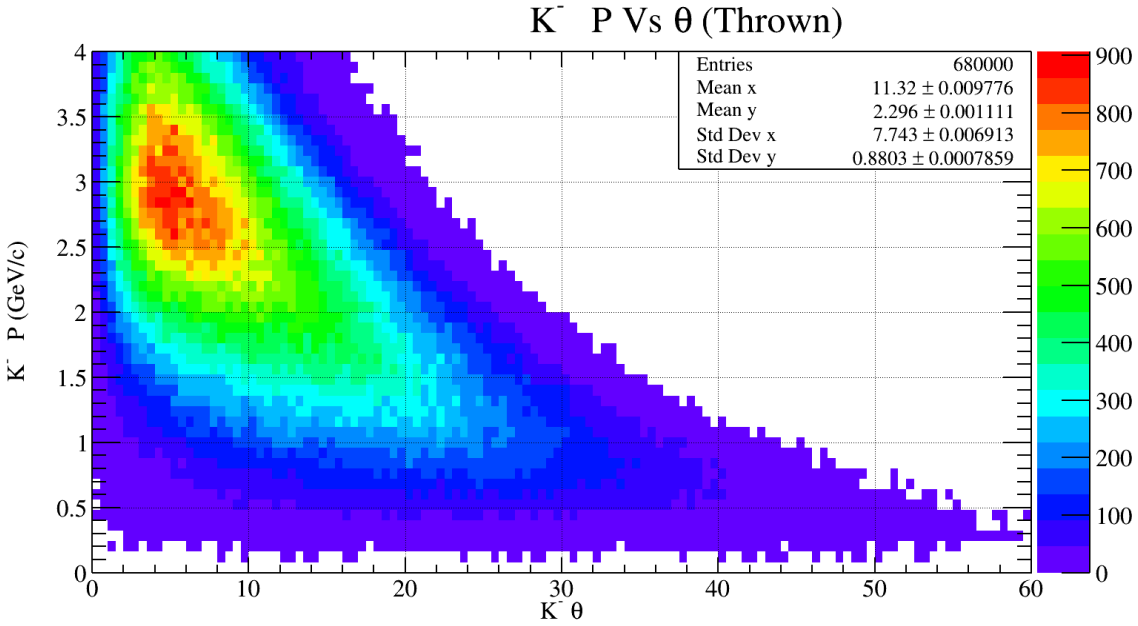

Figure 3.4: A two dimensional histogram which includes the thrown kinematic information of the generated K^-. In the histogram, the horizontal axis represents the generated θ angle in the lab frame, and the vertical axis represents the generated momentum magnitude in the lab frame.

Additionally. Figures [3.3][3.4] show the same plot but for K^+ and K^-, respectively. In these figures, it is clear that Kaons will preferentially travel towards the TOF/FCAL and with a momentum that should include a lot of pion contamination (see Figures [4.18][4.26] for more information on pion contamination at high momentum).

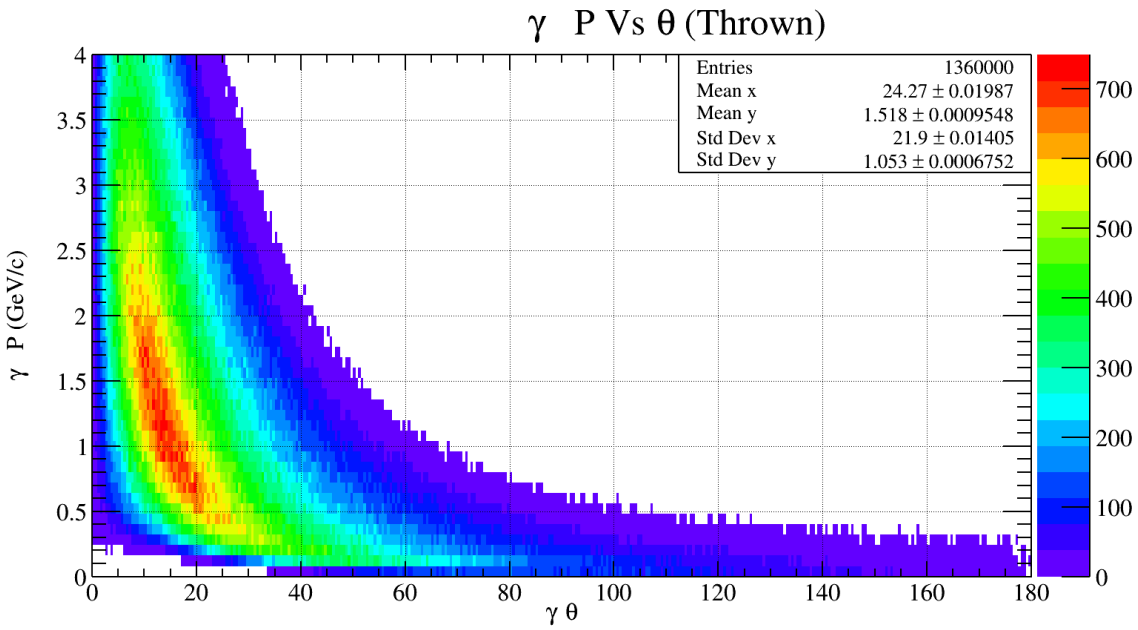

Figure 3.5: A two dimensional histogram which includes the thrown kinematic information of the generated photons. In the histogram, the horizontal axis represents the generated θ angle in the lab frame, and the vertical axis represents the generated momentum magnitude in the lab frame.

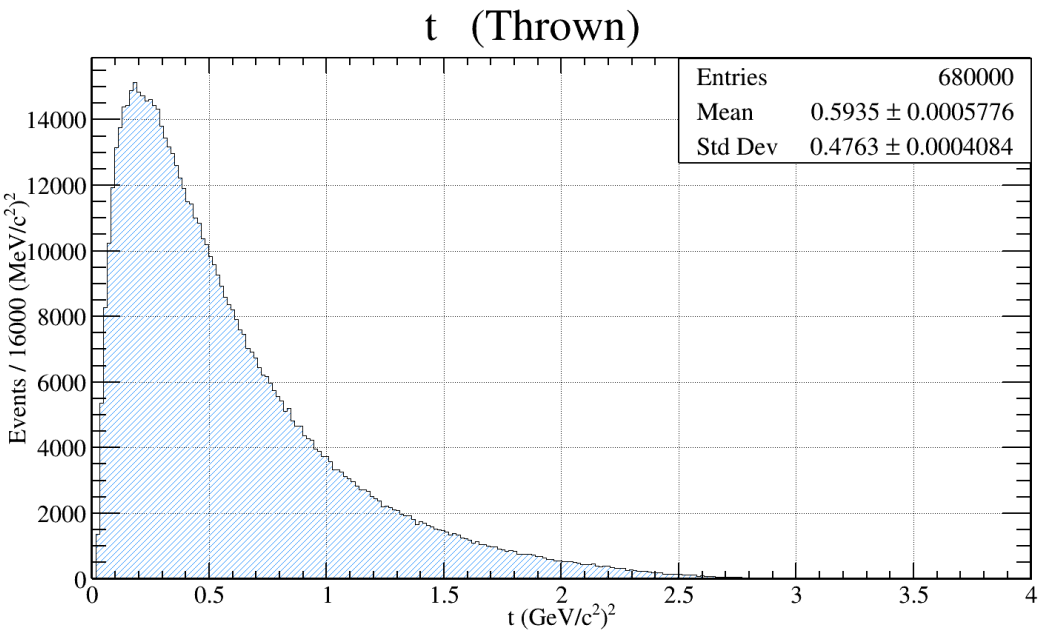

Figure 3.6: A histogram which includes the generated spectrum for the Mandelstam variable, t. The most important feature in this histogram is the fact that the majority of generated events come from low momentum transfer.

Lastly, Figure [3.5] shows that the final state photons will be mostly forward going and therefore we should expect to see the majority of them interacting with the FCAL rather than the BCAL. It comes as no surprise that the Monte Carlo has generated photons and kaons that favor the forward direction, while the recoil proton has low momentum and a highly transverse direction. This is simply a consequence of the fact that a 'low t' interaction was programmed into the Monte Carlo, resulting in Figure [3.6].

The last few figures I wish to discuss in this section involve the study of invariant mass spectra. The first of which is the invariant mass of $\phi\eta$ (Figure [3.7]) which shows a flat distribution between the values of 1.5 to 3 GeV/c^2; then the distribution drops off drastically until 3.3 GeV/c^2; and then less drastically from 3.3 to 4 GeV/c^2. These features may seem incorrect at first glance since the generated Monte Carlo mass is supposed to be flat. However, upon further inspection, it is clear that these features manifest themselves within the Monte Carlo data because of the shape of the beam spectra. The best way to see this behavior is by considering Figure [3.8]. This figure shows the generated Mandelstam variable t on the vertical axis, and the generated $\phi\eta$ mass on the

horizontal axis. Since t is the momentum transfer, it is directly correlated with the beam photon and therefore will exhibit some coherent bremsstrahlung structure. This structure can be seen in Figure [3.8] where there is clear evidence of the beam energy spectra influencing the behavior of the $\phi\eta$ mass. We know from Figure [3.1] that the most dominant statistics will come from the coherent edge at 9 GeV and should drop off drastically beyond that point. This feature of the data is clearly seen in Figure [3.8] and is therefore the reason for the odd behavior seen in Figure [3.7].

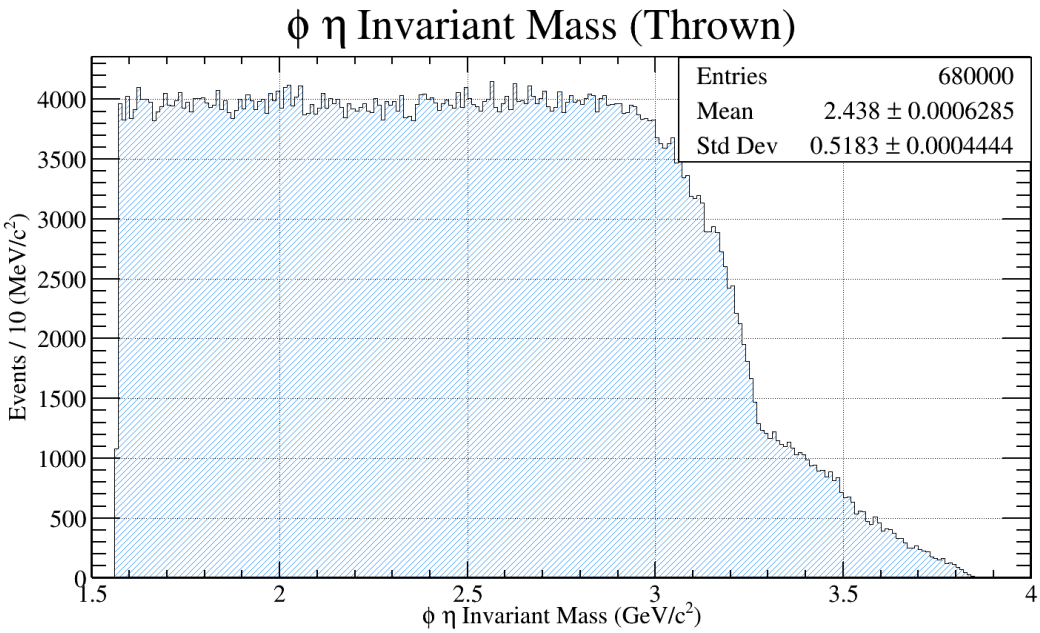

Figure 3.7: A histogram which includes the generated $\phi\eta$ invariant mass. In the figure one can easily see that the invariant mass of the $\phi\eta$ remains flat until it reaches $\sim 3.0 GeV/c^2$. From that point, the invariant mass falls sharply until $\sim 3.3 GeV/c^2$; and then continues to fall at a slower rate. This feature of the invariant mass is directly related to the fact that a coherent bremsstrahlung beam energy spectrum was used. The drastic drop off in statistics in the mass range of $3.0 - 3.3 GeV/c^2$ is caused by the primary coherent peak at $9.0 GeV$. To visualize this more clearly, see Figure [3.8].

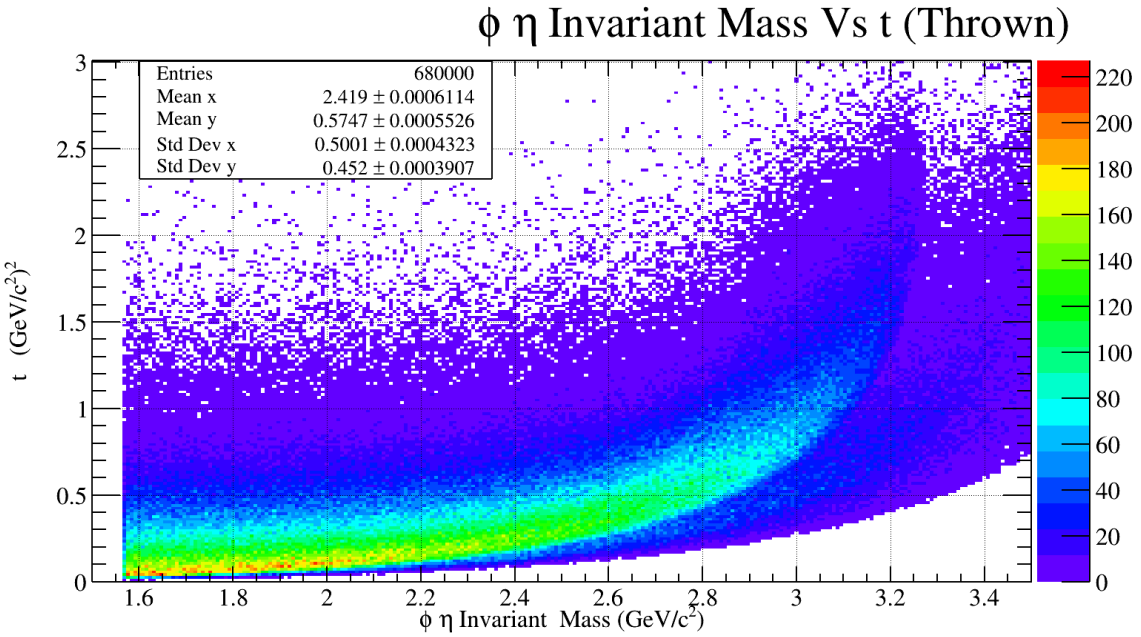

Figure 3.8: A two dimensional histogram which includes the generated $\phi\eta$ invariant mass on the horizontal axis and the Mandelstam t variable on the vertical axis. In the figure one can easily see the effect that the coherent peak has on the shape of the phase space. The effect can be seen in even greater detail in Figure [3.7].

CHAPTER 4

DATA SELECTION

4.1 Identification of $\gamma p \to pK^+K^-\gamma\gamma$ Events at GlueX

In order to study potential states of bound strangeonia, it is essential to properly identify all final and initial state particles. The final state topology that will be studied for this thesis is $\gamma p \to pK^+K^-\gamma_1\gamma_2$, where the K^+K^- pair are daughter states of the ϕ meson, and the $\gamma_1\gamma_2$ pair are daughter states of the η meson. Therefore, the beginning of this analysis section will focus on the particle identification of the proton, kaons, and final state photons, as well as the incident beam and target proton. Once identification of all particles has been well established, this analysis will then provide evidence that the final event sampling enforces exclusivity.

4.1.1 Spring 2017 Run Period

The data presented here is the result of the successful Spring 2017 Low Intensity run period. The Spring 2017 run period spanned from January 23rd to March 13th and accumulated roughly 50 billion physics events. The maximum electron beam energy used was 12 GeV, and the accelerator ran at 250 MHz while in low intensity (beam every 4 ns), and later ran at 500 MHz while in high intensity (beam every 2 ns). Upon entering Hall D, the electron beam was incident upon a radiator. During this run period, both amorphous and diamond radiators were used to produce either incoherent or coherent polarized bremsstrahlung radiation. The diamond radiator was experimentally set up to produce linear photon polarization at four different angles; 0°, 45°, 90°, and 135°. These directions were chosen in order to provide the detector with a uniform sampling of linear polarization in the transverse direction to the incident beam. In order to yield roughly the same amount of statistics for an amorphous radiator run as compared to a diamond radiator run, a beam current of 150 nA was incident upon the amorphous radiator, while a beam current of 100 nA was incident upon the diamond radiator. Farther downstream, a 5mm collimator hole was used for all radiator configurations. Lastly, the collimated photon beam was incident upon a stationary liquid hydrogen target. This resulted in one petabyte of files and $16pb^{-1}$ of integrated luminosity.

4.1.2 Identification of Initial State Particles

Photon Beam. The first step in identifying the initial state beam photon is to select the correct beam bunch. Since the electron beam is delivered from the accelerator every four nanoseconds, the timing of when the beam particles arrive into the hall is well known and we call this the Radio Frequency (RF) time. In addition to the RF time, we also have the beam time. The beam time is defined as the time which the reconstruction converged upon a common vertex time. The common vertex time is found by using the final state charged tracks and the their timing, and back tracking them to a common point in space and time. Comparing the beam time with the RF time provides the experiment with the correct beam bunch which should be centered at zero. An example of what this distribution looks like and the cut used for it is given in Figure 4.1.

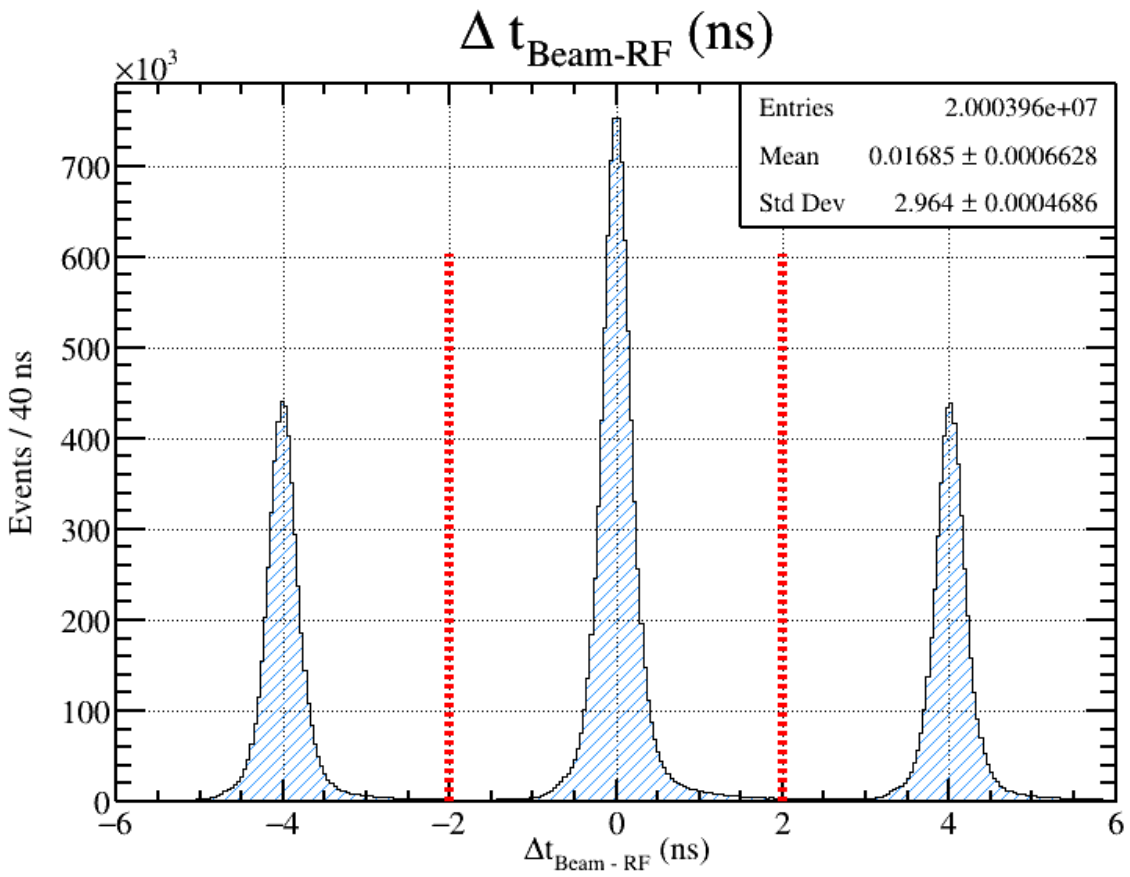

Figure 4.1: An example histogram of beam time as compared to the reported Radio Frequency (RF) time. In the plot there are three peaks, all of which are separated by four nanoseconds. Also included in the plot are two red dashed cut lines at ±2 ns. These cut lines will select the beam time which agrees with the RF and will reject the other out of time beam particles.

The last cut that was made on the beam photons was the observed beam energy. Although this cut does not technically fall under the category of a particle identification, it is included in this section because it was used as a prerequisite for the rest of this analysis. Since this study will ultimately focus on a reaction which requires a high 't' momentum transfer, it is natural to only allow beam photons with high momentum to begin with. This, coupled with the fact that low energy photons produce low statistics for this channel, is the reason why a beam energy cut of $Beam_E \geq 7.5$ GeV was enforced early in the analysis. It should also be noted that this analysis will include a beam asymmetry study for strangeonia which will force the beam energy to be within the coherent peak region ($8.0GeV - 8.8GeV$). An example beam energy distribution with the

associated cut is given in Figure 4.2.

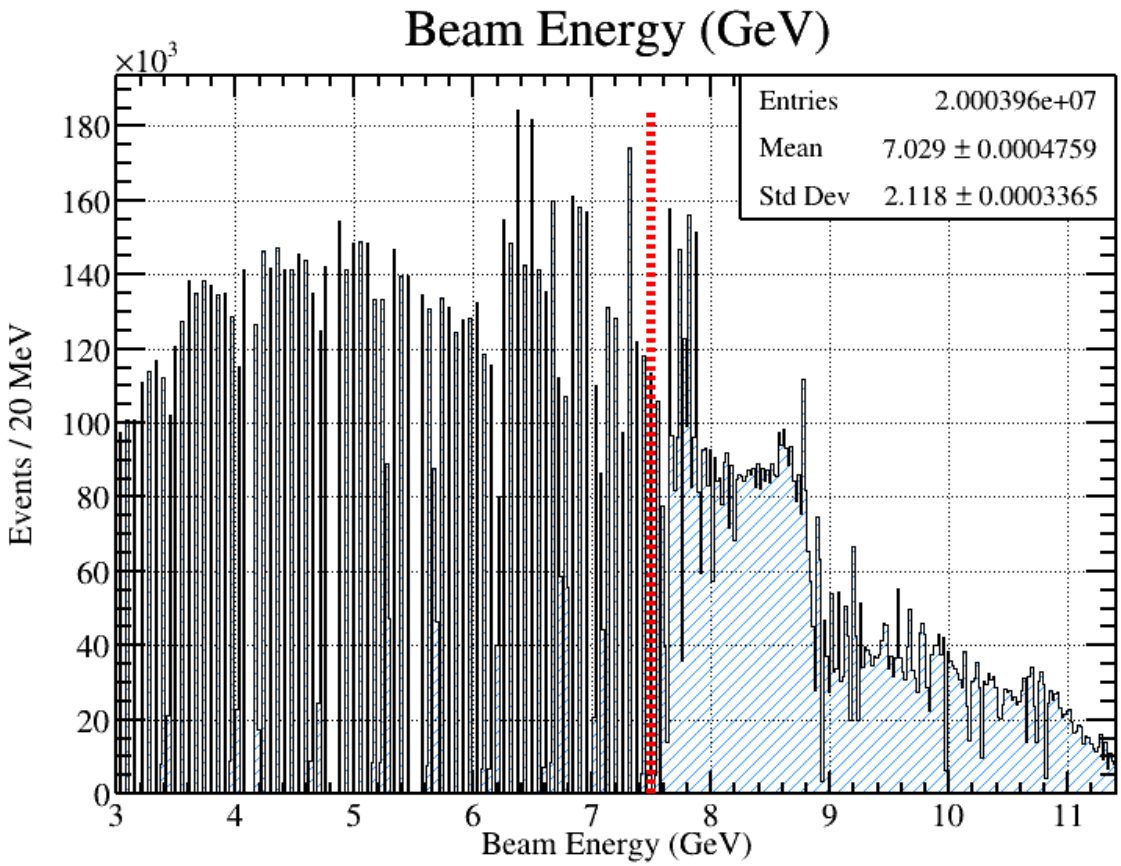

Figure 4.2: An example histogram of the beam energy distribution at GlueX. One can easily notice the large amount of statistics present around the coherent peak region ($8.0GeV - 8.8GeV$) and energies above it. Also contained in the image is a red dashed line which represents the cut value used on this data to select beam energies above 7.5 GeV.

Target Proton. There are two cuts needed to select the initial state proton. Both of these cuts enforce the reconstructed vertex for all final state particles to be within the geometric volume of the target chamber. Since this analysis does not contain a particle lifetime which would result in a detached vertex, it is imperative to remove backgrounds from other channels that may have this feature, such as excited baryons with a strange quark. An example of what the reconstructed vertex for the final state photons looks like in the z direction (along the beam direction) and in the x-y plane (transverse to the beam direction), as well as the associated cut values, is given in Figure 4.3.

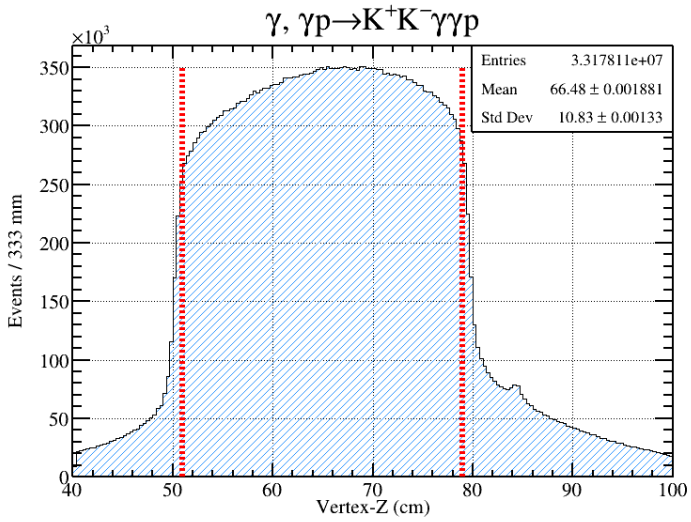

(a) Reconstructed vertex position along the beam direction for γ gamma candidates with cut lines at 51 and 79 cm.

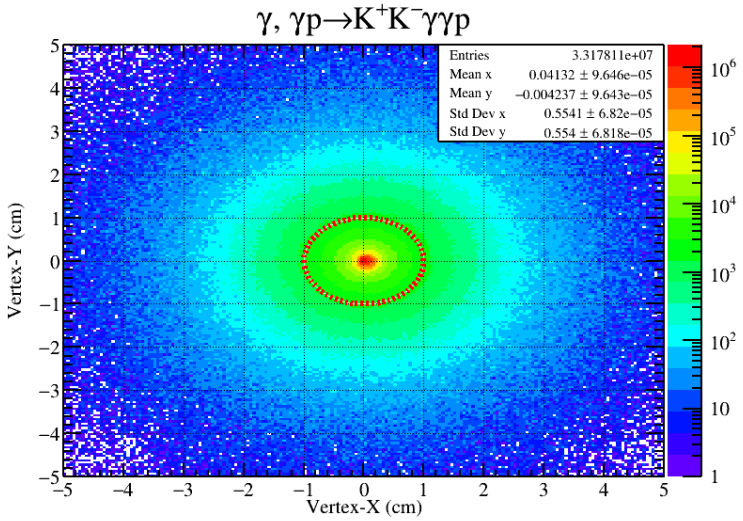

(b) Reconstructed vertex position transverse to the the beam direction for γ gamma candidates with cut a line at 1 cm in radial distance.

Figure 4.3: An example of what a reconstructed vertex distribution looks like for a final state γ in the reaction $\gamma p \to pK^+K^-\gamma_1\gamma_2$. The upper image is the reconstructed vertex position along the beam line, or z axis; and the lower image is the reconstructed vertex position in the directions transverse to the beam line. Both figures contain red dashed lines which represent the cut values for all reconstructed final state particles. In the z direction the cut values are $51cm \leq V_z \leq 79cm$, and in the transverse direction the cut values are $V_r \leq 1cm$. The z direction cut values are established from Log Entry 3456336 from a Spring 2017 empty target run. The transverse cuts are simply established by considering the geometric size of the target chamber.

4.1.3 Identification of Final State Particles

Recoil Proton. There are three cuts that were used to identify the recoil proton. One of the cuts is a standard dE/dX cut, which separates some of the slow moving protons from other particles of positive charge such as e^+, π^+, and K^+. Due to the higher mass of the proton in comparison to the other particles with positive charge, the proton will tend to lose more energy inside of the Central Drift Chamber. The second cut is to enforce the reconstructed vertex position of the charged proton track came from inside the target chamber. This cut is used to eliminate any background from particles that may have a detached vertex. The cut used is identical to those found and described in the Target section. The third and final cut that is used to identify the proton is the timing from the BCAL, FCAL, and TOF. An example of what these distributions look like as a function of momentum is given in Figure [4.4]. Since the data has a lot of pion background in these plots, it is difficult to determine what the proper timing cuts should be for all of the sub detectors. Due to this, a Monte Carlo sample of $\gamma p \to pX; X \to \phi\eta; \phi \to K^+K^-; \eta \to \gamma\gamma$ was generated and then reconstructed. This greatly reduces the background that is present in the timing plots and therefore can be used to estimate a proper timing cut for the proton and the sub detectors used to measure its time. Examples of these distributions and their associated projections onto the timing axis is given in Figure [4.5] through Figure [4.10]. A summary of all of the timing cuts used for the proton as well as all other final state particles is given in Table [4.1].

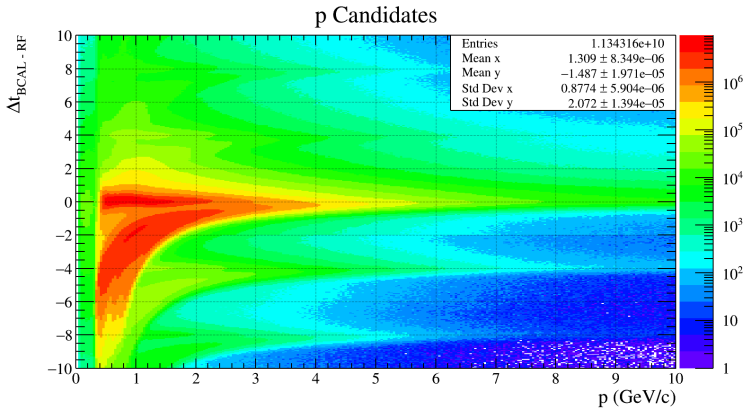

(a) Δ T Vs P for Proton candidates that have the Barrel Calorimeter as the timing detector.

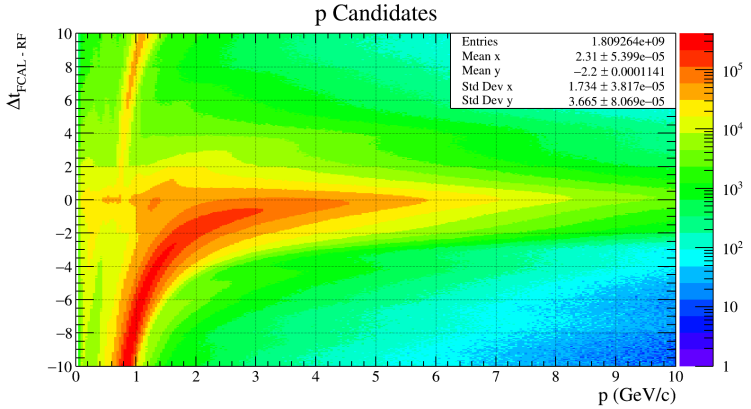

(b) Δ T Vs P for Proton candidates that have the Forward Calorimeter as the timing detector.

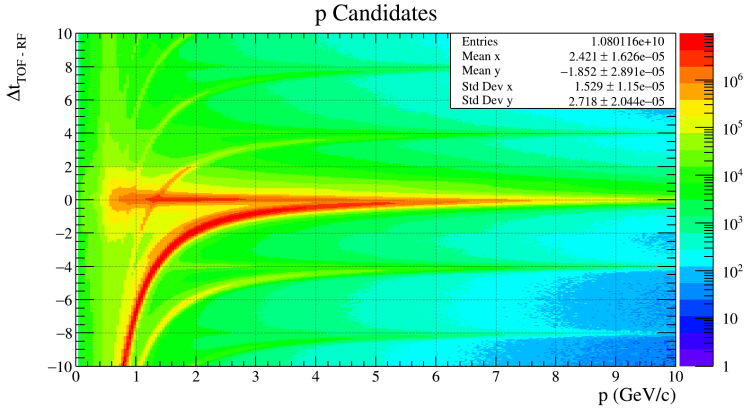

(c) Δ T Vs P for Proton candidates that have the Time of Flight as the timing detector.

Figure 4.4: Timing plots for proton candidates at GlueX. Protons are identified by selecting the horizontal band centered about $\Delta T = 0$. The curved line deviating below the horizontal proton line comes from miss identified π^+ tracks. The additional curved lines above and below $\Delta T = 0$ come from π^+ tracks that are associated with the wrong RF bunch.

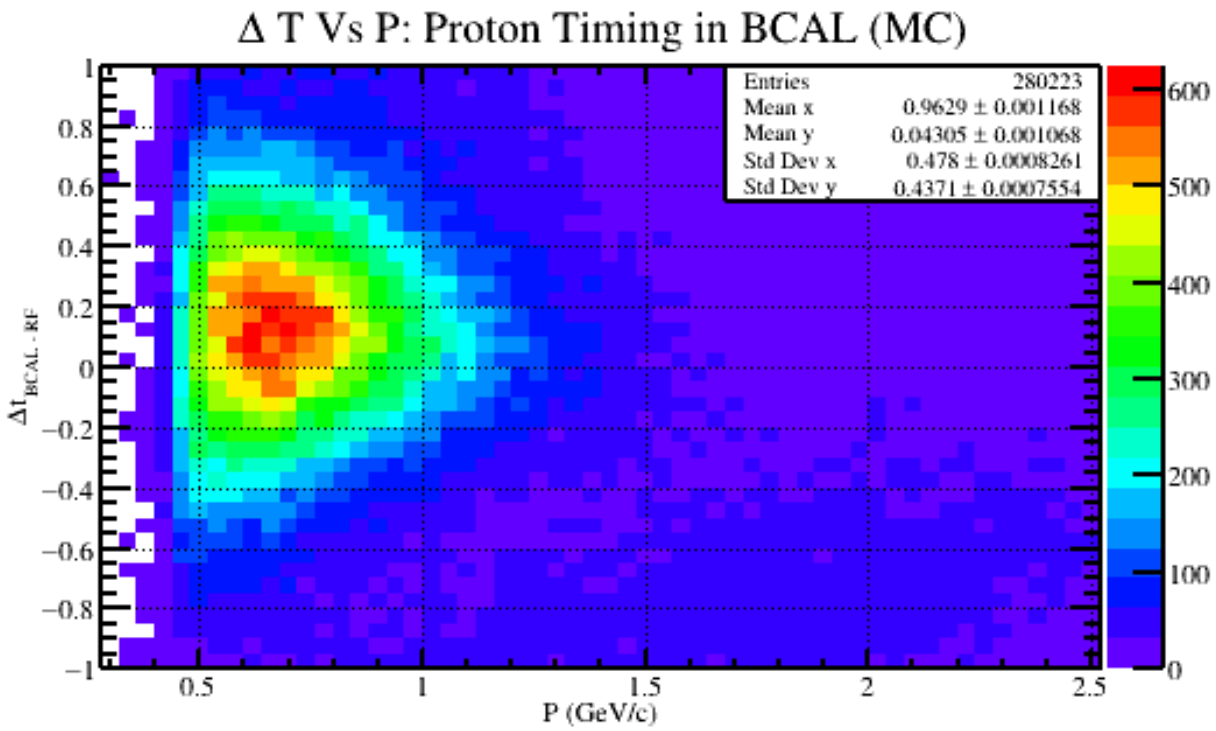

Figure 4.5: A timing plot for generated protons after reconstruction. The horizontal axis is the reconstructed momentum of the proton and the vertical axis is the timing difference between the BCAL and RF. The enhancement of statistics in the lower right portion of the plot comes from miss identified kaons that were also included in the Monte Carlo.

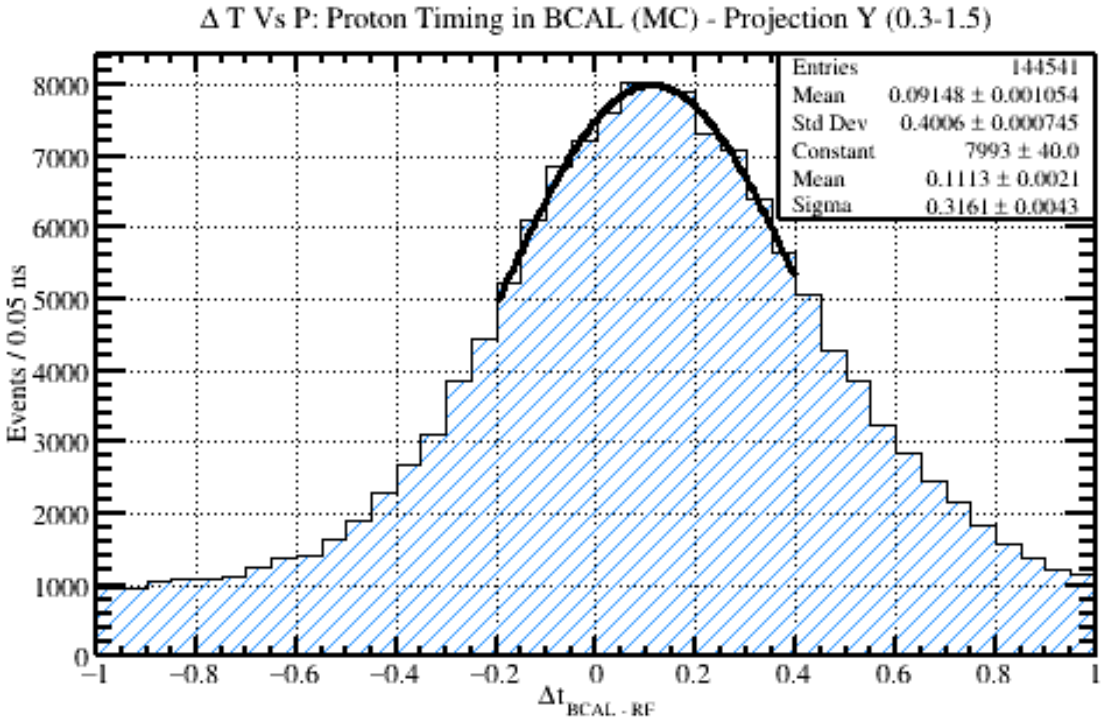

Figure 4.6: A projection of the statistics from Figure [4.5] onto the vertical (timing) axis between the momentum range of 0.3-1.5 GeV/C. This projection range was chosen so that the distortion from the lower kaon band was minimized. A Gaussian fit was performed and is included in the figure where the mean and width of the distribution are given in the legend.

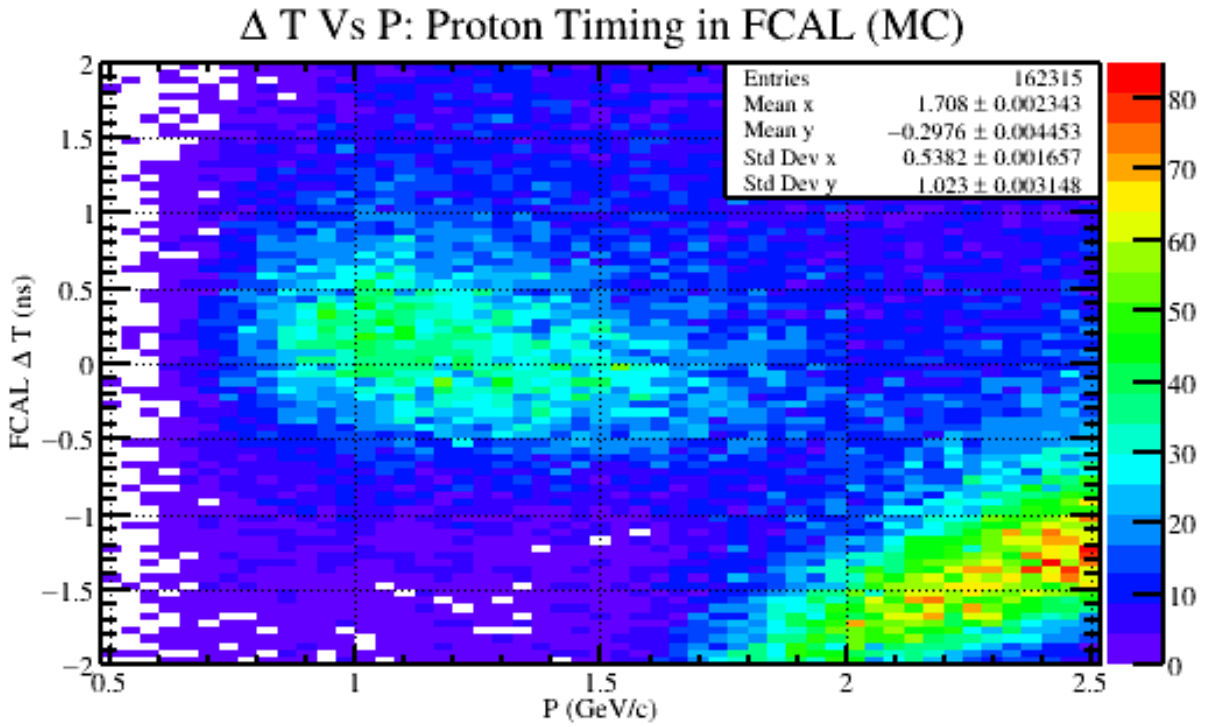

Figure 4.7: A timing plot for generated protons after reconstruction. The horizontal axis is the reconstructed momentum of the proton and the vertical axis is the timing difference between the FCAL and RF. The enhancement of statistics in the lower right portion of the plot comes from miss identified kaons that were also included in the Monte Carlo.

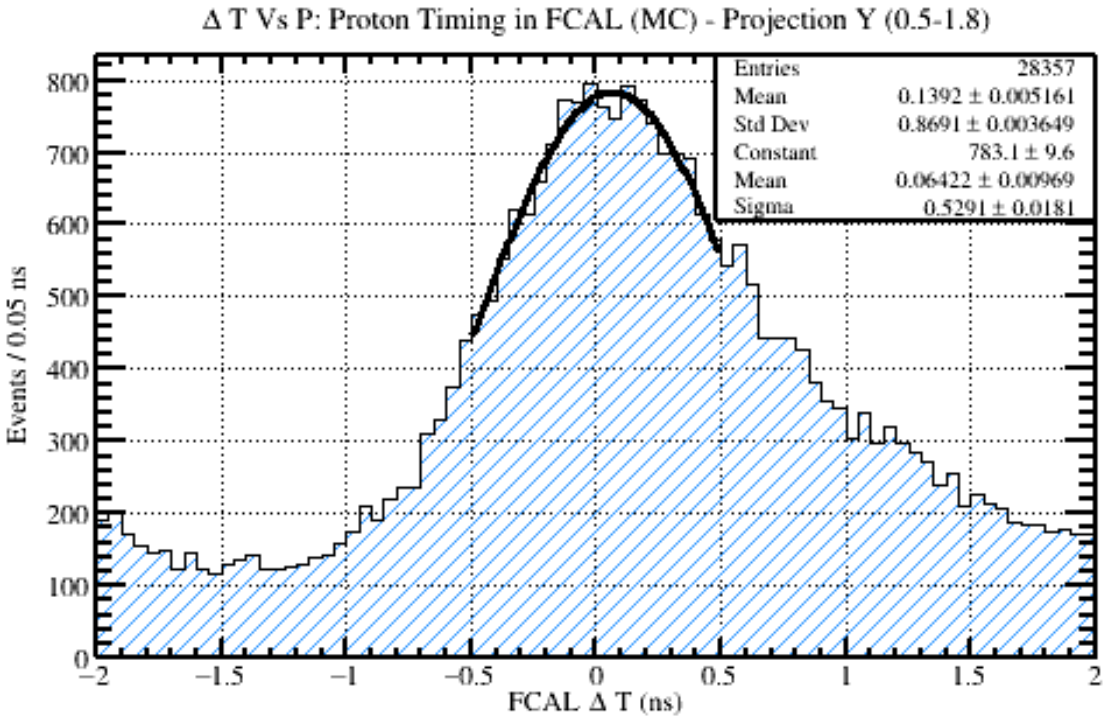

Figure 4.8: A projection of the statistics from Figure [4.7] onto the vertical (timing) axis between the momentum range of 0.5-1.8 GeV/C. This projection range was chosen so that the distortion from the lower kaon band was minimized. A Gaussian fit was performed and is included in the figure where the mean and width of the distribution are given in the legend.

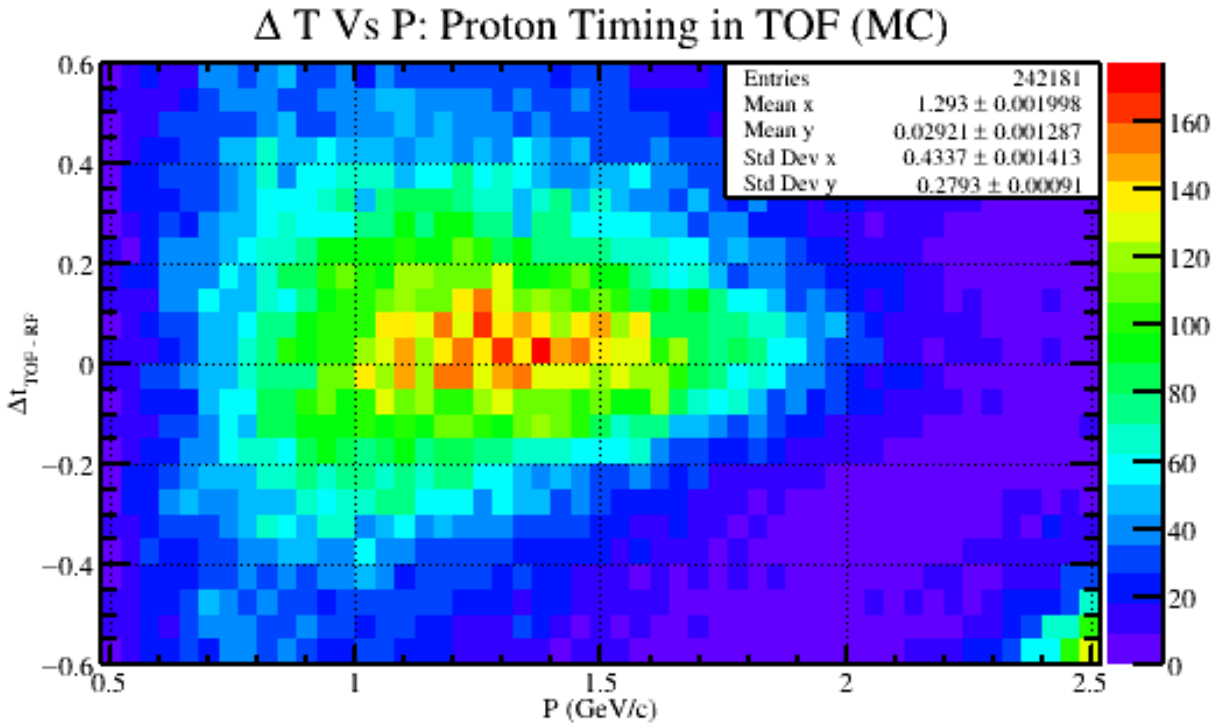

Figure 4.9: A timing plot for generated protons after reconstruction. The horizontal axis is the reconstructed momentum of the proton and the vertical axis is the timing difference between the TOF and RF. The enhancement of statistics in the lower right portion of the plot comes from miss identified kaons that were also included in the Monte Carlo.

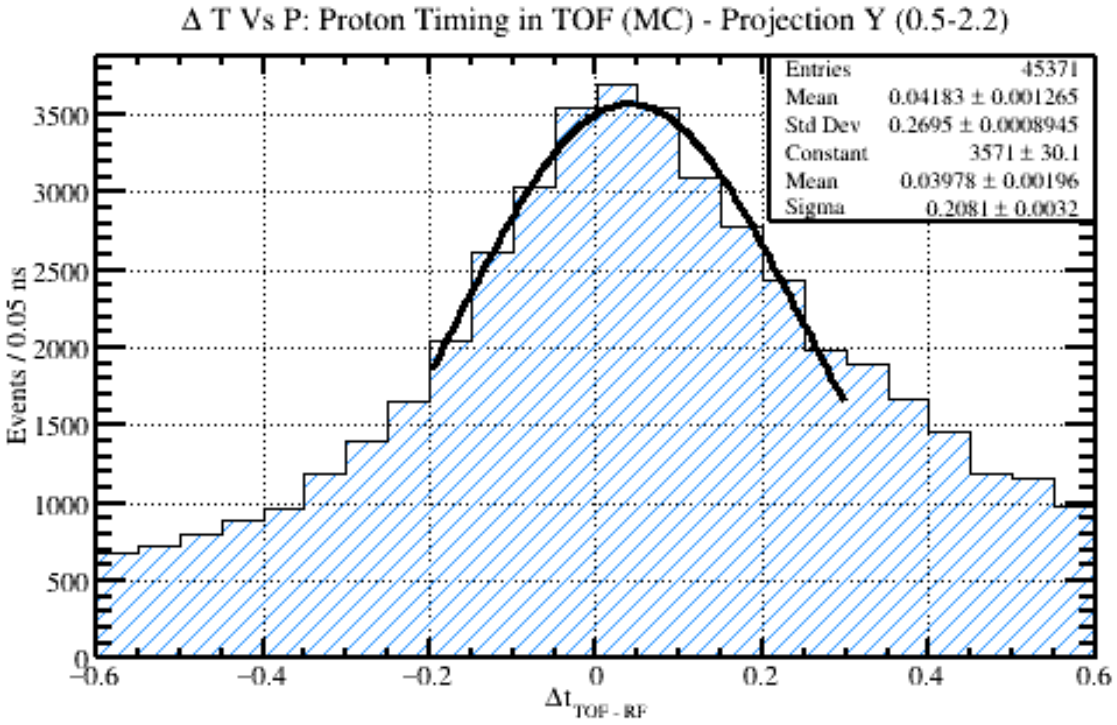

Figure 4.10: A projection of the statistics from Figure [4.9] onto the vertical (timing) axis between the momentum range of 0.5-1.8 GeV/C. This projection range was chosen so that the distortion from the lower kaon band was minimized. A Gaussian fit was performed and is included in the figure where the mean and width of the distribution are given in the legend.

K^+. There are two cuts that were used to identify the final state K^+. The first cut is to enforce the reconstructed vertex position of the K^+ track came from inside the target chamber. This cut is used to eliminate any parent state of the K^+ that may have a longer lifetime and therefore a detached vertex. The cut used is identical to those found and described in the Target section. The other cut that is used to identify the K^+ is the timing from the BCAL, FCAL, and TOF. An example of what these distributions look like as a function of momentum is given in Figure [4.11]. Since the data has a lot of pion and proton background in these plots, it is difficult to determine what the proper timing cuts should be for all of the sub detectors. Due to this, a Monte Carlo sample of $\gamma p \to pX; X \to \phi\eta; \phi \to K^+K^-; \eta \to \gamma\gamma$ was generated and then reconstructed. This greatly reduces the background that is present in the timing plots and therefore can be used to estimate a proper timing cut for the K^+ and the sub detectors used to measure its time. Examples of these distributions and their associated projections onto the timing axis is given in Figure [4.12] through Figure [4.17]. It should be noted that in many of the Monte Carlo plots, there appears to be an additional band from a particle with less mass. This is a consequence of using the *hdgeant* simulator, and the fact that it will decay particles while in flight. Therefore, the band inside the Monte Carlo plots arises from the weak decay of a kaon to a muon and a neutrino. A summary of all of the timing cuts used for the K^+ as well as all other final state particles is given in Table [4.1].

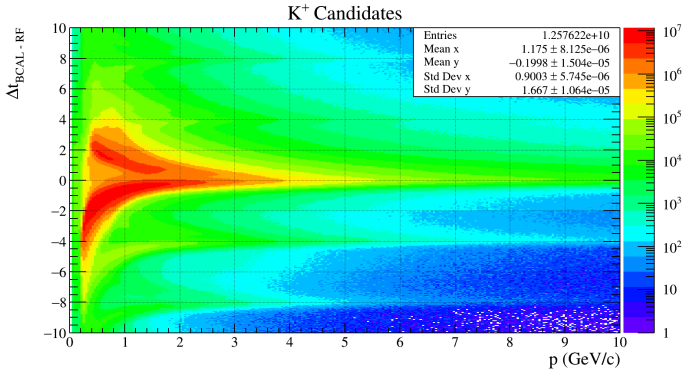

(a) Δ T Vs P for K^+ candidates that have the Barrel Calorimeter as the timing detector.

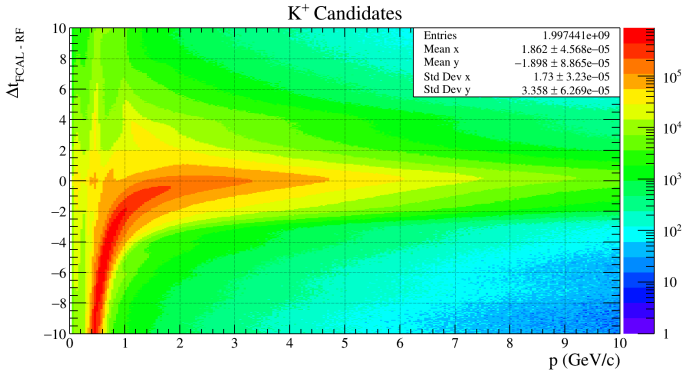

(b) Δ T Vs P for K^+ candidates that have the Forward Calorimeter as the timing detector.

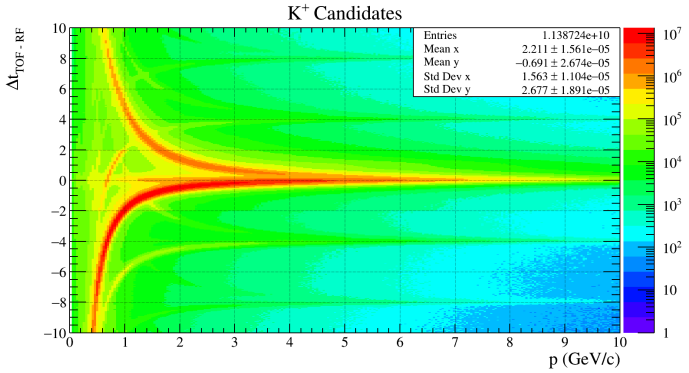

(c) Δ T Vs P for K^+ candidates that have the Time of Flight as the timing detector.

Figure 4.11: Timing plots for K^+ candidates at GlueX. K^+ are identified by selecting the horizontal band centered about $\Delta T = 0$. The curved line deviating below the horizontal K^+ line comes from miss identified π^+ tracks, and the curved line deviating above the horizontal K^+ line comes from miss identified proton tracks. The additional curved lines above and below $\Delta T = 0$ come from π^+ and proton tracks that are associated with the wrong RF bunch.

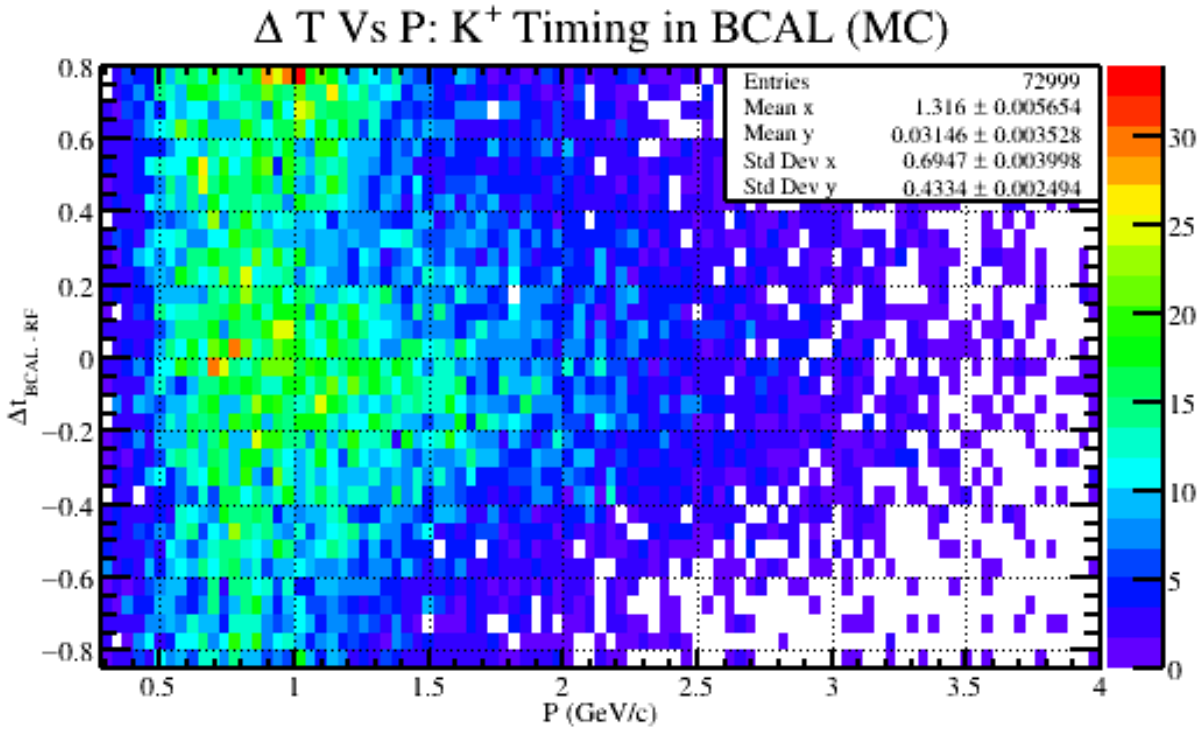

Figure 4.12: A timing plot for generated K^+ after reconstruction. The horizontal axis is the reconstructed momentum of the K^+ and the vertical axis is the timing difference between the BCAL and RF. It should be noted that the statistics in this sampling are smaller than other plots. This is due to the fact that the kinematics of the generated channel prefer to have the kaons moving in the forwards direction; and therefore provide few timing hits in the BCAL. Additionally, the extra statistics present in the upper left portion of the graph are due to protons included in this Monte Carlo sample.

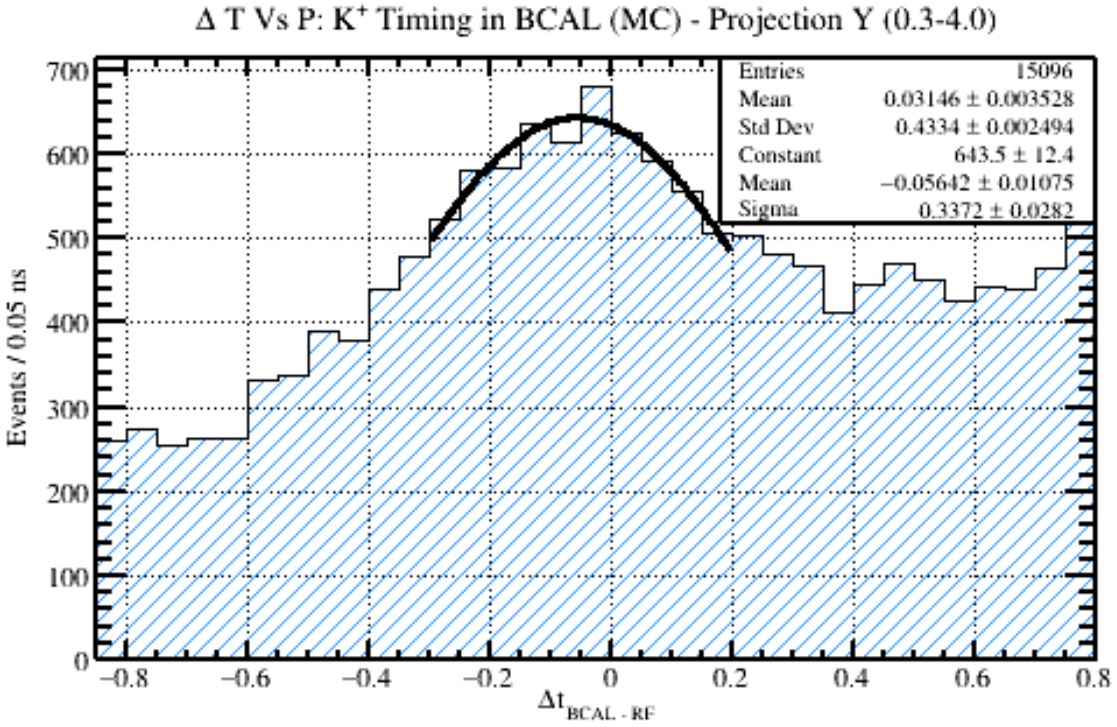

Figure 4.13: A projection of the statistics from Figure [4.12] onto the vertical (timing) axis between the momentum range of 0.3-4.0 GeV/C. A Gaussian fit was performed and is included in the figure where the mean and width of the distribution are given in the legend. The distortion of statistics towards the higher timing differences is due to protons included in this Monte Carlo study.

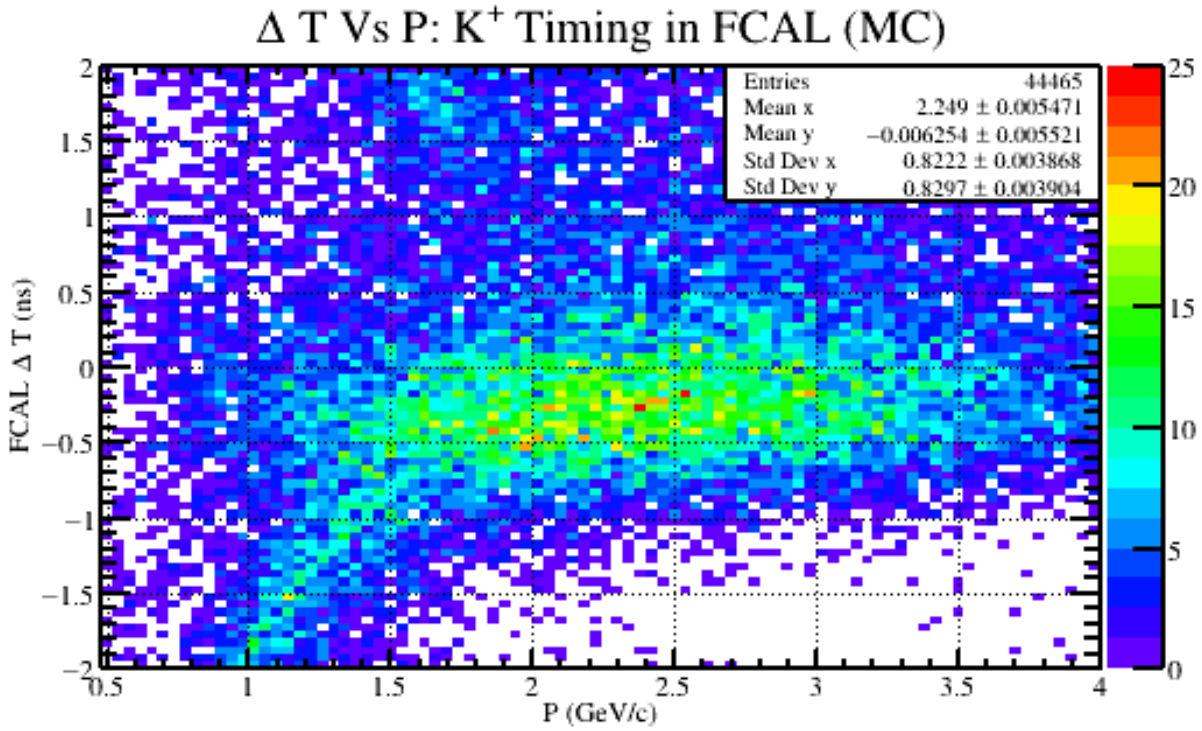

Figure 4.14: A timing plot for generated K^+ after reconstruction. The horizontal axis is the reconstructed momentum of the K^+ and the vertical axis is the timing difference between the FCAL and RF. The curved band that appears below the K^+ band around 1.5 GeV/c and lower comes from μ^+. Although muons were not explicitly generated, the computer program hdgeant (derived from geant) allows for some fraction of kaons to decay weakly while in flight; resulting in a observed muons.

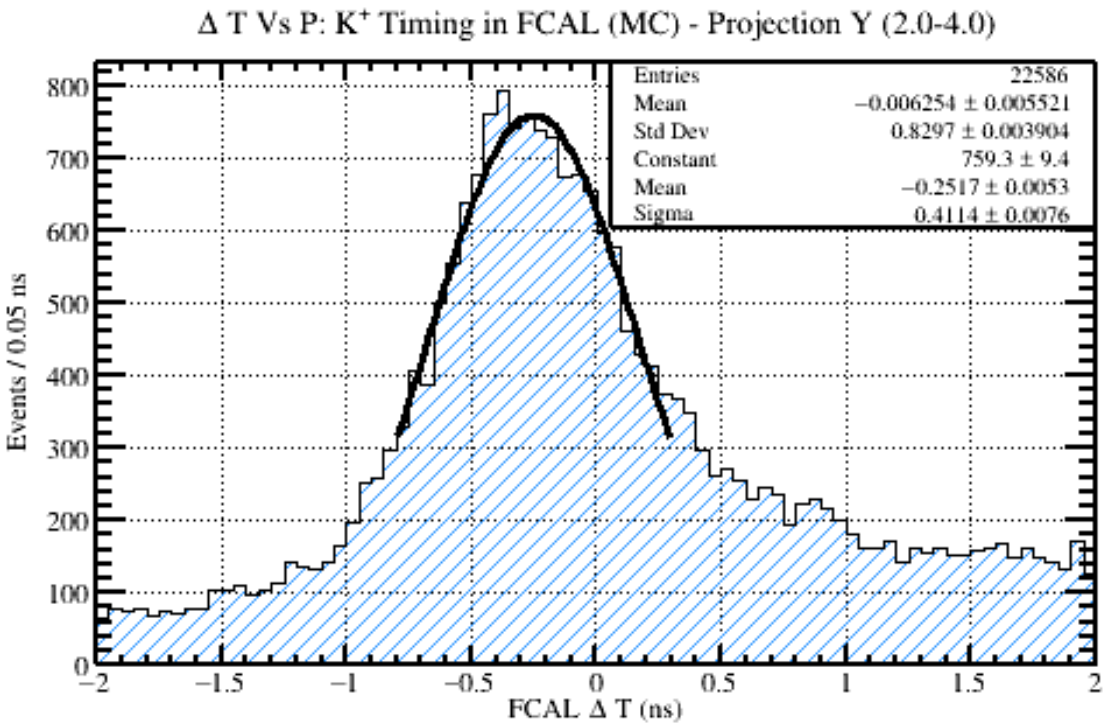

Figure 4.15: A projection of the statistics from Figure [4.14] onto the vertical (timing) axis between the momentum range of 2.0-4.0 GeV/C. This projection range was chosen so that the distortion from the lower muon band and upper proton band was minimized. A Gaussian fit was performed and is included in the figure where the mean and width of the distribution are given in the legend.

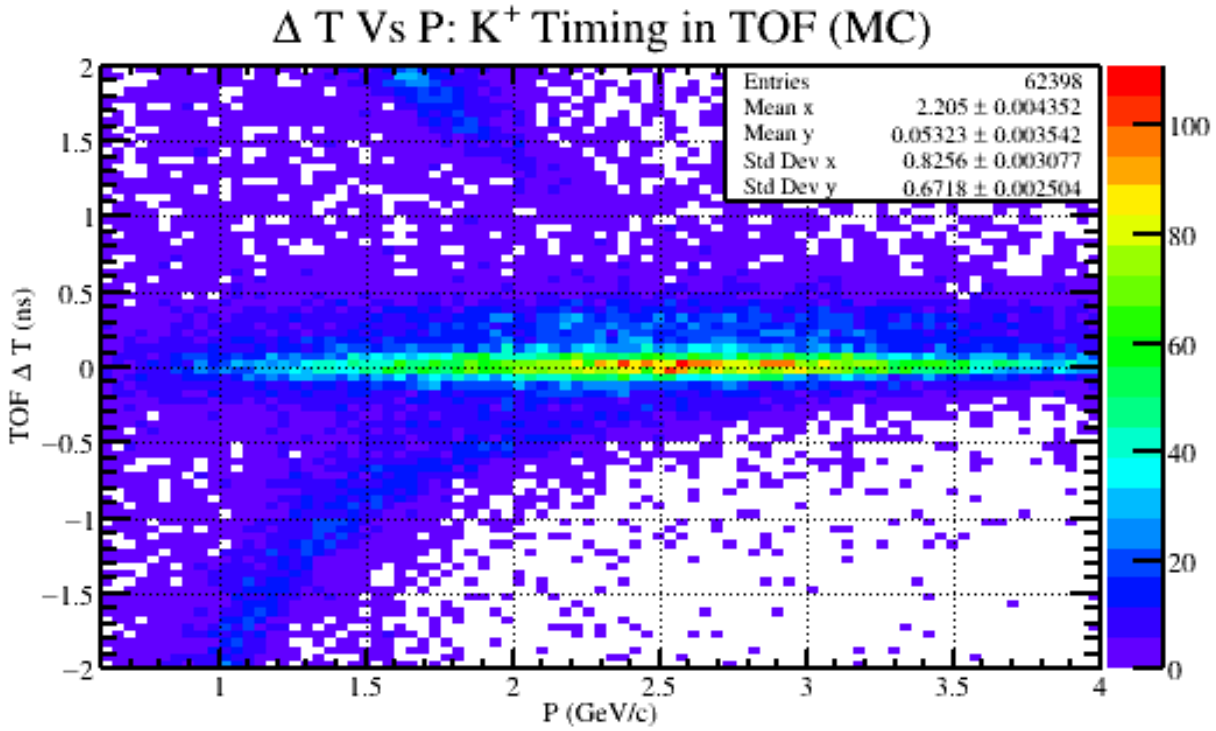

Figure 4.16: A timing plot for generated K^+ after reconstruction. The horizontal axis is the reconstructed momentum of the K^+ and the vertical axis is the timing difference between the TOF and RF. The curved band that appears below the K^+ band around 2.5 GeV/c and lower comes from μ^+; and the band near the top of the plot comes from protons. Although muons were not explicitly generated, the computer program hdgeant (derived from geant) allows for some fraction of kaons to decay weakly while in flight; resulting in an observed muon.

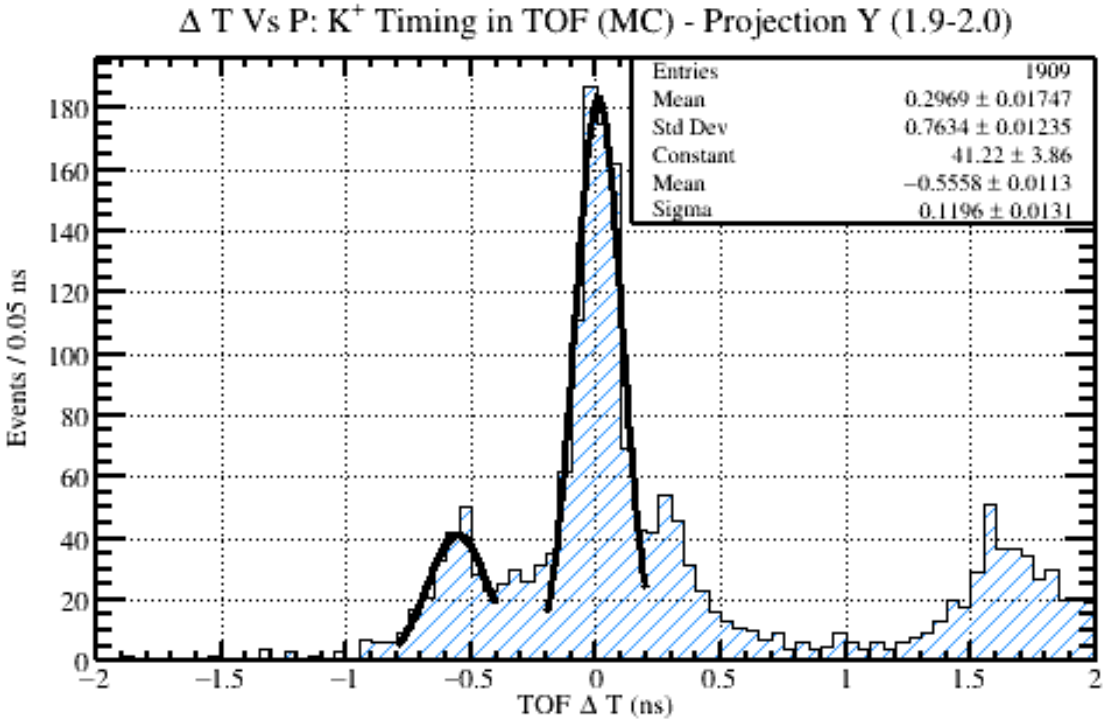

Figure 4.17: A projection of the statistics from Figure [4.16] onto the vertical (timing) axis between the momentum range of 1.9-2.0 GeV/C. This projection range is one out of many that were studied from Figure [4.16]. The purpose of this study is to determine the amount of muon contamination in the kaon band as a function of momentum. The results of this study are provided in Figure [4.18]. Lastly, two Gaussian fits were performed on this data. The mean and width of these Gaussian fits are recorded in Figure [4.18] for each momentum range.

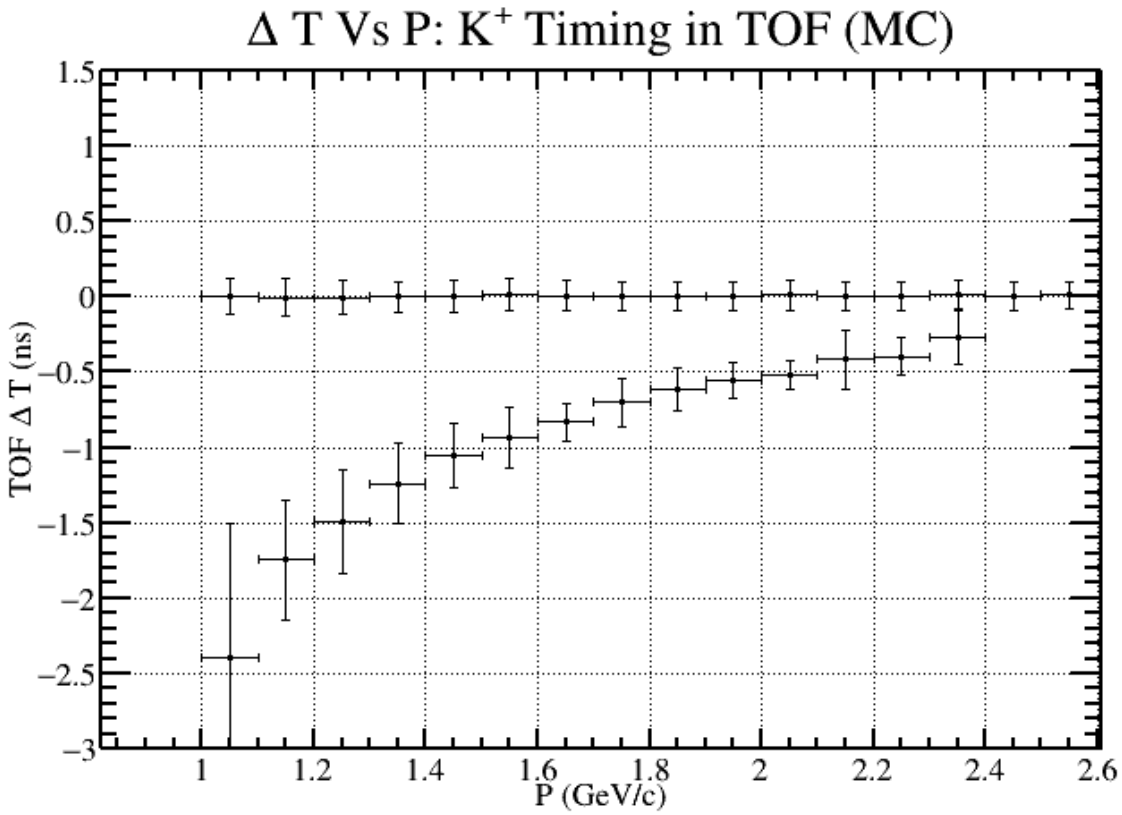

Figure 4.18: The image above is the result of the timing study performed on Figure [4.16]. Using that figure, a number of projection histograms were fit using different momentum ranges. An example of one of these fits is given in Figure [4.17]. The data points close to 0 ΔT correspond to the Gaussian fits performed on the kaon signal, and the data points that approach that band from the bottom correspond to the Gaussian fits performed on the muon signal. The horizontal position of each point is in the middle of the projection range, and the vertical position of each point was assigned based on the mean value of the Gaussian fit for each particle. The horizontal error bars are the size of the projection range, which is always 0.1 GeV/c. The vertical error bars are determined by the width of the Gaussian fits. The average of the widths of the kaon peaks is $0.1ns$ which is the value used to determine the timing cut in Table 4.1.

K^-. Just like its antiparticle, the K^- has two identifying cuts; the vertex and timing cuts.The vertex cut is used to eliminate any parent state of the K^- that may have a longer lifetime and therefore a detached vertex. The cut used is identical to those found and described in the Target section. The timing cuts for the K^- are for the BCAL, FCAL, and TOF sub detectors. Since the timing distributions from data (Figure [4.19]) have too much background in them, a Monte Carlo sample of $\gamma p \to pX; X \to \phi\eta; \phi \to K^+K^-; \eta \to \gamma\gamma$ was generated and then reconstructed. This

greatly reduces the background that is present in the timing plots and therefore can be used to estimate a proper timing cut for the K^- and the sub detectors used to measure its time. Examples of these distributions and their associated projections onto the timing axis is given in Figure [4.20] through Figure [4.25]. It should be noted that in many of the Monte Carlo plots, there appears to be an additional band from a particle with less mass. This is a consequence of using the *hdgeant* simulator, and the fact that it will decay particles from while in flight. Therefore, the band inside the Monte Carlo plots arises from the weak decay of a kaon to a muon and a neutrino. A summary of all of the timing cuts used for the K^- as well as all other final state particles is given in Table [4.1].

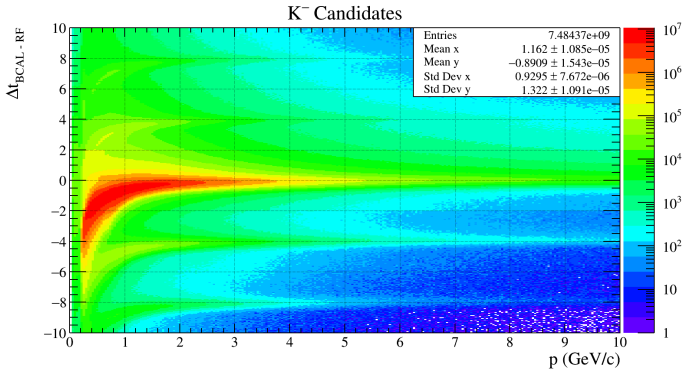

(a) Δ T Vs P for K^- candidates that have the Barrel Calorimeter as the timing detector.

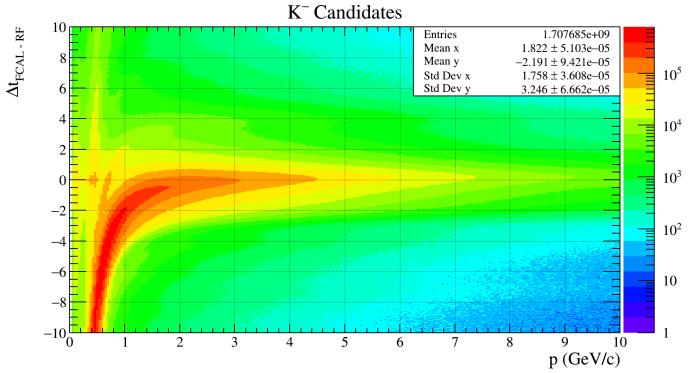

(b) Δ T Vs P for K^- candidates that have the Forward Calorimeter as the timing detector.

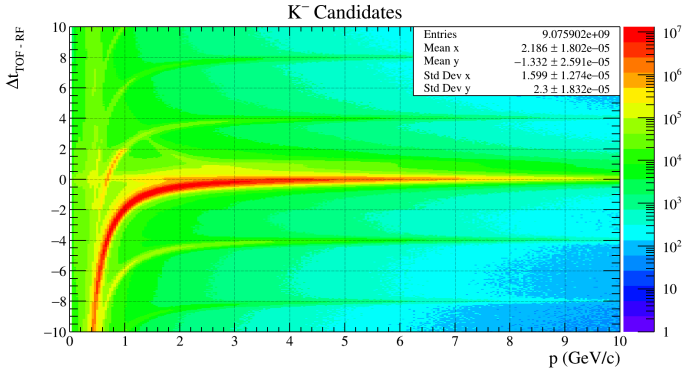

(c) Δ T Vs P for K^- candidates that have the Time of Flight as the timing detector.

Figure 4.19: Timing plots for K^- candidates at GlueX. K^- are identified by selecting the horizontal band centered about $\Delta T = 0$. The curved line deviating below the horizontal K^- line comes from miss identified π^- tracks. The additional curved lines above and below $\Delta T = 0$ come from π^- tracks that are associated with the wrong RF bunch.

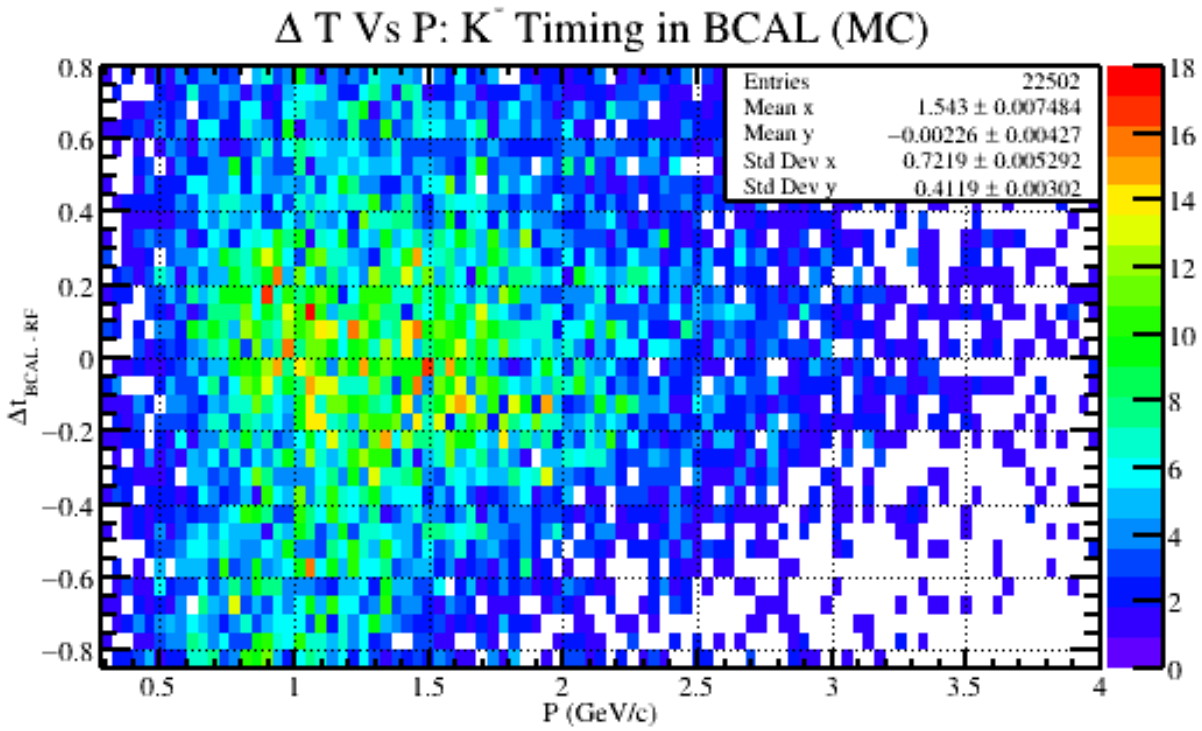

Figure 4.20: A timing plot for generated K^- after reconstruction. The horizontal axis is the reconstructed momentum of the K^- and the vertical axis is the timing difference between the BCAL and RF. It should be noted that the statistics in this sampling are smaller than other plots. This is due to the fact that the kinematics of the generated channel prefer to have the kaons moving in the forwards direction; and therefore provide few timing hits in the BCAL. Additionally, the extra statistics present in the lower left portion of the graph are due to muons. Although muons were not explicitly generated, the computer program hdgeant (derived from geant) allows for some fraction of kaons to decay weakly while in flight; resulting in observed muons.

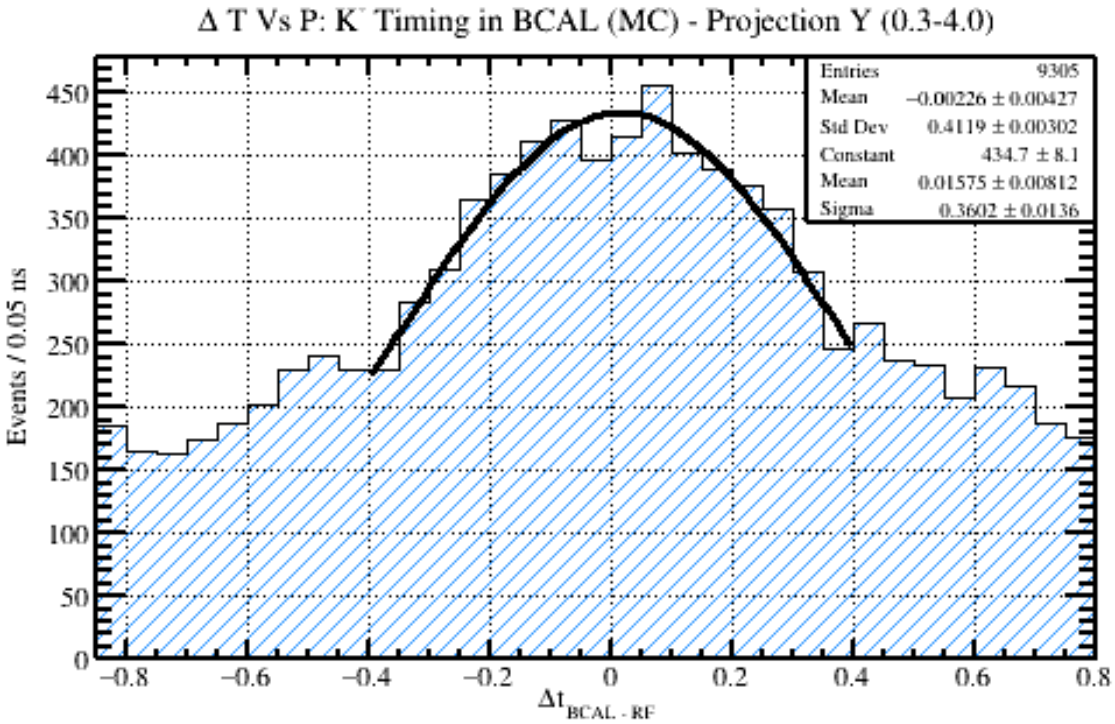

Figure 4.21: A projection of the statistics from Figure [4.20] onto the vertical (timing) axis between the momentum range of 0.3-4.0 GeV/C. A Gaussian fit was performed and is included in the figure where the mean and width of the distribution are given in the legend.

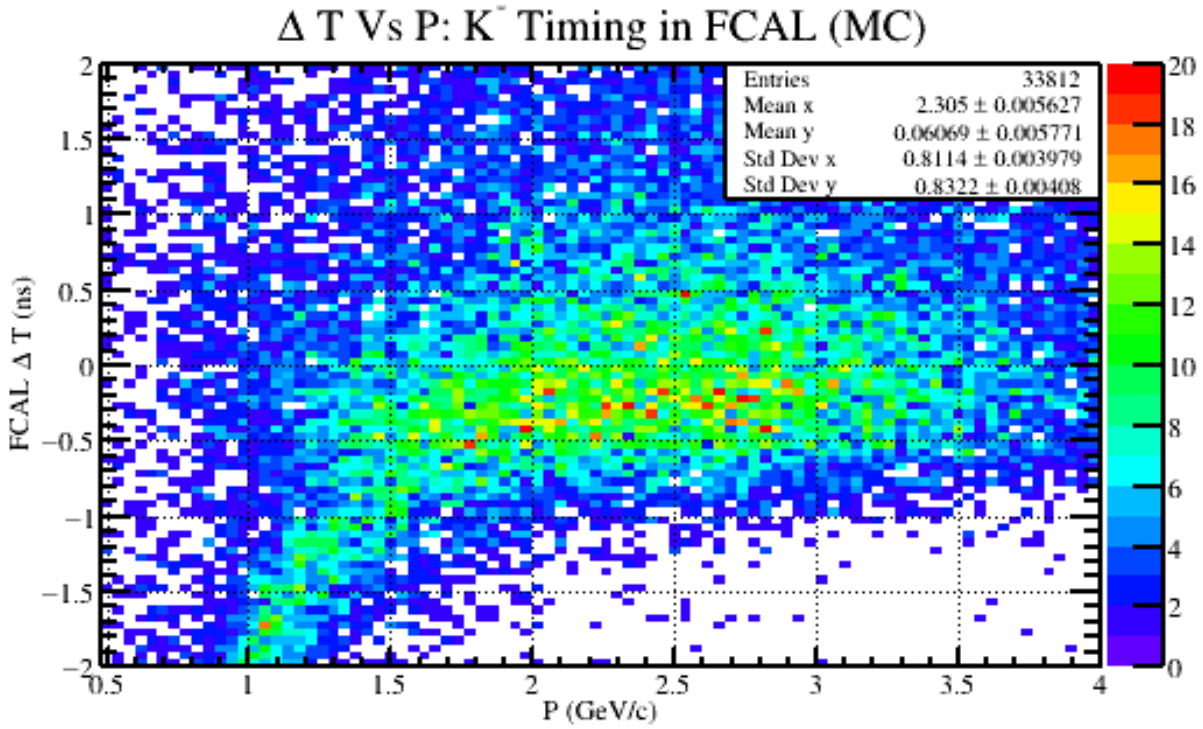

Figure 4.22: A timing plot for generated K^- after reconstruction. The horizontal axis is the reconstructed momentum of the K^- and the vertical axis is the timing difference between the FCAL and RF. The curved band that appears below the K^- band around 1.5 GeV/c and lower comes from μ^-. Although muons were not explicitly generated, the computer program hdgeant (derived from geant) allows for some fraction of kaons to decay weakly while in flight; resulting in an observed muon.

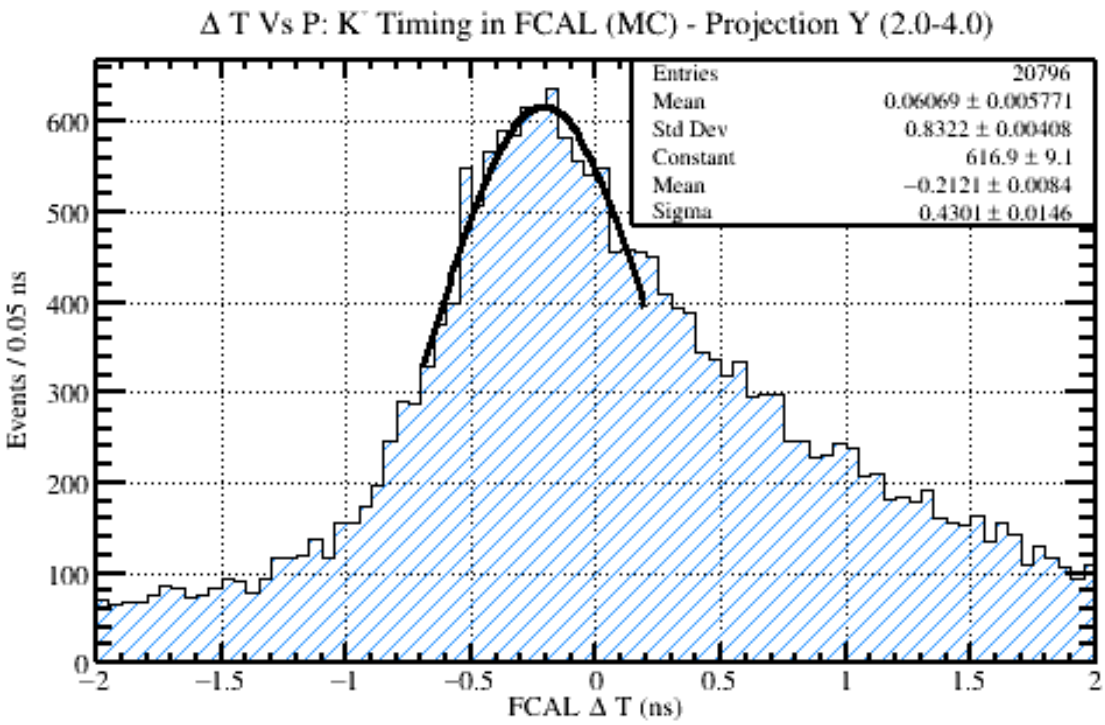

Figure 4.23: A projection of the statistics from Figure [4.22] onto the vertical (timing) axis between the momentum range of 2.0-4.0 GeV/C. This projection range was chosen so that the distortion from the lower muon band was minimized. A Gaussian fit was performed and is included in the figure where the mean and width of the distribution are given in the legend.

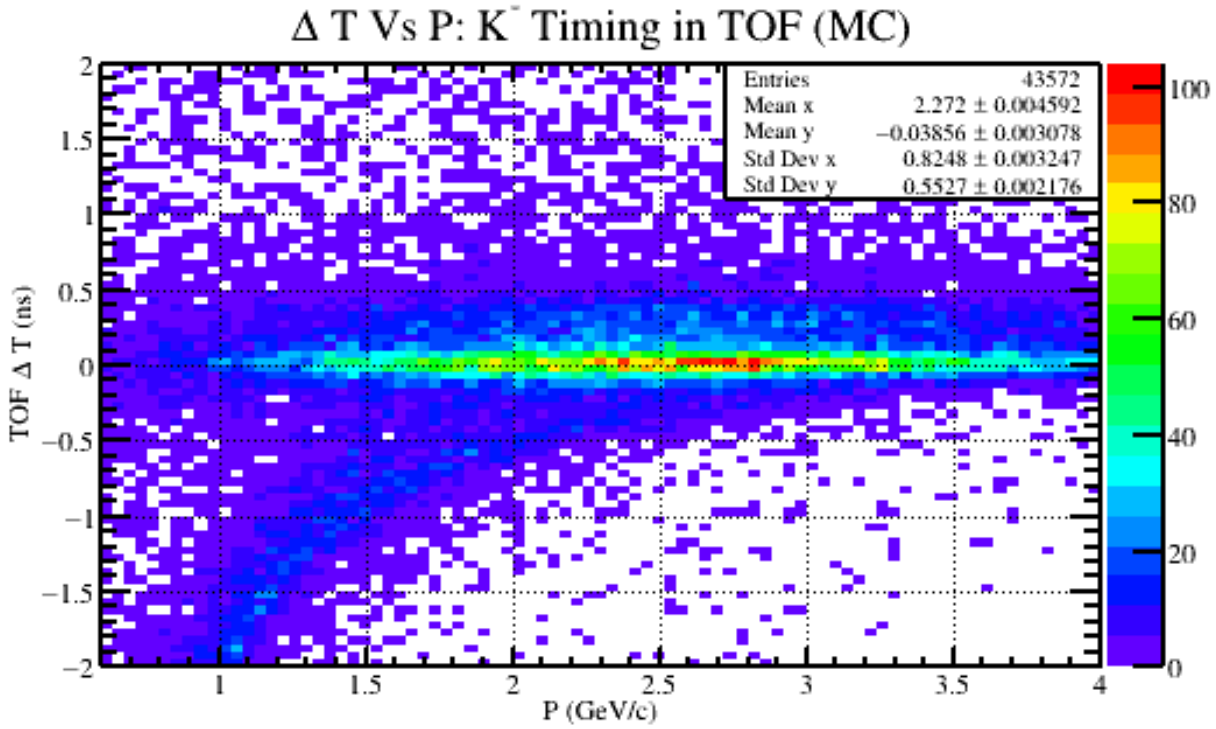

Figure 4.24: A timing plot for generated K^- after reconstruction. The horizontal axis is the reconstructed momentum of the K^- and the vertical axis is the timing difference between the TOF and RF. The curved band that appears below the K^- band around 2.5 GeV/c and lower comes from μ^-. Although muons were not explicitly generated, the computer program hdgeant (derived from geant) allows for some fraction of kaons to decay weakly while in flight; resulting in an observed muon.

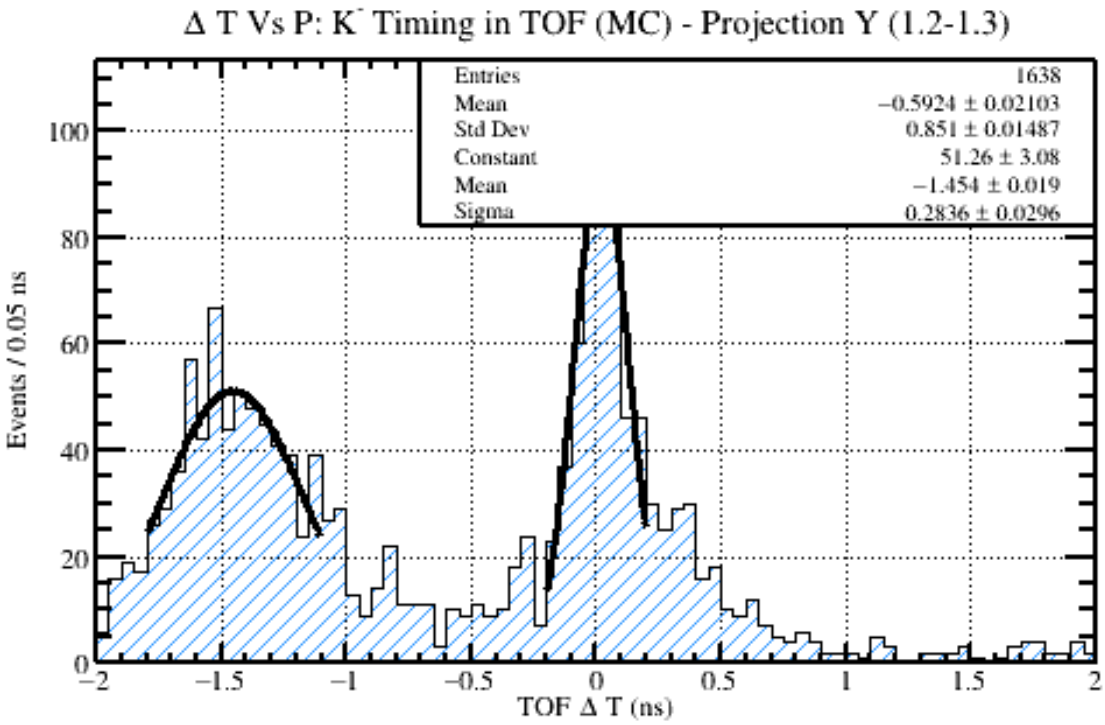

Figure 4.25: A projection of the statistics from Figure [4.24] onto the vertical (timing) axis between the proton momentum range of 1.2-1.3 GeV/C. This projection range is one out of many that were studied from Figure [4.24]. The purpose of this study is to determine the amount of muon contamination in the kaon band as a function of momentum. The results of this study are provided in Figure [4.26]. Lastly, two Gaussian fits were performed on this data. The mean and width of these Gaussian fits are recorded in Figure [4.26] for each momentum range.

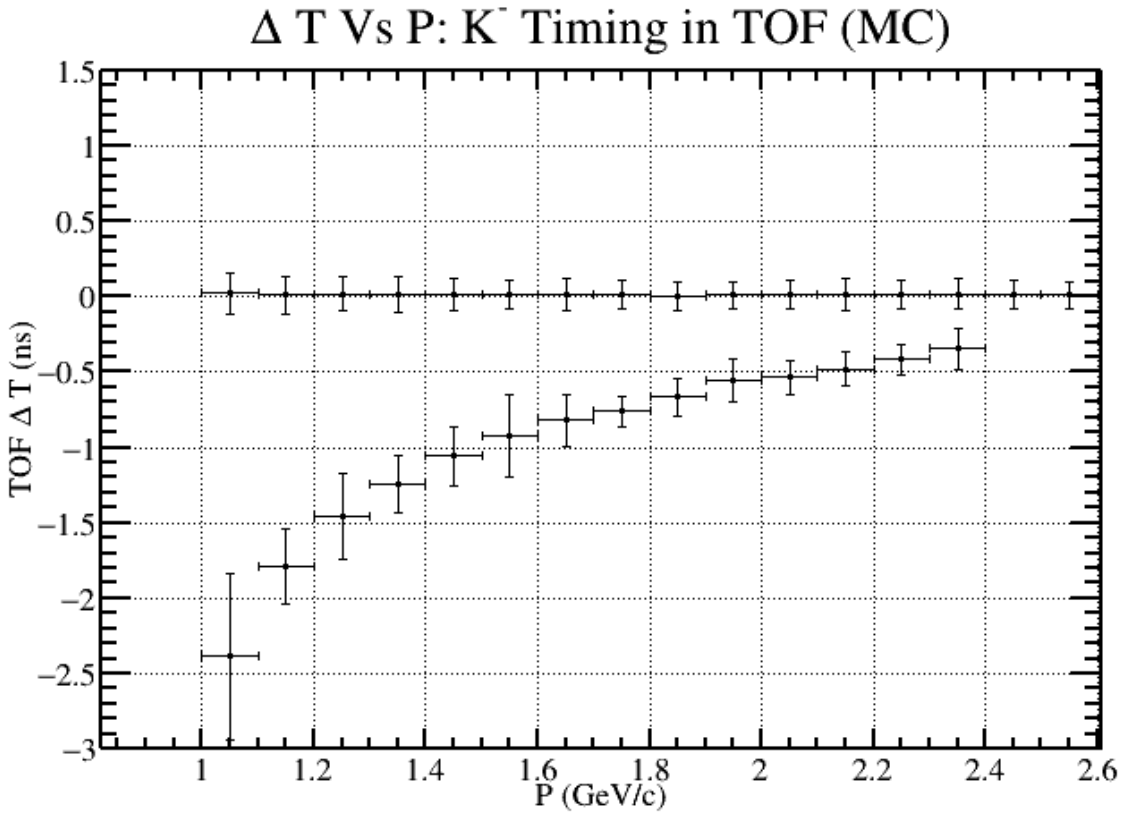

Figure 4.26: The image above is the result of the timing study performed on Figure [4.24]. Using that figure, a number of projection histograms were fit using different momentum ranges. An example of one of these fits is given in Figure [4.25]. The data points close to 0 ΔT correspond to the Gaussian fits performed on the kaon signal, and the data points that approach that band from the bottom correspond to the Gaussian fits performed on the muon signal. The horizontal position of each point is in the middle of the projection range, and the vertical position of each point was assigned based on the mean value of the Gaussian fit for each particle. The horizontal error bars are the size of the projection range, which is always 0.1 GeV/c. The vertical error bars are determined by the width of the Gaussian fits. The average of the widths of the kaon peaks is $0.1ns$ which is the value used to determine the timing cut in Table 4.1.

γ. Unlike the other final state particles with charge, the final state photons only have two timing cuts and no vertex cuts. There are no vertex cuts because the photon has no net charge and can therefore not leave a charged track inside the detector to reconstruct. Without a charged track to reconstruct, it is impossible for the reconstruction to backtrack where the particle originated from. In addition, there is also no timing cut for the TOF. This is due to the fact that the time of flight can only interact with charged particles, and therefore cannot interact with photons.

The timing cuts for the γ only come from the BCAL, FCAL. Since the timing distributions from data (Figure [4.27]) have too much neutron background in them, a Monte Carlo sample of $\gamma p \to pX; X \to \phi\eta; \phi \to K^+K^-; \eta \to \gamma\gamma$ was generated and then reconstructed. This greatly reduces the background that is present in the timing plots and therefore can be used to estimate a proper timing cut for the γ and the sub detectors used to measure its time. Examples of these distributions and their associated projections onto the timing axis is given in Figure [4.28] through Figure [4.31]. A summary of all of the timing cuts used for the photon as well as all other final state particles is given in Table [4.1].

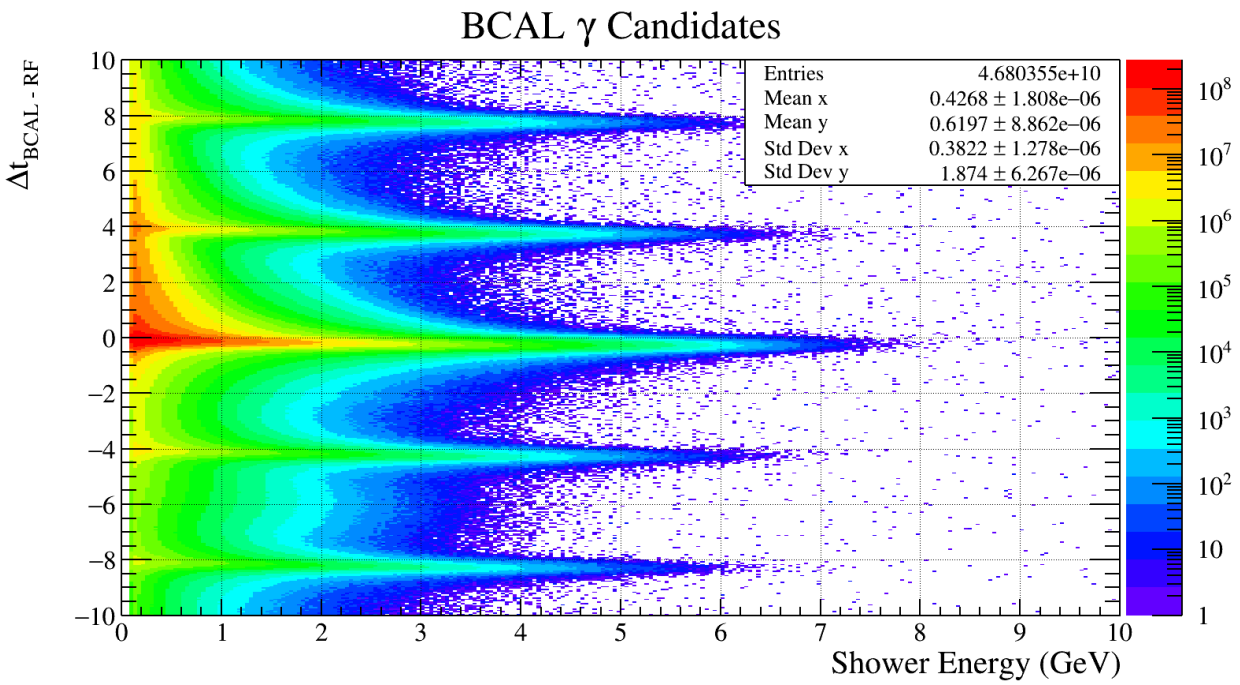

(a) Δ T Vs Shower Energy for γ candidates that have the Barrel Calorimeter as the timing detector.

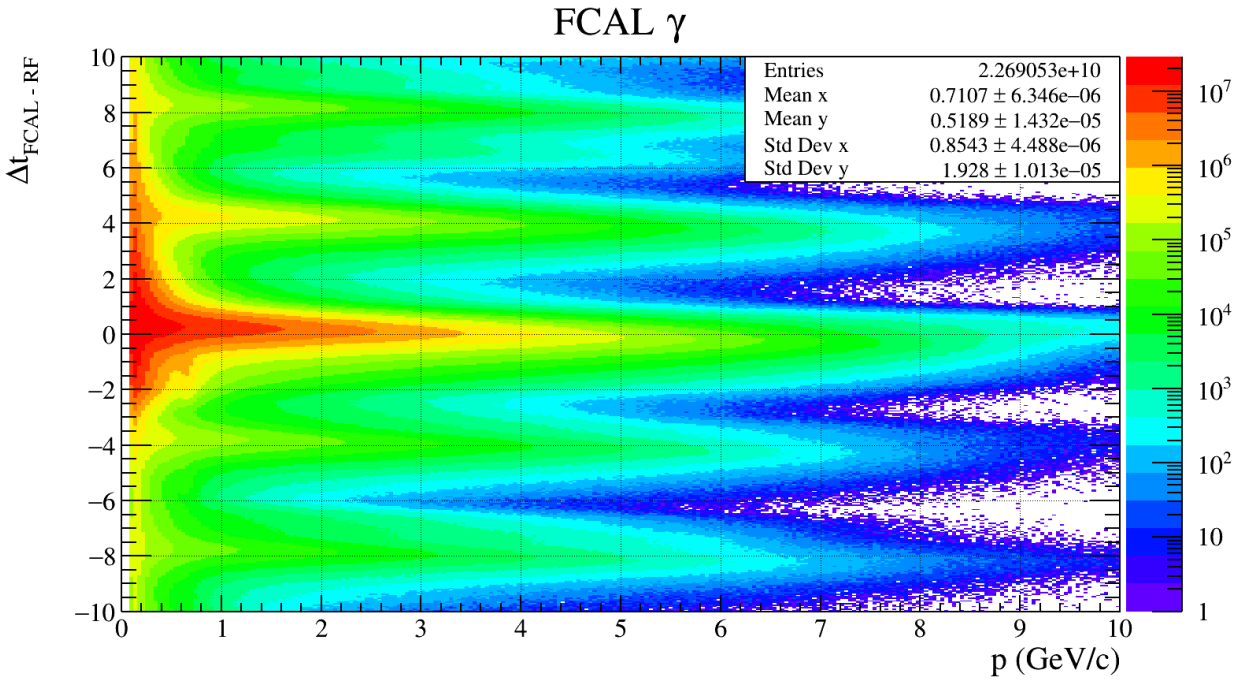

(b) Δ T Vs Shower Energy for γ candidates that have the Forward Calorimeter as the timing detector.

Figure 4.27: Timing plots for γ candidates at GlueX. γ are identified by selecting the horizontal band centered about $\Delta T = 0$. Large enhancement in statistics at low momentum and out of time with the γ line comes from slow moving and poorly times neutrons. The additional horizontal lines above and below $\Delta T = 0$ come from γ showers that are associated with the wrong RF bunch.

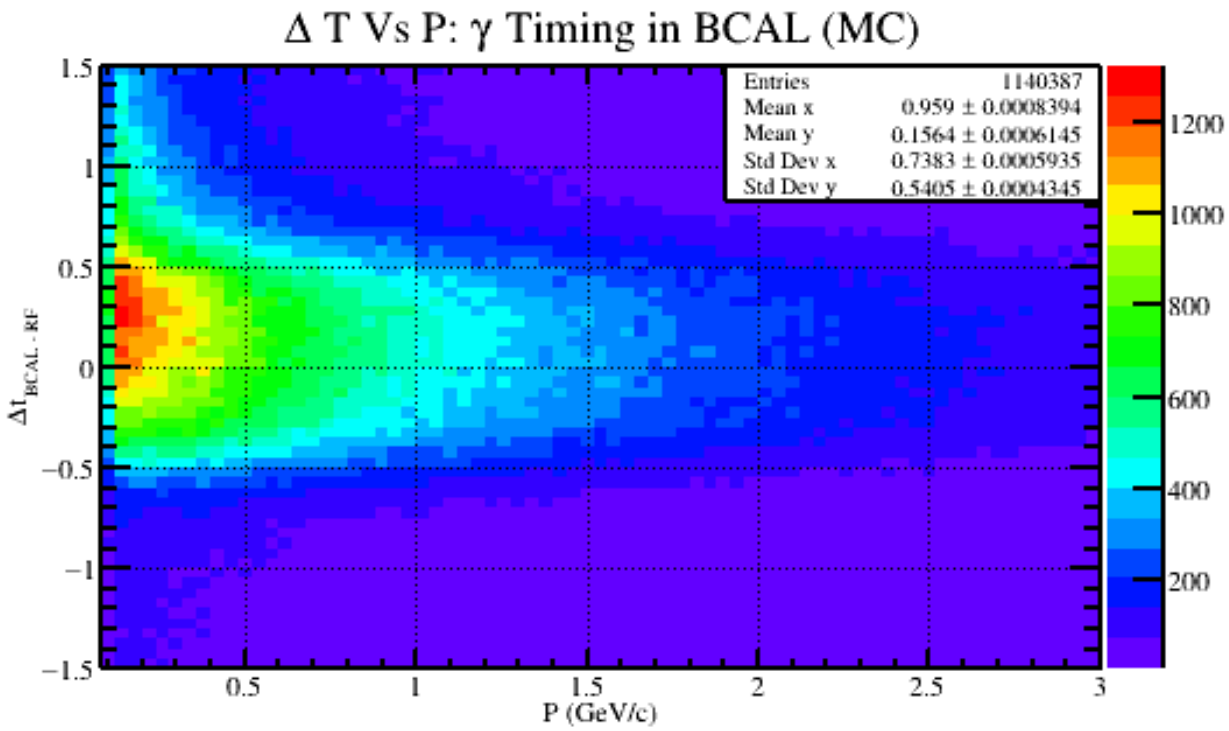

Figure 4.28: A timing plot for generated γ after reconstruction. The horizontal axis is the reconstructed momentum of the γ and the vertical axis is the timing difference between the BCAL and RF.

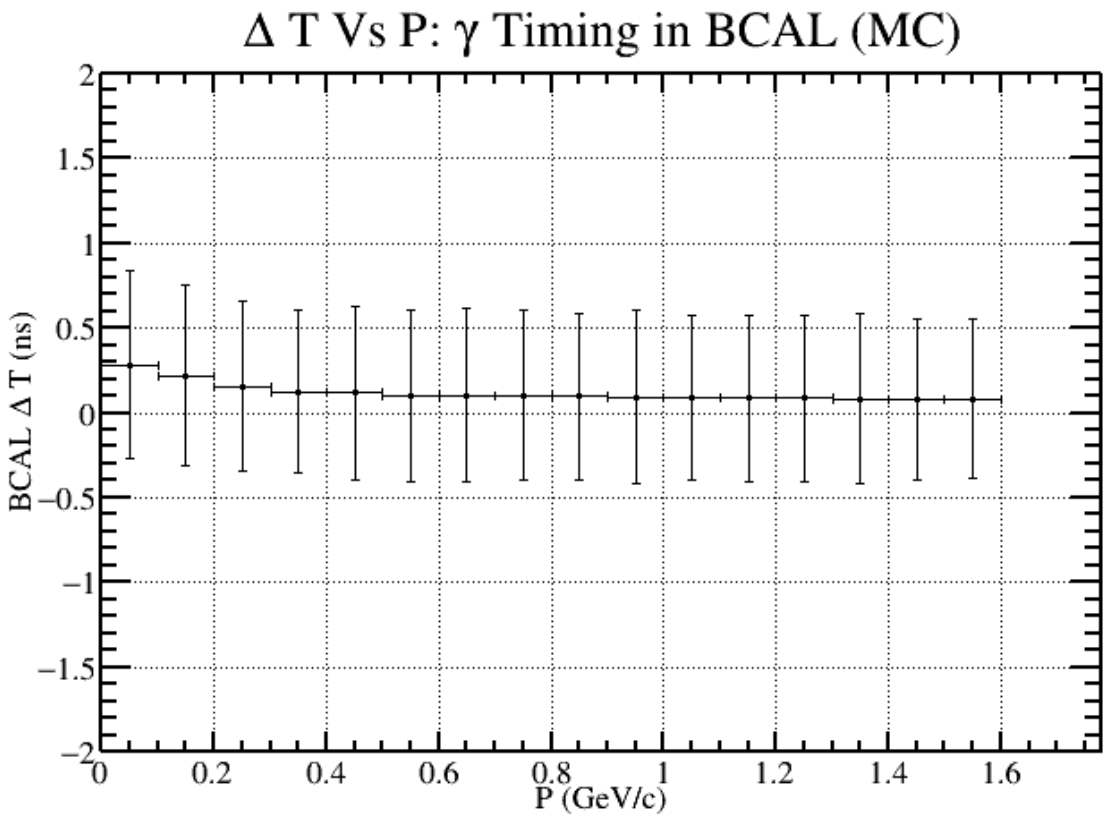

Figure 4.29: The image above is the result of the timing study performed on Figure [4.28]. Using that figure, a number of projection histograms were fit using different momentum ranges. The horizontal position of each point is in the middle of the projection range, and the vertical position of each point was assigned based on the mean value of the Gaussian fit. The horizontal error bars are the size of the projection range, which is always 0.1 GeV/c. The vertical error bars are determined by the width of the Gaussian fit. The average of the widths of the photon peaks is $\sim 0.5ns$ which is the value used to determine the timing cut in Table [4.1].

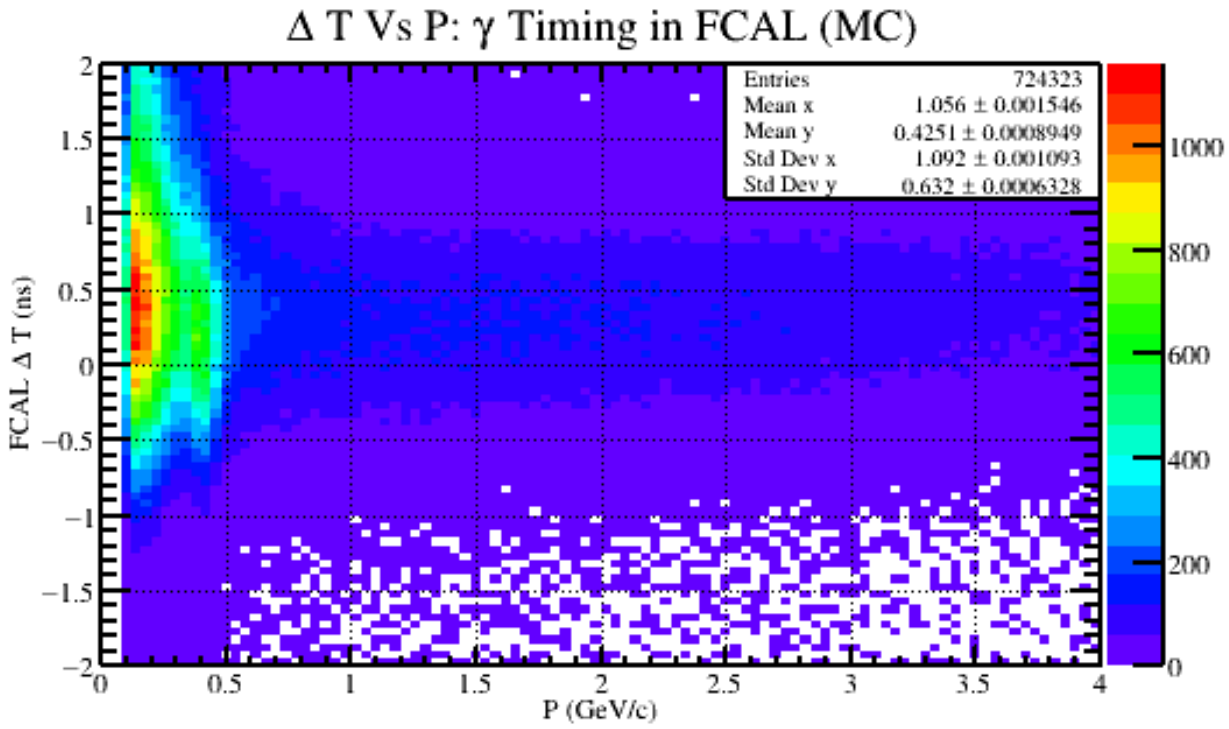

Figure 4.30: A timing plot for generated γ after reconstruction. The horizontal axis is the reconstructed momentum of the γ and the vertical axis is the timing difference between the FCAL and RF.

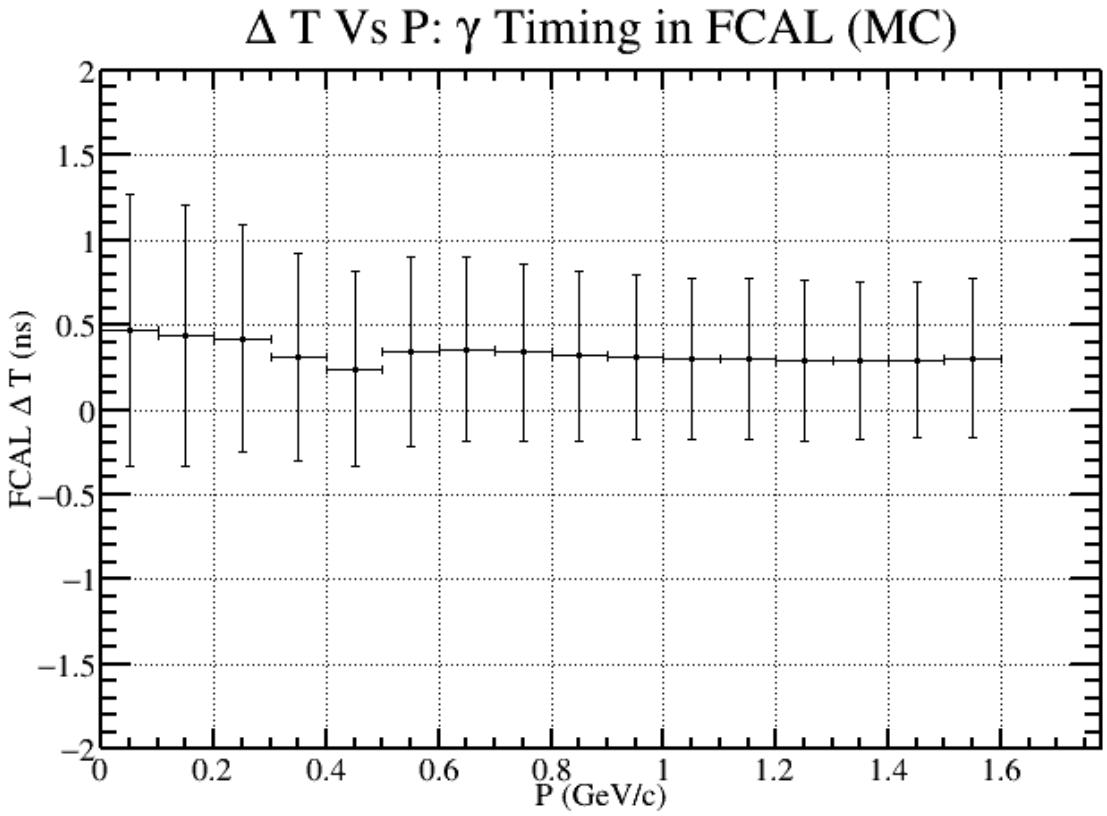

Figure 4.31: The image above is the result of the timing study performed on Figure [4.30]. Using that figure, a number of projection histograms were fit using different momentum ranges. The horizontal position of each point is in the middle of the projection range, and the vertical position of each point was assigned based on the mean value of the Gaussian fit. The horizontal error bars are the size of the projection range, which is always 0.1 GeV/c. The vertical error bars are determined by the width of the Gaussian fit. The average of the widths of the photon peaks is $\sim 0.55ns$ which is the value used to determine the timing cut in Table [4.1].

4.2 Additional Cuts for $\gamma p \to pK^+K^-\gamma\gamma$

Kaon Timing Selection Cut. After the particle identification cuts had been made on the data, it was found that there was still a large amount of background in the K^+K^- invariant mass plot. This background was in all likelihood due to misidentified pions that were mistaken for kaons. This can happen because of the timing and momentum resolutions inherent in any particle physics experiment. Furthermore, as can be seen in many of the timing plots provided, pions and kaon

are in fact indistinguishable at high momentum. An example of what the K^+K^- invariant mass histogram looks like after all particle identification cuts can be seen in Figure 4.32.

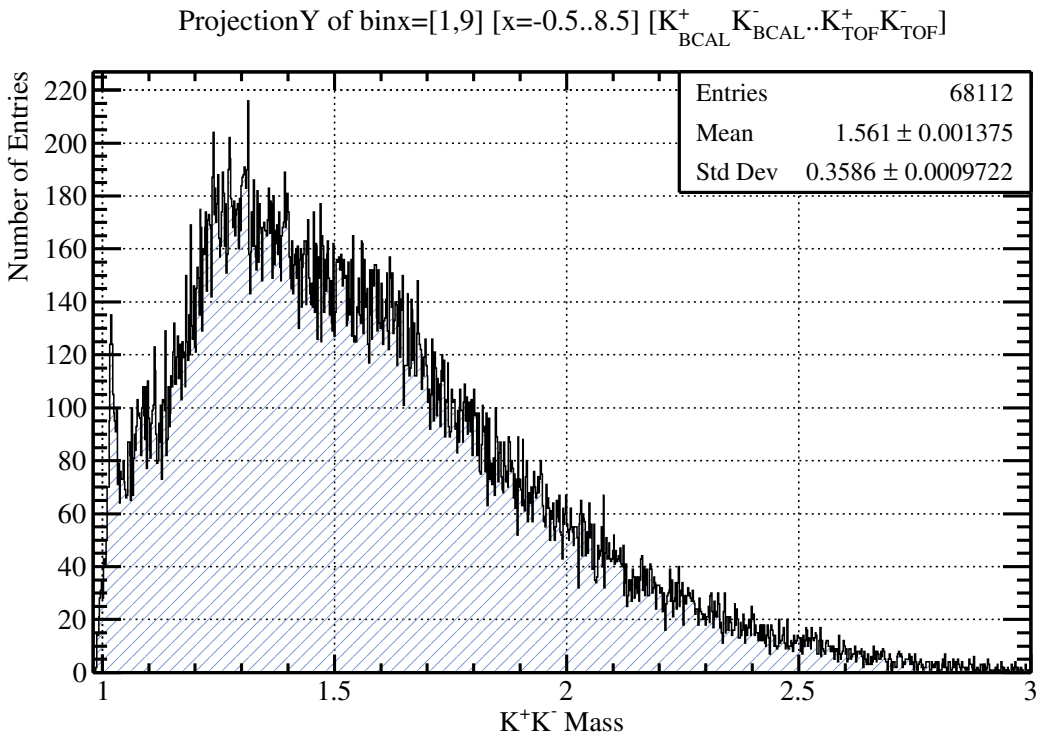

Figure 4.32: A histogram showing the K^+K^- invariant mass after particle identification cuts. The figure clearly shows a large amount of background at masses higher than the ϕ. This is due to the misidentification of pions for kaons.

Due to this background, a study was performed over 5 percent of the data in order to understand both where it may be coming from. The answer to this question was found by splitting up the K^+K^- invariant mass into different sub detectors which are responsible for the timing of the kaons. At GlueX, the three sub detectors which are responsible for providing timing and particle identification for charged particles are the Barrel Calorimeter, the Forward Calorimeter, and the Time of Flight. Since both the K^+ and the K^- can interact with any three of these sub detectors, there are nine total possible timing combinations that need to be considered. In order to properly understand these combinations, a two dimensional color histogram was provided to show how the K^+K^- invariant mass changes as a function of sub detector timing for the kaons (Figure 4.33).

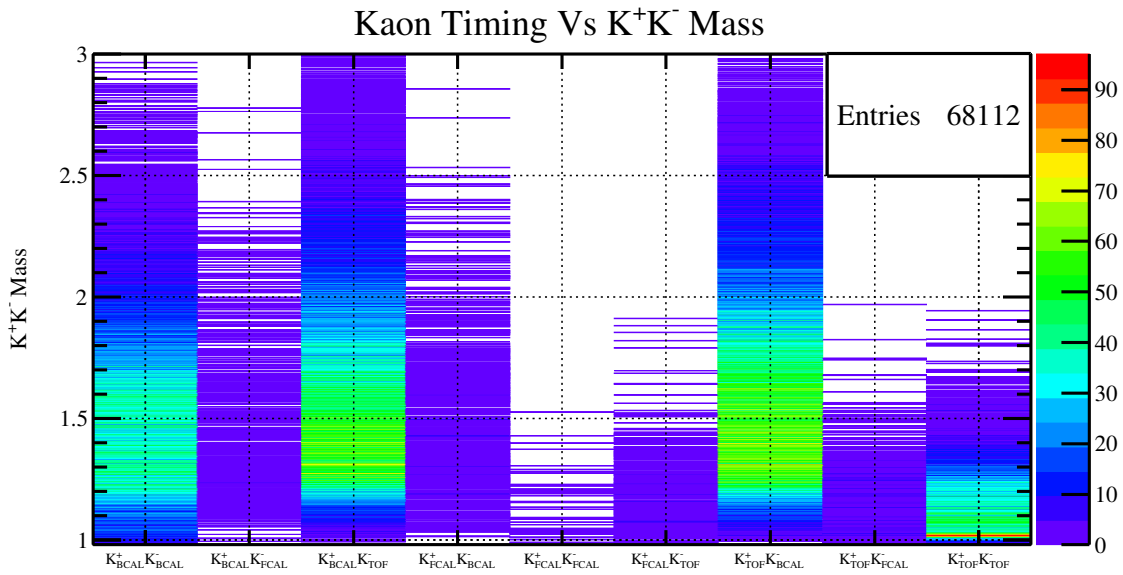

Figure 4.33: A two dimensional color histogram of the K^+K^- invariant mass versus the timing detectors for the kaons.

There are three important observations that can be made from Figure 4.33. One observation is that there is an overwhelming amount of background which comes from the Barrel Calorimeter timing for both K^+ and K^-. The second observation is that the Forwards Calorimeter has little to no statistics what so ever. This is due to the fact that the GlueX reconstruction algorithm prefers timing from sub detectors that have the best timing resolution. Since the Time of Flight and the Forwards Calorimeter are in the same geometric direction, this means that they tend to share a lot of the same charged tracks. Since the timing resolution of the Time of Flight detector is better than the Forward Calorimeter, the majority of forward going charged tracks have timing from the Time of Flight. The last observation of Figure 4.33 is that merely all of the events which appear to have a ϕ meson reconstructed in them only exist in the last bin which is the TOF/TOF timing bin. More specifically, it appears that most of the relevant $\phi\eta$ events will only have kaon timing that came from the Time of Flight detector. Therefore, all other timing sub detectors for the kaons can be thrown out. To further emphasize this point, projections of all nine bins contained within Figure 4.33 have been provided (Figures 4.34,4.35,4.36). These figures clearly show K^+K^- invariant mass spectra which contain all background and no sign of a ϕ meson; with the exception of the TOF/TOF projection.

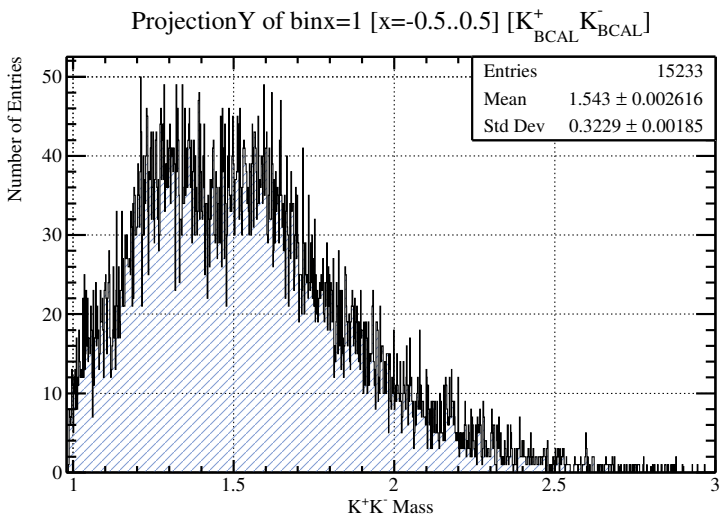

(a) Projection of $K^+_{BCAL}K^-_{BCAL}$ bin from Figure 4.33.

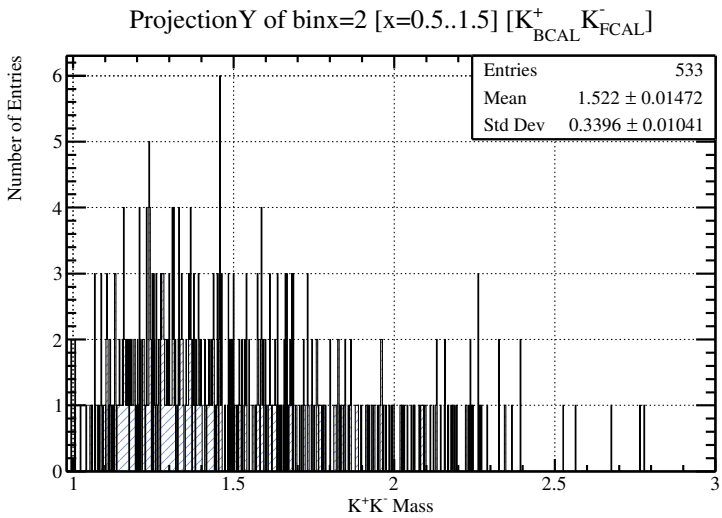

(b) Projection of $K^+_{BCAL}K^-_{FCAL}$ bin from Figure 4.33.

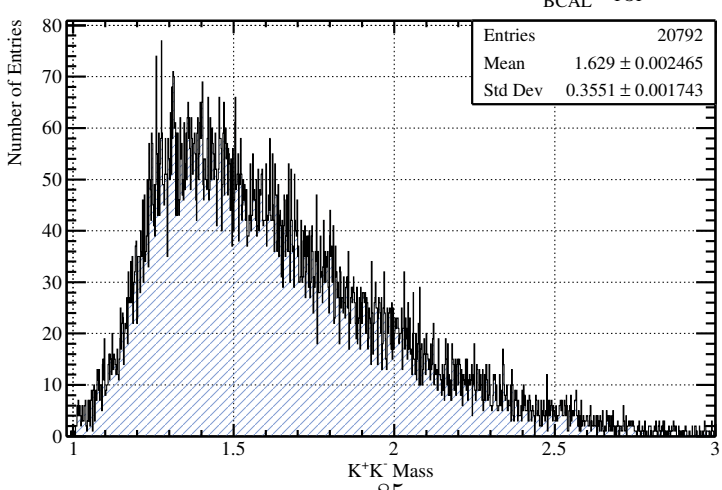

(c) Projection of $K^+_{BCAL}K^-_{TOF}$ bin from Figure 4.33.

Figure 4.34: Projections of $K^+_{BCAL}K^-_X$ bins from Figure 4.33.

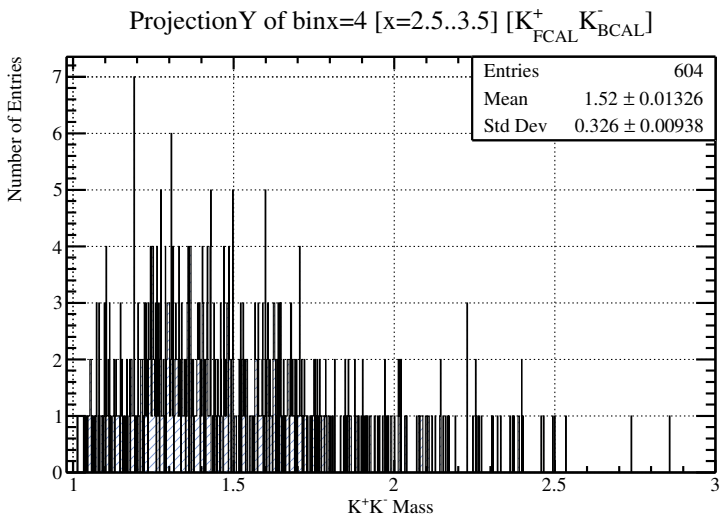

(a) Projection of $K^+_{FCAL}K^-_{BCAL}$ bin from Figure 4.33.

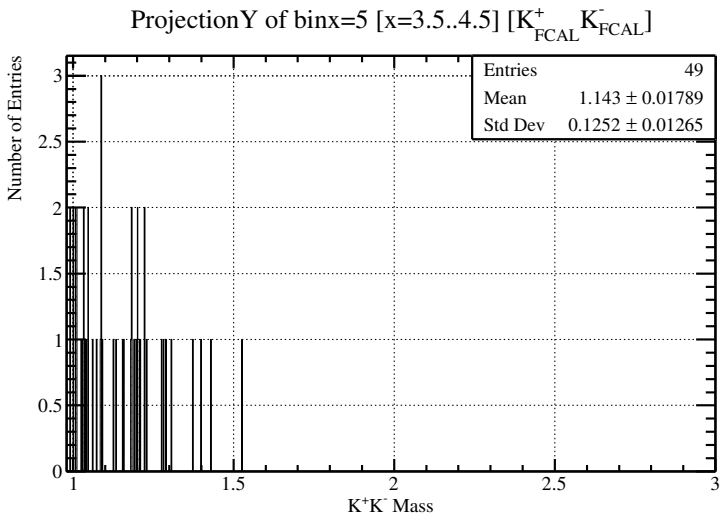

(b) Projection of $K^+_{FCAL}K^-_{FCAL}$ bin from Figure 4.33.

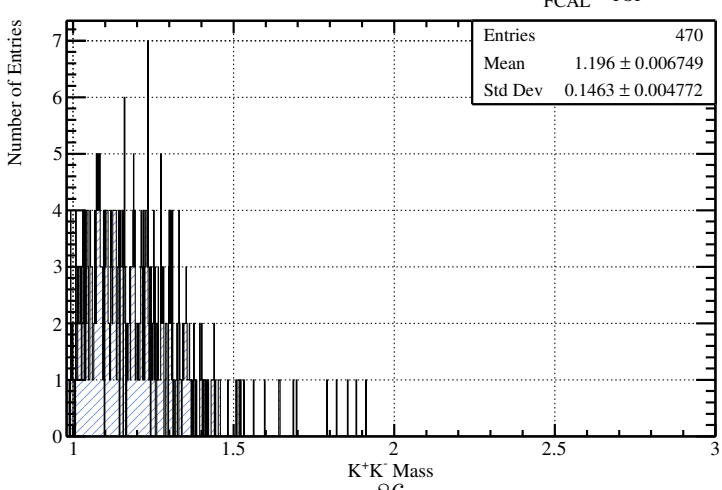

(c) Projection of $K^+_{FCAL}K^-_{TOF}$ bin from Figure 4.33.

Figure 4.35: Projections of $K^+_{FCAL}K^-_X$ bins from Figure 4.33.

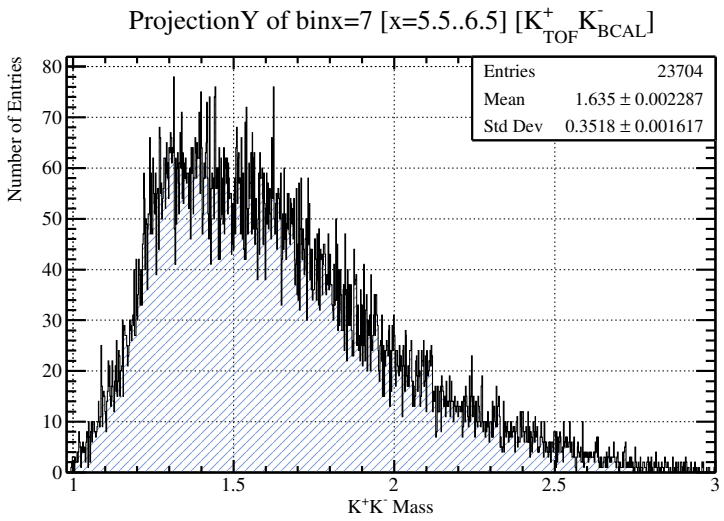

(a) Projection of $K^+_{TOF}K^-_{BCAL}$ bin from Figure 4.33.

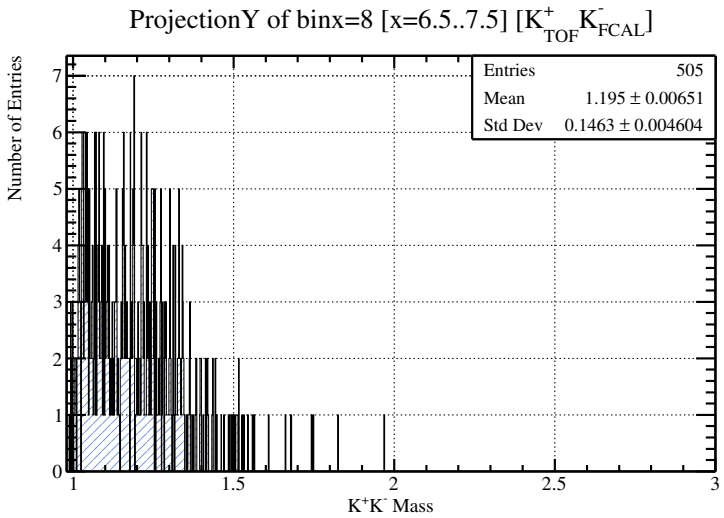

(b) Projection of $K^+_{TOF}K^-_{FCAL}$ bin from Figure 4.33.

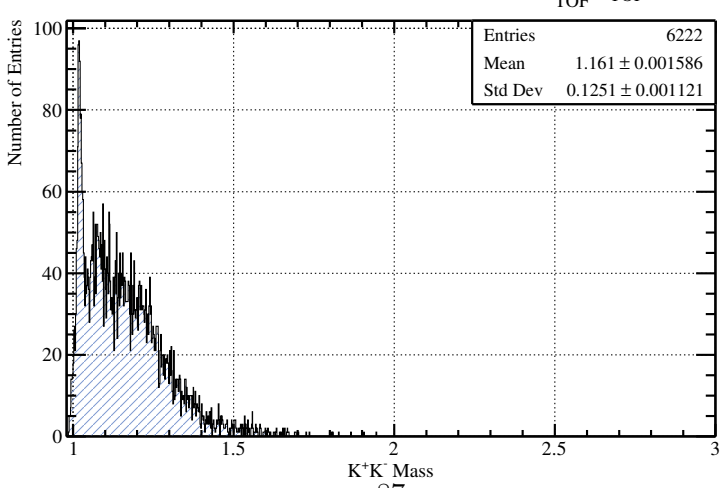

(c) Projection of $K^+_{TOF}K^-_{TOF}$ bin from Figure 4.33.

Figure 4.36: Projections of $K^+_{TOF}K^-_X$ bins from Figure 4.33.

Strangeness Conservation Cut. One key aspect to performing a $\phi\eta$ analysis is to both identify the ϕ and the η mesons while also reducing the amount of background in each of their invariant mass spectra. One of the issues with the K^+K^- invariant mass spectra is the fact that it contains misidentified pions. This background causes a peak in the K^+K^- invariant mass around $1.2GeV/c^2$. This peak is a manifestation of a ρ^0 which can decay to a $\pi^+\pi^-$ final state. An example of this background is illustrated nicely in Figure 4.37.

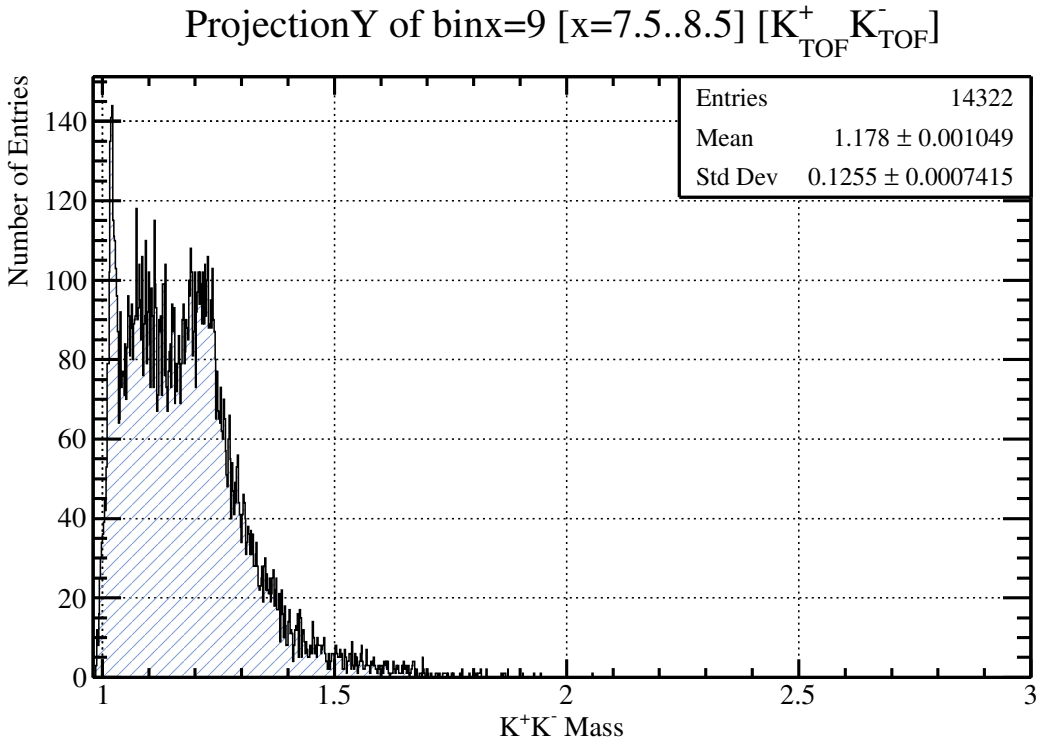

Figure 4.37: An example K^+K^- invariant mass histogram without a strangeness conservation cut. A clear rho peak can be seen around roughly $1.2GeV/c^2$. The histogram which has a reduced pion background can be seen in Figure 4.36c.

One important aspect of QCD and the quark model is the conservation of quark flavor in hadronic decays, or decays which involve the interaction of the strong nuclear force. Conservation of quark flavor states that the initial number flavored quarks minus the initial number of corresponding anti-quarks of the same flavor, must be conserved. An example of this can be any strong interaction which is being studied with the GlueX spectrometer. The experiment has an initial state photon which has no net quark content, plus a proton which has two up quarks and one down quark. Since

the GlueX experiment is designed to study hadronic interactions, the final state must have a net quark flavor of two up quarks and one down quark. Considering the $\gamma p \rightarrow p\phi\eta$ interaction, it is clear that this requirement is met. The initial and final state proton are identical in quark flavor, and the ϕ and η mesons have no net quark flavor to them. Moreover, since the K^+K^- decay of the ϕ meson is being considered, the overall strangeness of this decay needs to be conserved as well. To state this more explicitly, the K^+ meson consists of a $u\bar{s}$ composite state, while the the K^- meson consists of a $s\bar{u}$ composite state. Since each kaon carries either a strange or anti-strange quark, it is only necessary to observe one kaon well. The method of only identifying one kaon well is called strangeness conservation.

Strangeness conservation is used to both preserve good $\phi\eta$ statistics, while also reducing the amount of background under the ϕ peak (Figure 4.37). Since the Time of Flight detector is the only timing detector used for the kaons in this analysis, it is only necessary to consider the particle identification from that sub detector. In order to understand how strangeness conservation is implemented in this analysis, Figure 4.38 is provided. Contained within this figure is the timing versus momentum plot for the K^+, identical to Figure 4.18. Also contained within this diagram is a red line which represents the cut that will be used to separate particles with 'good strangeness' as opposed to particles that 'do not have good strangeness'. This red line is not drawn randomly, or by eye, but is rather derived from simple equations of physics.

The flight time it takes for any relativistic particle to travel a distance δX at a velocity V in the lab frame, can be expressed using Equation 4.1.

$$t = \frac{\delta X}{V} = \frac{\delta X}{\beta c} \tag{4.1}$$

Furthermore, it is well known from Special Relativity that $\beta = E/P$. Using the relativistic equation for invariant mass, we can rewrite Equation 4.1 as Equation 4.2.

$$t = \frac{\delta X}{c}\frac{\sqrt{m_i^2 + P^2}}{P} \tag{4.2}$$

Since Equation 4.2 is true for any particle, we can then use it to describe the timing difference between pions and kaons in the lab frame, as measured by the Time of Flight. This final equation will take the form of Equation 4.3.

$$\delta t = \frac{\delta X}{c} \frac{\sqrt{m_\pi^2 + P^2} - \sqrt{m_K^2 + P^2}}{P} \tag{4.3}$$

The parameters δX, c, m_π, and m_K are known for Equation 4.3 since one is the speed of light, two are well known invariant masses of sub atomic particles, and the other is the distance from the center of the target chamber to the wall of the time of flight. Although charged particles will bend while traveling inside a static magnetic field, this effect is minimal due to the high forward momentum of the kaons in this reaction. Therefore, the only two variables left over are δt and P which serve as the vertical and horizontal axis variables, respectively.

One last modification of Equation 4.3 is needed in order to take the form seen in Figure 4.38. If the equation is left the way that it is, the red line would simply bisect the pion curve, and would therefore not work well as a background cut. Therefore, Equation 4.3 is shifted up by $0.2ns$. This parameter was chosen based on the timing study that was performed on the Monte Carlo and is therefore a 2σ timing shift. It should be noted that since the K^+ and K^- mesons are anti-particles, as well as the π^+ and π^-, the same equation can be used to separate background for both kaons.

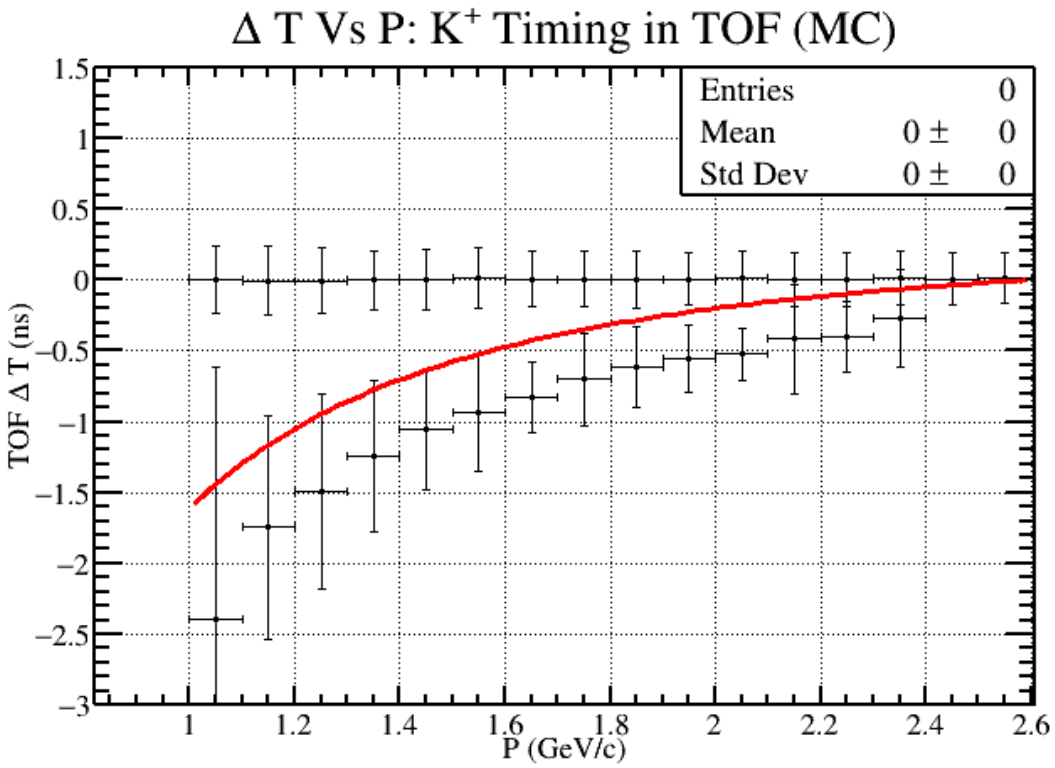

Figure 4.38: A histogram which provides the strangeness conservation cut used for kaons that are detected by the Time of Flight detector. This is identical to Figure 4.18, except that it includes a red line which represents Equation 4.3, with a timing shift of $0.2ns$.

Given Equation 4.3 and Figure 4.38, strangeness conservation can now be addressed. In order to enforce strangeness conservation, it is imperative to identify one 'good kaon'. Good kaons will have three primarily characteristics to them. One characteristic is that the timing will be centered around $\delta t = 0$, the second is that its timing will only come from the Time of Flight, and third is that it will be to the left or above of the red line given in Figure 4.38. Any particle that is to the right or below the red line is not guaranteed to be a kaon, and is therefore 'unknown'. Strangeness conservation allows us to preserve more statistics because all that is needed to justify the observation of a final state which includes a K^+K^- is one 'good kaon'. Therefore, any combination that the has either a K^+ or a K^- with the characteristics mentioned above will be accepted. The only combinations that will be rejected ones which both kaon candidates fail the characteristics mentioned above. To emphasize the importance and effectiveness of this cut, one should see what the K^+K^- invariant

mass looks like without strangeness conservation (Figure 4.37), and then compare it to the K^+K^- invariant mass with strangeness conservation (Figure 4.36c).

Fiducial Photon Cut and Two Photon Cut. Before performing this Monte Carlo study, it was well known that there was a lot of photon background seen in the data. After studying the data for quite some time, it was found that a two photon cut would destroy most of the background associated with photons and would also result in an observed η resonance in a $\gamma\gamma$ invariant mass plot. At the time, it was unknown why the cut appeared to throw out a lot of photon background while simultaneously appearing to enhance signal. After carefully studying accepted Monte Carlo, background generated Monte Carlo (`bggen`), and data, it was found that much of this background is attributed to secondary photons. A secondary photon should be thought of as a photon that did not originate from any photoproduction reaction, nor from any expected decay of parent states. Therefore, a secondary photon can be thought of as a photon that arose from an interaction within the GlueX spectrometer from a final state particle. An example of a secondary photon that would be present in $\gamma p \to p\phi\eta$ data can be explained by means of high momentum and forward going kaons (Figures [3.3][3.4]). Since it is very likely that most of the kaons in this channel will interact with either the Time of Flight detector or the Forward Calorimeter, it is expected that these particle will deposit a lot of energy in this region of the spectrometer. These high momentum particles will cause a signal in one or both of these detectors and will also cause a 'splash' effect near the signal region. This splash effect can cause some of the blocks in the Forward Calorimeter to absorb the extra energy and therefore become reconstructed photons in the data. The additional reconstructed photons will therefore cause the number of photons reconstructed in an event to be fictitiously higher than what was actually present within the detector. To first order, this perhaps explains why doing a two photon cut on data will both greatly reduce background and enhance a signal. However, many important questions will still remain about this cut. How much signal do we lose by simply performing a two photon cut? Furthermore, is there a better way to cut out the background and preserve as many signal events as possible? This subsection will show that this effect does in fact manifest itself in both Monte Carlo and data; and will perform an analysis on Monte Carlo and data to show the best way of reducing secondary photons.

The first evidence that suggests the existence of secondary photons in $\gamma p \to p\phi\eta; \phi \to K^+K^-; \eta \to \gamma\gamma$ accepted Monte Carlo can be seen by simply plotting the invariant mass of a reconstructed $\gamma\gamma$

pair (Figure [4.39]). The data which went into this plot was created by throwing $\gamma p \to p\phi\eta; \phi \to K^+K^-; \eta \to \gamma\gamma$ into the GlueX detector and then simulating its behavior with `hdgeant` and `mcsmear`. The invariant mass spectrum in Figure [4.39] shows a clear peak from the generated η meson on top of a background that spans to low mass. If this sample initially only threw two photons exactly equal to the η meson invariant mass, then why are there so many low mass photon combinations that appear to be in the shape of background? To answer this question, we can separate our reconstructed Monte Carlo particles into two categories: particles that were generated and particles that were not generated. In doing so, we can see where this background comes from and also how to possibly reduce it.

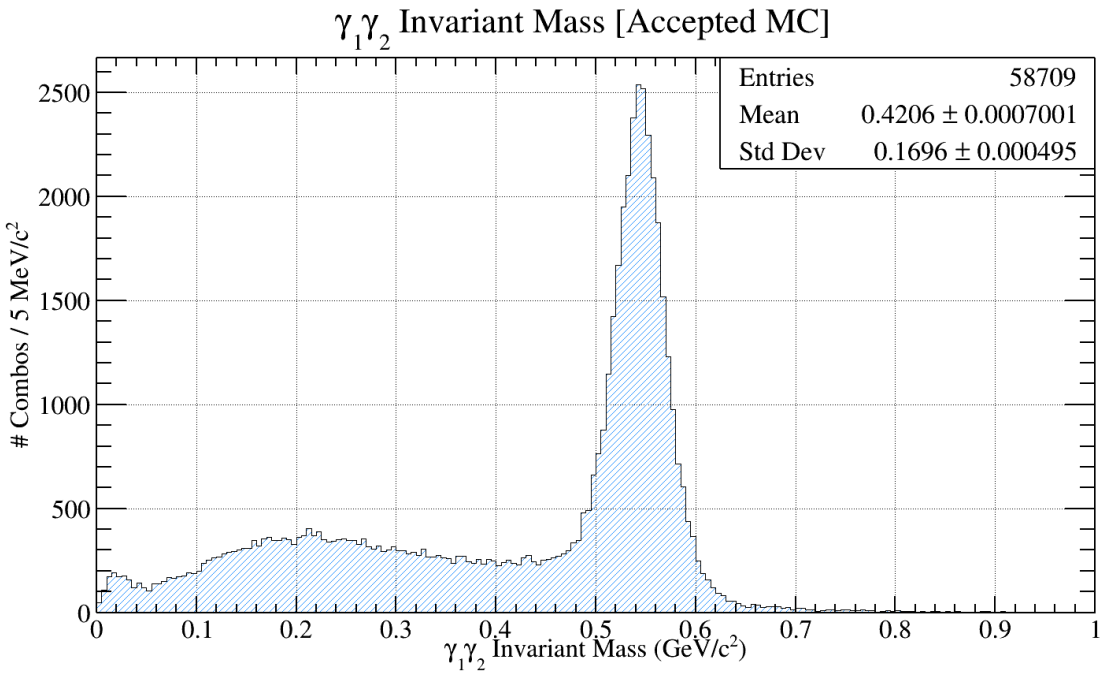

Figure 4.39: Invariant mass of the reconstructed $\gamma_1\gamma_2$ pair from accepted Monte Carlo. This Monte Carlo data originally came from a $\gamma p \to p\phi\eta; \phi \to K^+K^-; \eta \to \gamma\gamma$ generated topology. An interesting feature of this invariant mass spectra is that it shows a clear η peak, but also contains a background as well. The source of this background is thoroughly studied in subsection 4.2.

We will first describe the background seen in Figure [4.39] by displaying P Vs θ and ϕ Vs θ plots for the thrown photons and the secondary photons in Figure [4.40]. The most important feature to take away from these plots is the tendency for secondary photons to be at a shallow angle relative to the beam direction (below 12 while also having a low three momentum magnitude (below 500

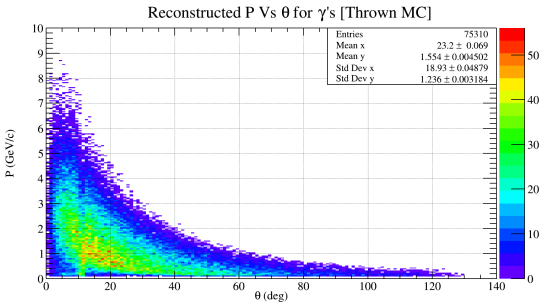

(a) P Vs θ distribution for thrown Monte Carlo photons.

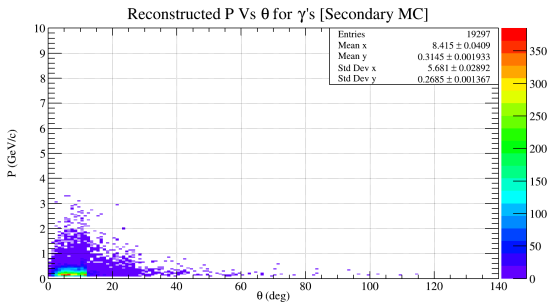

(b) P Vs θ distribution for secondary Monte Carlo photons.

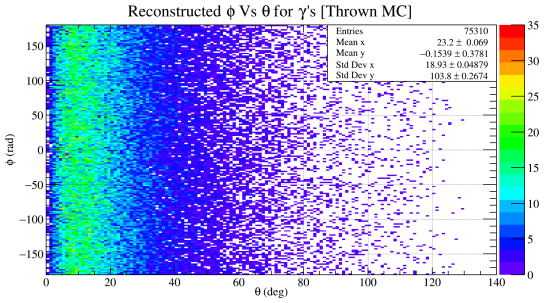

(c) ϕ Vs θ distribution for thrown Monte Carlo photons.

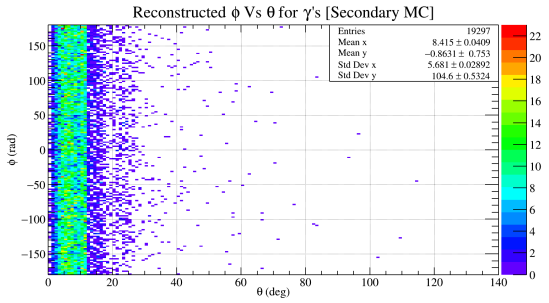

(d) ϕ Vs θ distribution for secondary Monte Carlo photons.

Figure 4.40: P Vs θ and ϕ Vs θ distributions for thrown (left column) and secondary (right column) photons inside accepted Monte Carlo data.

MeV/c). Simply knowing the distribution of these photons gives us some insight into where they came from. Since neutral photons can only be detected by either the Forward Calorimeter or the Barrel Calorimeter and most of these photons appear in the forward direction, it is clear that FCAL showers are causing these photons to appear.

The reconstructed invariant mass for a given $\gamma\gamma$ combination within an event as a function of the number of photons reconstructed within an event can also be shown. By using our Monte Carlo samples, we can also separate these plots into thrown and secondary photons, identical to what we did in Figure [4.40]. The reconstructed invariant mass of two photons versus the number of reconstructed photons in an event is given in Figure [4.41]. There are two important observations that should be taken away from the two sub figures. In Figure 4.41a a clear η resonance can be seen which spans a large number of reconstructed photons per event. What this sub figure tells us

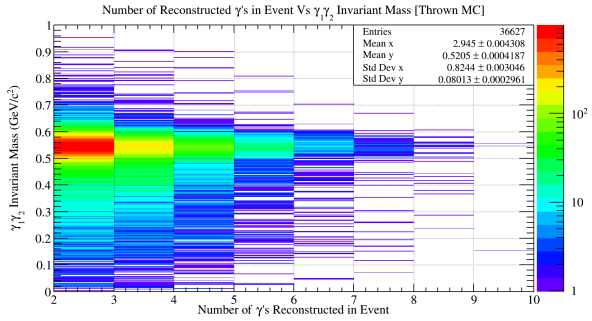

(a) Number of photons reconstructed in an event versus $\gamma_1\gamma_2$ Invariant Mass for thrown photons.

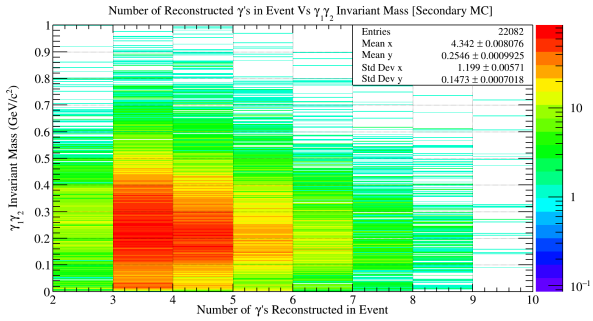

(b) Number of photons reconstructed in an event versus $\gamma_1\gamma_2$ Invariant Mass for secondary photons.

Figure 4.41: Comparing how the invariant mass for a given $\gamma\gamma$ pair changes depending on the number of reconstructed photons in an event and whether or not the photons were thrown or secondary photons.

right away is that performing a two photon cut on the data is not good for signal events. In fact, after fitting a Gaussian function to the η peaks between 3 and 10 reconstructed photons, it was found that ∼8,000 combinations would be lost out of a total of ∼30,000; resulting in a 26 percent loss of events. The second important feature seen in Figure 4.41b is the fact that most of the secondary photons exist in events which reconstruct more than two photons per event. Therefore, it is imperative to cut secondary photons while also preserving the event photons that exist in events which yield a large number of reconstructed photons.

There are a number of ways to cut the secondary photons seen in accepted Monte Carlo. The first and most obvious way would be to cut photons that are both below 12θ and lower than 500 MeV/c in three momentum magnitude. However, since this analysis will eventually include a cut on Kinematic Fit confidence level, the effect of this cut on secondary photons will be studied first. This portion of the study will now include three sets of data: accepted Monte Carlo, background generated Monte Carlo `bggen`, and data. The fist plot that will be shown is the Kinematic Fit confidence level versus the reconstructed $\gamma_1\gamma_2$ invariant mass for all three data sets (Figure [4.42]). In each plot one can easily see an η peak at higher confidence level along side background which is typically at much lower confidence level. Using the accepted Monte Carlo from Figure [4.42a] it was determined that a preliminary Kinematic Fit confidence level cut would be placed at the value $1x10^{-6}$.

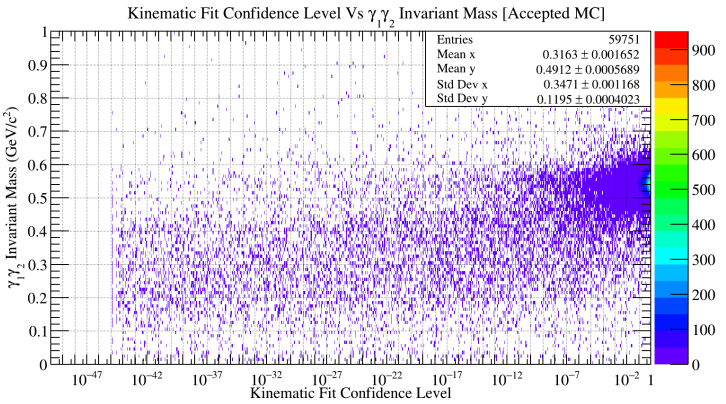

(a) Kinematic Fit confidence level (scaled logarithmically) versus $\gamma_1\gamma_2$ Invariant Mass for accepted Monte Carlo.

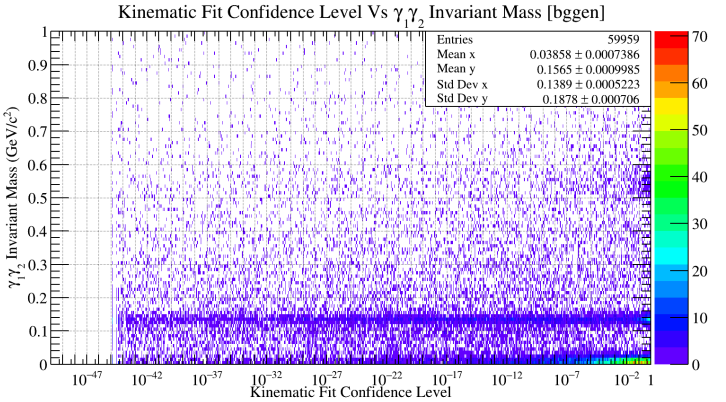

(b) Kinematic Fit confidence level (scaled logarithmically) versus $\gamma_1\gamma_2$ Invariant Mass for background generated Monte Carlo.

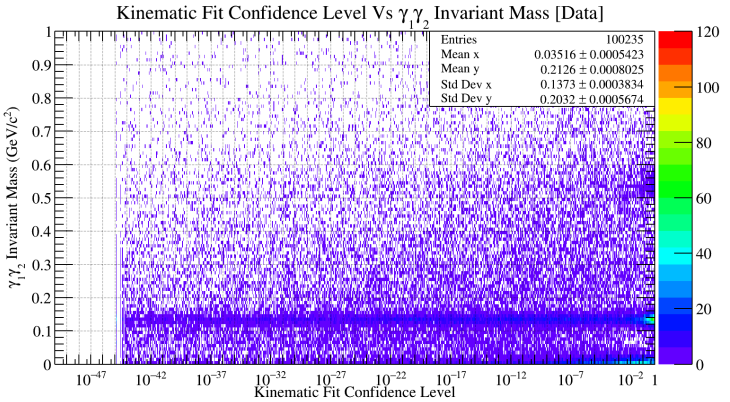

(c) Kinematic Fit confidence level (scaled logarithmically) versus $\gamma_1\gamma_2$ Invariant Mass for data.

Figure 4.42: Kinematic Fit confidence level (scaled logarithmically) versus $\gamma_1\gamma_2$ Invariant Mass for accepted Monte Carlo, background generated Monte Carlo, and data.

After performing a confidence level cut of $1x10^{-6}$ it is clear that much of the secondary photons are destroyed. One way of seeing the effect of this cut is by looking at the number of reconstructed photons in an event versus the $\gamma_1\gamma_2$ invariant mass distributions (Figure [4.43]). Comparing Figure [4.43a] with Figure [4.41a], one can easily see that the Kinematic Fit confidence level cut moved many of the η's from high photon reconstruction number per event to low photon reconstruction number per event. This migration of events is due to the fact that the Kinematic Fitter is cutting many secondary photons out of events and therefore decreasing the number of photons reconstructed per event. Furthermore, comparing Figure [4.43b] with Figure [4.41b], one can simply look at the density of events within the two dimensional histogram to realize that an overwhelming amount of secondaries has been cut, roughly 94 percent.

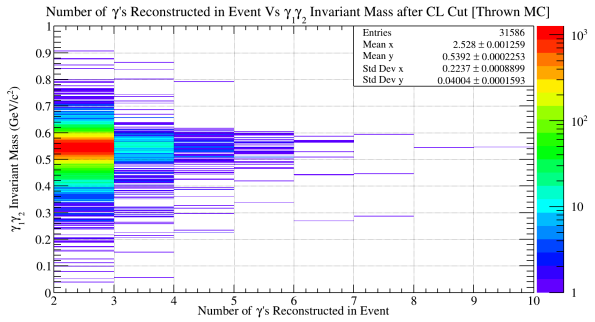

(a) Number of photons reconstructed in an event versus $\gamma_1\gamma_2$ Invariant Mass for thrown photons after a Kinematic Fit confidence level cut of $1x10^{-6}$.

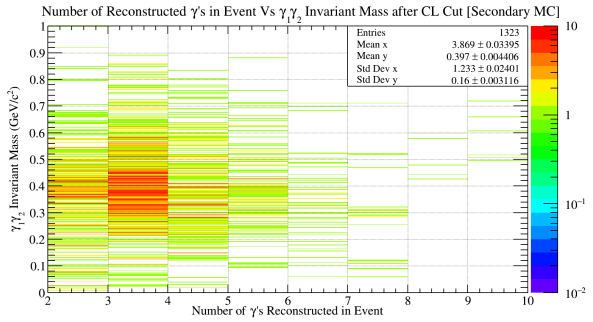

(b) Number of photons reconstructed in an event versus $\gamma_1\gamma_2$ Invariant Mass for secondary photons after a Kinematic Fit confidence level cut of $1x10^{-6}$.

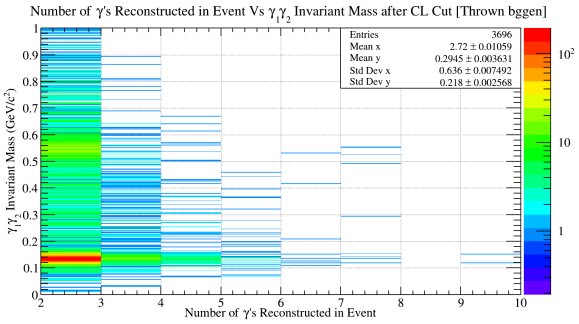

(c) Number of photons reconstructed in an event versus $\gamma_1\gamma_2$ Invariant Mass for thrown photons from `bggen` data after a Kinematic Fit confidence level cut of $1x10^{-6}$.

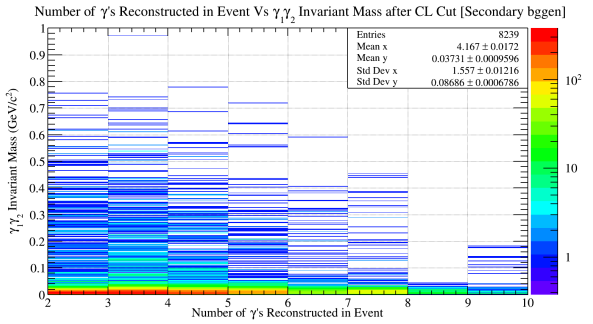

(d) Number of photons reconstructed in an event versus $\gamma_1\gamma_2$ Invariant Mass for secondary photons from `bggen` data after a Kinematic Fit confidence level cut of $1x10^{-6}$.

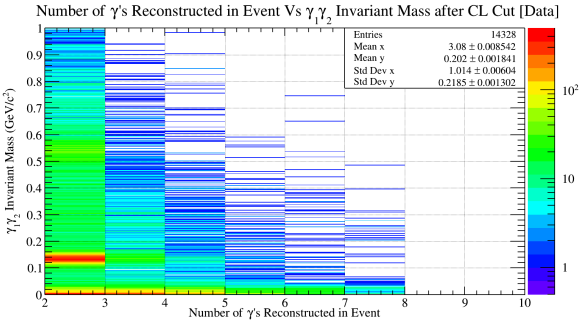

(e) Number of photons reconstructed in an event versus $\gamma_1\gamma_2$ Invariant Mass for data after a Kinematic Fit confidence level cut of $1x10^{-6}$.

Figure 4.43: Number of photons reconstructed in an event versus $\gamma_1\gamma_2$ Invariant Mass for accepted Monte Carlo, `bggen`, and data after a Kinematic Fit confidence level cut of $1x10^{-6}$.

Seeing that there is still a non negligible amount of secondary photons left in accepted Monte Carlo and `bggen`, the next cut that will be applied to all of the data is a P Vs θ cut, where $P < 500MeV/c$ and $\theta < 12$ After enforcing these cuts on all photons, the distribution of number of photons reconstructed in an event versus $\gamma_1\gamma_2$ Invariant Mass is shown once again in Figure [4.44]. It is easy to see that most, if not all of the η signal has migrated to the two photon bin and simultaneously much of the secondary background has been reduced in all data sets. Due to this, a two photon cut is now necessary to do in order to reduce some of the left over background at higher number of reconstructed photons per event.

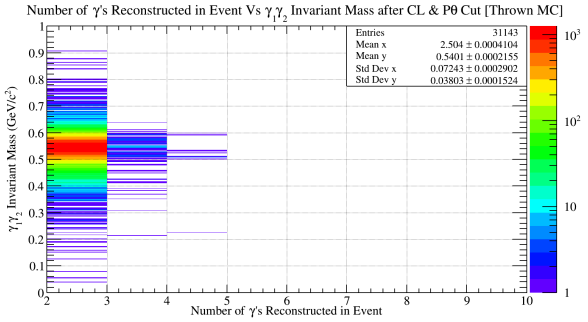

(a) Number of photons reconstructed in an event versus $\gamma_1\gamma_2$ Invariant Mass for thrown photons after a confidence level cut of $1x10^{-6}$ and a P Vs θ cut.

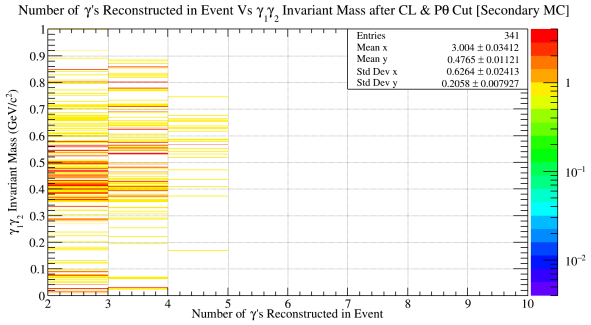

(b) Number of photons reconstructed in an event versus $\gamma_1\gamma_2$ Invariant Mass for secondary photons after a confidence level cut of $1x10^{-6}$ and a P Vs θ cut.

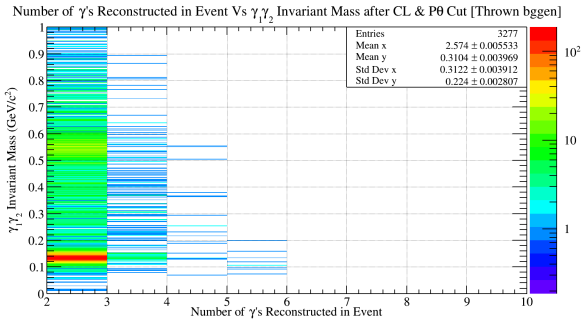

(c) Number of photons reconstructed in an event versus $\gamma_1\gamma_2$ Invariant Mass for thrown photons from `bggen` data after a confidence level cut of $1x10^{-6}$ and a P Vs θ cut.

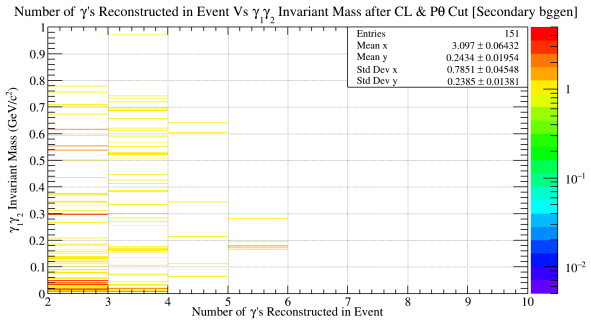

(d) Number of photons reconstructed in an event versus $\gamma_1\gamma_2$ Invariant Mass for secondary photons from `bggen` data after a confidence level cut of $1x10^{-6}$ and a P Vs θ cut.

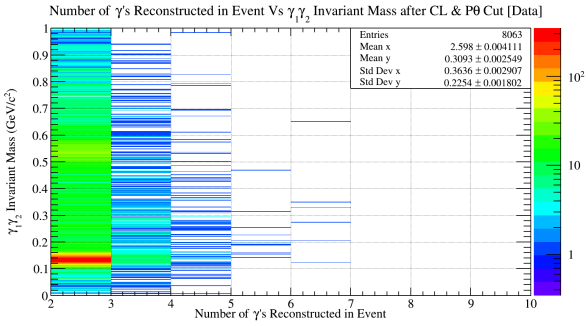

(e) Number of photons reconstructed in an event versus $\gamma_1\gamma_2$ Invariant Mass for data after a confidence level cut of $1x10^{-6}$ and a P Vs θ cut.

Figure 4.44: Number of photons reconstructed in an event versus $\gamma_1\gamma_2$ Invariant Mass for accepted Monte Carlo, `bggen`, and data after a confidence level cut of $1x10^{-6}$ and a P Vs θ cut.

In this section it was shown that it is necessary to perform a P Vs θ cut of $P < 500MeV/c$ and $\theta < 12$ nd a two photon cut. After completing this sequence of cuts, it was found that 94 percent of background data was cut, while preserving 93 percent of signal data.

4.2.1 Exclusivity

The last cuts that need to take place in order to observe $\gamma p \to p\phi\eta$ are two; one which reduces the number of photons from the beam, and the other which cuts on the missing mass squared of the system. After all cuts had been made, it was found that there were still residual combinations from events which came directly from the beam photons and not the final state particles. After the proper beam timing cut, the event selection will then loop over available combinations in order to select the best available beam photon. This is done by selecting the beam photon which reconstructs the missing mass squared which is closest to zero. After enforcing this criteria, it is guaranteed that only one combination per event will survive. After this selection of events, an additional cut is placed on the data which enforces exclusivity. This is done by only allowing events with a missing mass squared between $-0.02GeV^2/c^4 \leq MM^2 \leq 0.02GeV^2/c^4$. The enforcement of exclusivity removes any background that did not properly conserve the measured four momentum from the $\gamma p \to pK^+K^-\gamma\gamma$ reaction. To finalize this section Table 4.2 is a summarized list of all cuts performed by this analysis.

4.2.2 Tabular Summary of Particle Identification Cuts

Particle	Detector	ΔT Cut [ns] (2σ)
Proton	BCAL	$\pm$ 0.6
Proton	FCAL	$\pm$ 1.0
Proton	TOF	$\pm$ 0.4
K^+	BCAL	$\pm$ 0.7
K^+	FCAL	$\pm$ 0.8
K^+	TOF	$\pm$ 0.2
K^-	BCAL	$\pm$ 0.7
K^-	FCAL	$\pm$ 0.8
K^-	TOF	$\pm$ 0.2
γ	BCAL	$\pm$ 1.0
γ	FCAL	$\pm$ 1.1

Table 4.1: A table with timing cut values for all final state particles in the reaction $\gamma p \rightarrow pK^+K^-\gamma_1\gamma_2$. The values of the timing cuts change depending on both the particle species and detector system resolution. It should be noted that the final state photons only have the calorimeters as possible timing detectors. This is due to the fact that they do not interact with the TOF detector.

#	Description of Cut	Reference
1	Timing cuts for all final state particles	Table 4.1
2	Vertex cuts for all final state particles	Figures 4.3a, 4.3b
3	Beam timing cut	Figure 4.1
4	Beam energy cut	Figure 4.2
5	Proton dE/dX cut	[Paper]
6	Fiducial cut for final state photons	Subsec: 4.2
7	Kaon timing only from TOF	Figure 4.36c
8	Strangeness Conservation	Figure 4.38
9	Two Photon Cut	Subsec: 4.2
10	γ_{Beam} with MM^2 closest to zero	Subsec:4.2.1

Table 4.2: A list which summarizes all cuts used to identify $\gamma p \rightarrow pK^+K^-\gamma\gamma$.

CHAPTER 5

ANALYSIS

5.1 Investigation of $\phi\eta$ correlation by means of K^+K^- Vs $\gamma_1\gamma_2$ Invariant Mass Plot

The image illustrated in Figure 5.1 is the data in question. On the vertical axis is the K^+K^- invariant mass and on the horizontal axis is the $\gamma_1\gamma_2$ invariant mass. To be absolutely clear, this is a plot of invariant mass versus invariant mass and is therefore not a Dalitz Plot. Some interesting features contained within the image are the clear vertical bands for the π^0 and η resonances which have large decay modes to $\gamma\gamma$ final states. In addition, one can also observe a horizontal band slightly above 1 $\frac{GeV}{c^2}$ which corresponds to the ϕ meson decaying to a K^+K^- final state. This analysis will focus on the region where the ϕ meson and η meson bands cross in order to determine if their intersection region contains some type of correlation.

5.1.1 Cuts on the 2D Invariant Mass Plot

In order to analyze the $\phi\eta$ region of this data, only events which fall within $\pm 10\sigma_\phi$ away from the ϕ peak and $\pm 10\sigma_\eta$ away from the η peak will be considered. This was done by taking different slices of either the $\gamma\gamma$ or K^+K^- data, then projecting the invariant mass distribution onto the opposite axis. For example, there were five different ϕ mass regions studied in this analysis. Each fit corresponds to a different $\gamma\gamma$ mass range. The $\gamma\gamma$ mass ranges are all $4\sigma_\eta$ in width, and span a total mass range of $m_\eta - 10\sigma$ to $m_\eta + 10\sigma$. An illustrated example with labeled cut lines is provided in Figure 5.2. It should be noted that the analysis of the η mass was not studied symmetrically about the ϕ due to the fact that going more than $m_\phi - 6\sigma_\phi$ away from the ϕ peak would result in no events because of the K^+K^- threshold.

5.1.2 Projections and Fits for ϕ and η

Once the data had been cut and projected in the ten different mass regions, the ϕ and η peaks were fit. In the instance of the ϕ meson, the signal plus background events were fit with a Gaussian plus a second degree polynomial. The fit range used in each histogram projection for the ϕ meson

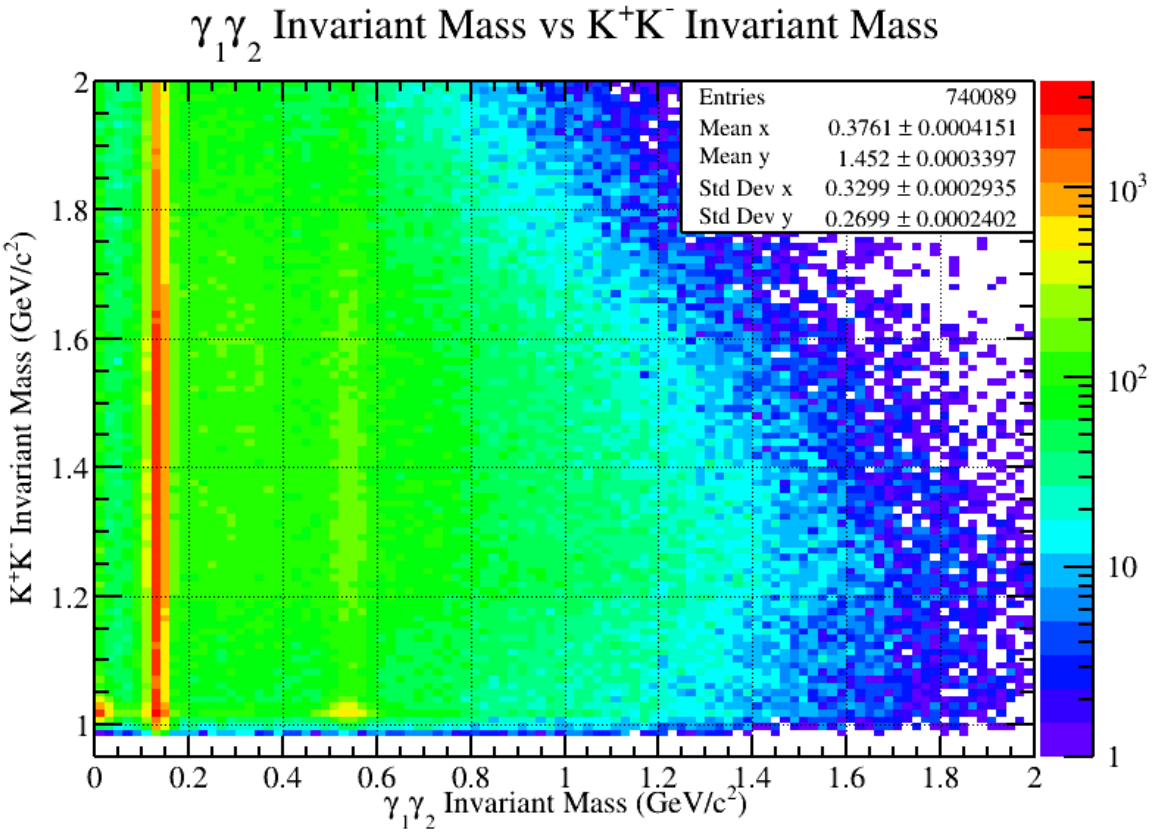

Figure 5.1: A two dimensional invariant mass plot with the K^+K^- invariant mass on the vertical axis, the $\gamma_1\gamma_2$ invariant mass on the horizontal axis, and a logarithmically scaled z axis. Some interesting features contained within the image are the clear vertical bands for the π^0 and η resonances which have large decay modes to $\gamma\gamma$ final states. In addition, one can also observe a horizontal band slightly above 1 $\frac{GeV}{c^2}$ which corresponds to the ϕ meson decaying to a K^+K^- final state.

spans from $m_\phi - 6\sigma_\phi$ to $m_\phi + 30\sigma_\phi$ $\frac{GeV}{c^2}$. The unusually large fit range was necessary in order to properly estimate the background surrounding the ϕ mass. In the instance of the η meson, the signal plus background events were fit with a Gaussian plus a first degree polynomial due to the relatively flat background surrounding the η peak. The fit range used for the η meson spans $m_\eta \pm 6\sigma_\eta$ $\frac{GeV}{c^2}$. The resulting fits are provided in the images below where the blue line represents the fit for all events (signal plus background), the green line represents the Gaussian fit (signal events), and the red line represents the polynomial fit (background events). Each histogram contains a title with brackets at the end. The arguments encapsulated by the brackets is the cut range that was used for that particular projection sample.

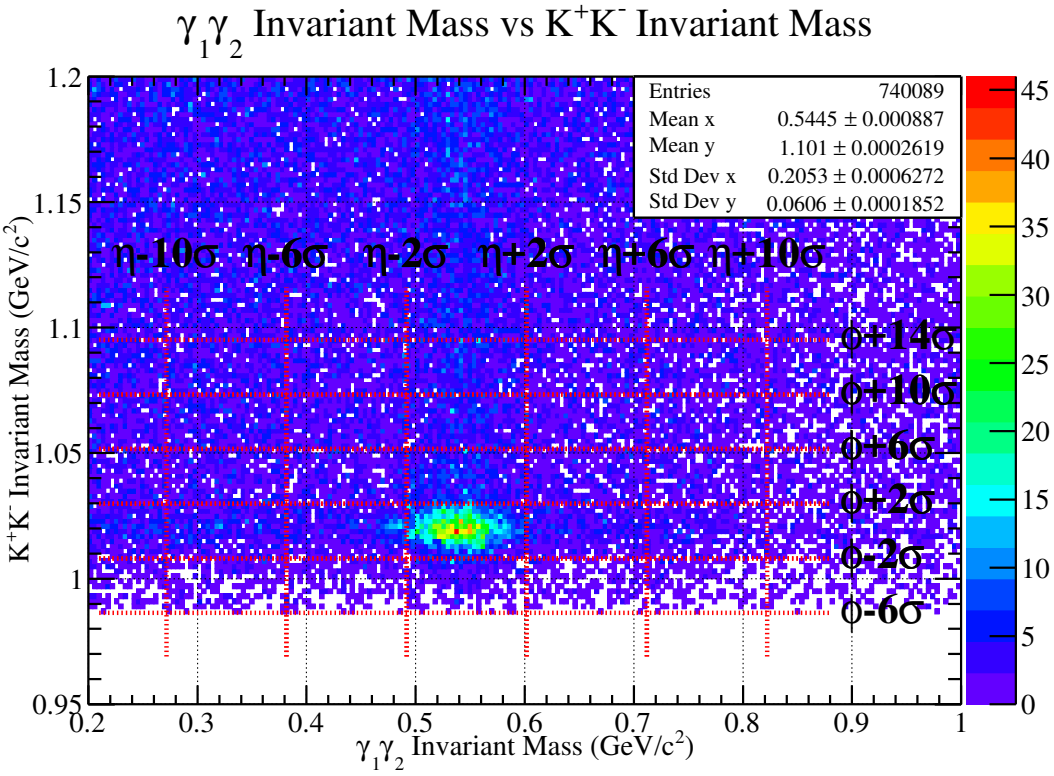

Figure 5.2: An illustrated example of the cuts used for studying the correlation of $\phi\eta$. The figure above is a two dimensional invariant mass plot which clearly shows an η band spanning the vertical direction at $\sim 0.547 GeV/c^2$ and a ϕ band spanning the horizontal direction at $\sim 1.02 GeV/c^2$. The red vertical and horizontal cut lines provide the ranges used to study $\phi\eta$ correlation. Examples of what the projected ranges look like are provided in Figures [5.3][5.4].

5.1.3 Integration Results for ϕ and η

After obtaining accurate fits for all regions, integration of the Gaussian fit functions was performed. Each Gaussian fit was integrated in the range of $m \pm 2\sigma_m$, where m represents either m_ϕ or m_η mass coupled with the addition or subtraction of two standard deviations in each direction. Integration of the Gaussian fits provides an accurate estimate for the number of signal events that exists for that particular sampling of $\gamma\gamma$ Vs K^+K^- phase space. The estimated number of signal events have been added to the 2D mass plot below, with the exception of the $\phi\eta$ intersection region which will be discussed in more detail in the Conclusion section.

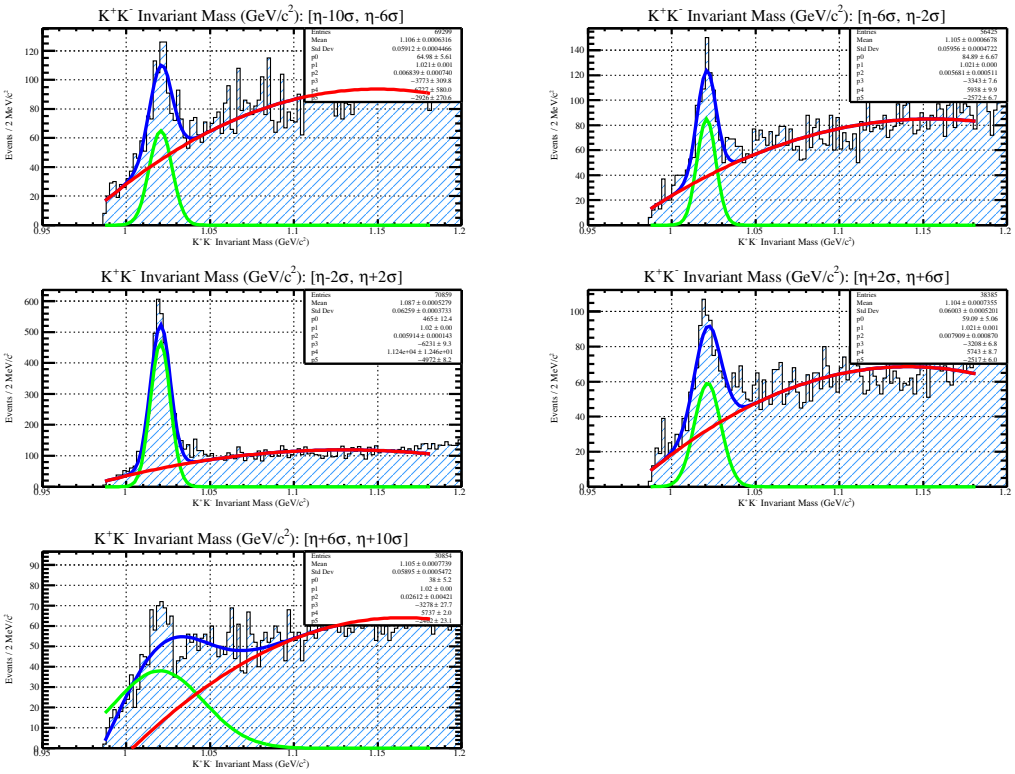

Figure 5.3: A collection of different K^+K^- Invariant Mass projections as a function of $\gamma_1\gamma_2$ Invariant Mass cut range. Each sub figure includes a red line which is a second degree polynomial used to estimate the shape of the background, a green line which is a Gaussian used to estimate the ϕ signal peak, and a blue line which the sum total of the polynomial fit and Gaussian fit. Lastly, each sub figure also includes the $\gamma_1\gamma_2$ Invariant Mass cut range used to produce the projected figure. This information is in the title of the histogram, inside the brackets.

5.1.4 Additional Statistics Study

In addition to the analysis mentioned above, an additional study has been included which simply samples the phase space and records the number of events within that sample. To do this, the same cut ranges as before were used. The only difference is that only the 3x3 grid surrounding the $\phi\eta$ intersection region. Each region is a box cut which is exactly $4\sigma_\phi$ x $4\sigma_\eta$ in area. Each area is given an index to denote the specific region of phase space that is being sampled and an illustration is provided below.

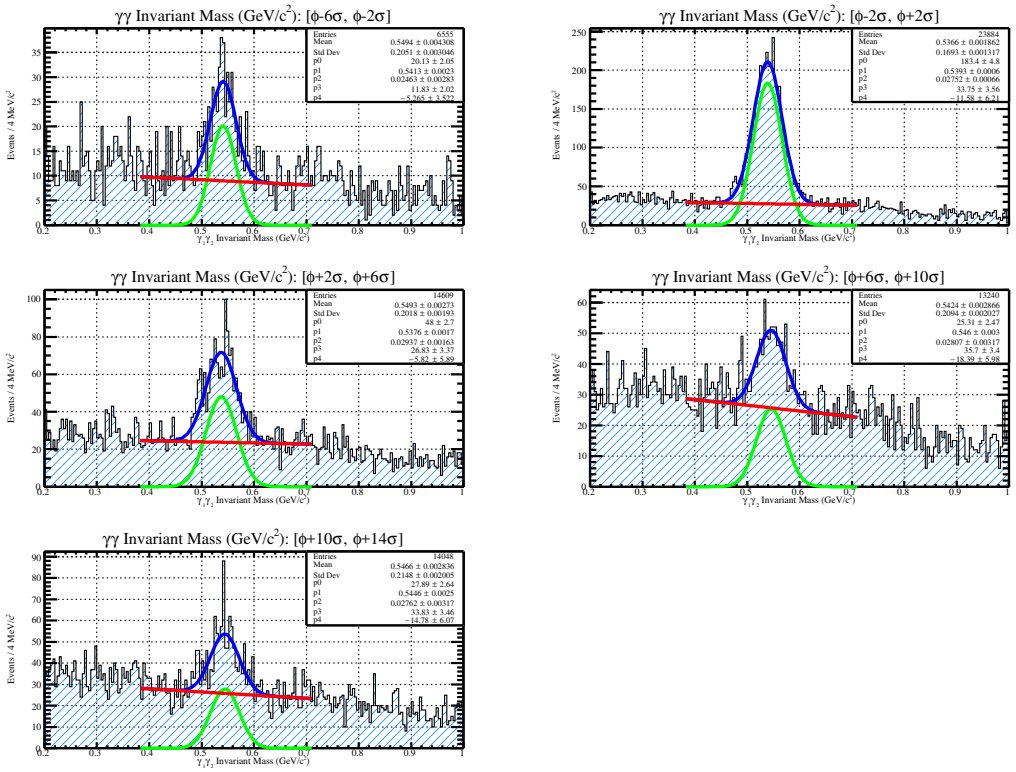

Figure 5.4: A collection of different $\gamma_1\gamma_2$ Invariant Mass projections as a function of K^+K^- Invariant Mass cut range. Each sub figure includes a red line which is a first degree polynomial used to estimate the shape of the background, a green line which is a Gaussian used to estimate the η signal peak, and a blue line which the sum total of the polynomial fit and Gaussian fit. Lastly, each sub figure also includes the K^+K^- Invariant Mass cut range used to produce the projected figure. This information is in the title of the histogram, inside the brackets.

Using the diagram as a reference, it is easy to see that the average number of background events within this phase space can be calculated using the formula $N_{BG} = (A_1 + A_3 + A_7 + A_9)/4$. Additionally, the average number of ϕ and η events plus background can be calculated using $N_{BG} + N_\phi = (A_4 + A_6)/2$ and $N_{BG} + N_\eta = (A_2 + A_8)/2$, respectively. Lastly, quantification of the number of correlated events in region 5 is possible by using $N_{BG} + N_\phi + N_\eta + N_{correlated} = A_5$. A figure with the number of events contained within each region of phase space is given below.

The first step of this simplistic analysis is to determine what the average number of background

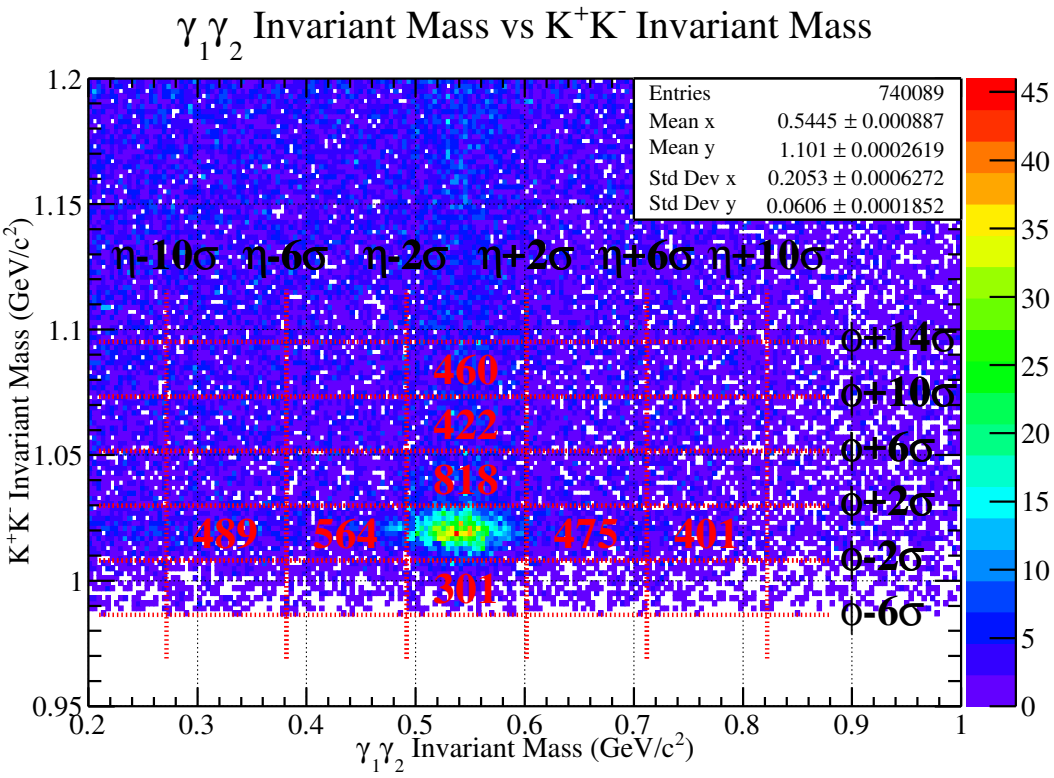

Figure 5.5: The above figure provides the number of events for each projection range studied. These numbers were calculated by means of integrating the Gaussian fit for either the ϕ or η between $\pm 2\sigma$. The vertical column of numbers represents the number of η events for a given K^+K^- Invariant Mass, and the horizontal row of numbers represents the number of ϕ events for a given $\gamma_1\gamma_2$ Invariant Mass. The number of events observed in the intersection region was not included in the figure due to the amount of space available. There numbers can be found in the Conclusion section.

events is, which is calculated to be 453. Knowing this, the number of ϕ and η events can now be determined by using the equations $N_{BG} + N_\phi = (A_4 + A_6)/2$ and $N_{BG} + N_\eta = (A_2 + A_8)/2$, and then subtracting the average number of background events. Upon doing this, it was fount that N_ϕ is 423 and N_η is 433. To complete this analysis, the number of correlated events can now be estimated by using the equation $N_{BG} + N_\phi + N_\eta + N_{correlated} = A_5$, and subtracting N_{BG}, N_ϕ, and N_η. The total number of correlated events is 2446. This calculations shows once again that there is an overflow of events within the $\phi\eta$ intersection region that cannot be explained by the presence

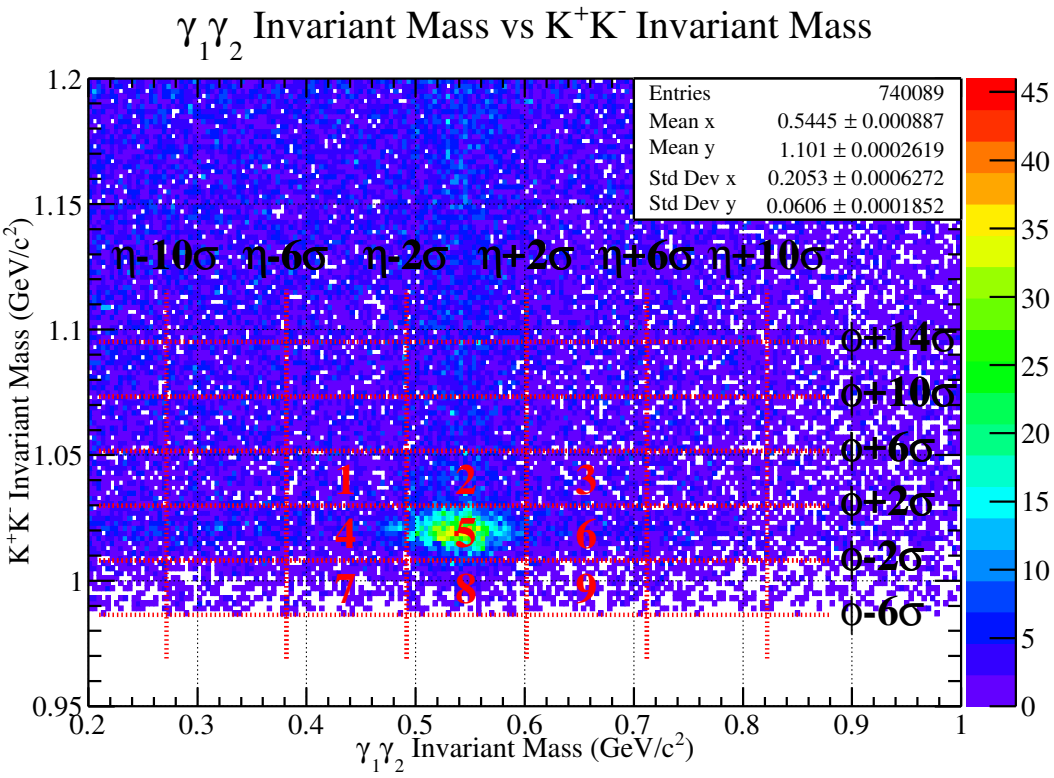

Figure 5.6: An illustration to provide the reader with an idea of how the second statistics study is performed. All of the cut ranges are identical to the first statistics study. The numbers provided in the figure do not represent events, but simply indicate the index associated with a certain area of $\phi\eta$ phase space.

of background or the addition of events from the ϕ and η bands.

5.1.5 Conclusion of K^+K^- Vs $\gamma_1\gamma_2$ Invariant Mass Plot Study

Given that the number of estimated signal events has been calculated for the ϕ and η bands which neighbor the $\phi\eta$ intersection region, the expected number of events will be in the $\phi\eta$ intersection region using averages can be estimated. Taking the numbers from the two dimensional plot above and rounding to the nearest integer, the average number of signal events in the ϕ band is $\overline{\phi_{events}} \sim 482$, and the average number of signal events in the η band is $\overline{\eta_{events}} \sim 500$. Therefore, it is estimated that the number of signal events within the $\phi\eta$ intersection region should be just shy

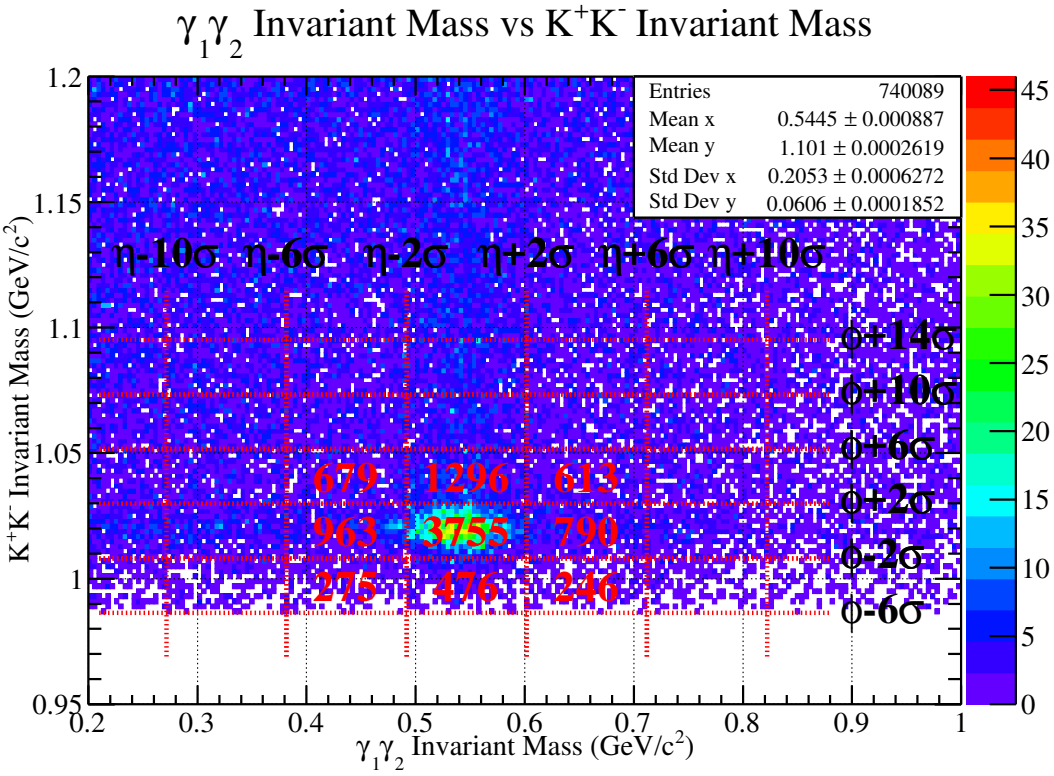

Figure 5.7: This figure shows the total number of counts in each box. To b be clear, the numbers in each are do not represent the total number of events, but rather the precise amount of statistics contained. Upon inspection, one can see evidence of $\phi\eta$ correlation, which is explained in the Conclusion section.

of 1000 events if there is no correlation present. After integrating the Gaussian fit for the ϕ and η mesons in the $\phi\eta$ intersection region, it was found that there were 3194 events corresponding to the ϕ fit, and 2993 events corresponding to the η fit. Both of these fits not only yield roughly the same number of events, but they also produce an event estimate which is a factor of three higher than what would have been there from the ϕ and η bands alone. The large increase in event statistics within the $\phi\eta$ intersection region strongly suggests that some type of correlation is present within this area of K^+K^- $\gamma\gamma$ phase space. It should be clearly noted that the nature of this correlation is not identified at this time. Moreover, it is unclear from this study as to whether or not the bound stats is mesonic or baryonic in nature. Additional studies on this area of phase space need

to be performed in order to establish that this spike in statistics is not coming from the $\gamma p \to N^* \phi$, $N^* \to p\eta$ topology.

5.2 Probabilistic Weightings for $\phi\eta$ Events

Throughout the course of history, physicists have tried clever ways of reducing the amount of background that is present under a given signal, or resonance. An example of this may be the classic side band subtraction, where the signal region will be defined by some average mass value, plus or minus a well defined width, or sigma. If one were to perform a cut about this region after particle identification and cuts, there may still be a good deal of background underneath the peak. In order to eliminated the background under the signal, one thing to do is use the background near the peak as reference for subtraction. To do this, one would use background events that are located at both higher and lower mass values far away from the signal, so long as the total mass range used is equal to the mass range for selecting the signal region. The side band subtraction method works well for some physics analyses, but not all. Side band subtraction is an issue with this analysis because the primary purpose is to observe structures in the $\phi\eta$ invariant mass spectra. Performing a side band subtraction is problematic because it allows events well below the $\phi\eta$ threshold mass to exist in the background spectra. Subtracting off these events from the primary signal region results in a final $\phi\eta$ invariant mass spectra which has negative event counts at low $\phi\eta$ mass values. Therefore, it is imperative to seek alternative background subtraction methods. The method that will be presented in this analysis uses a probabilistic weighting procedure which will be explained in this section.

5.2.1 Introduction to Probabilistic Event Weightings

One of the issues with a side band subtraction method is that it treats all events with a relative weight of one. The purpose of this section is to describe and propose a new method which does not treat all events with a value of one, but instead assigns a fractional weight to an event based off of a quality factor, or Q-factor. The quality value idea was first introduced in 2008 by M. Williams, M. Bellis, and C. A. Meyer in a paper titled "*Separating Signals from Non-Interfering Backgrounds using Probabilistic Event Weightings.*". The paper considers a generic situation in which there is a data set of n total events described by m coordinates, which will be written as $\vec{\xi}$. Within the data

set, there exists n_s total signal events and n_b total background events, and therefore $n = n_s + n_b$. In addition, both the signal and the background distributions are functions of the coordinates, such that $S(\vec{\xi})$ can be thought of as a signal distribution and $B(\vec{\xi})$ can be thought of as a background distribution. Contained within the set of coordinates $\vec{\xi}$, there exists a *reference coordinate* (ξ_r) with which we know the functional form of $S(\xi_r)$ and $B(\xi_r)$ *a priori*. The reference coordinate that is used in this thesis as well as in the paper mentioned above is the invariant mass of a final state. For many invariant mass distributions, the functional form of the signal distribution, $S(\xi_r)$ can be represented with a well known signal function. Some examples of well known signal functions are Gaussian, Voigtian, and Breit-Wigner distributions. In addition, the background distribution, $B(\xi_r)$, can be represented with an n^{th} degree polynomial function.

Since the signal and background distributions are not necessarily known *a priori* for the other coordinates, we use them to calculate a kinematic distance on an event by event basis. This is done by using the Equation (5.1).

$$d_{ij}^2 = \sum_{k \neq r} \left[\frac{\xi_k^i - \xi_k^j}{R_k} \right]^2 \tag{5.1}$$

In Equation(5.1), the total kinematic distance is calculated between some event i, as compared to another event j. This is done by taking the sum of the squared difference over all of the coordinates ξ_k, except for the reference coordinate ξ_r. The difference between coordinates is then normalized by the parameter R_k. The parameter R_k is the total maximum difference for a given coordinate ξ_k. An example of this may be the measurement of an azimuthal angle which spans from 0 to 2π. Therefore, the R_k for an azimuthal angle would be 2π. Upon closer inspection, one should realize that Equation(5.1) is simply a representation of the Pythagorean Theorem in a normalized $m-1$ dimensional kinematic space.

After calculating all of the kinematic distances for an event i, as compared to all other events within the data set $1...j...n$, it is then necessary to only keep the *nearest neighbors*. The nearest neighbors, by definition, are a subset of the n events which have the smallest kinematic distance with respect to the i^{th} event that is being considering. The purpose of only keeping the nearest neighbors stems from the assumption that a signal or background event with certain kinematic measurements, will share similar kinematic values with other signal or background events, respectively. The number of nearest neighbors for a set of events n is an arbitrary amount, and does not greatly effect

the quality factor calculation; so long as the amount is a small fraction of the total events n. Once the list of nearest neighbors is known for the i^{th} event, it is then necessary to plot their reference coordinate, ξ_r, onto a histogram. This histogram should contain a well understood signal distribution $S(\xi_r, \vec{\alpha})$, and background distribution $B(\xi_r, \vec{\alpha})$, as mentioned above; where $\vec{\alpha}$ is the set of known/unknown fit parameters used to describe the signal or background distribution. The histogram will then be fit by the sum of the signal and background distributions such that $F(\xi_r, \vec{\alpha}) = S(\xi_r, \vec{\alpha}) + B(\xi_r, \vec{\alpha})$. The quality factor can then be calculated by using the reference coordinate value for the i^{th} event and plugging it into the signal and background functions by using Equation(5.2), where $\hat{\alpha}$ is the set of fitted parameters for the signal or background distribution.

$$Q_i = \frac{S(\xi_r^i, \hat{\alpha}_i)}{S(\xi_r^i, \hat{\alpha}_i) + B(\xi_r^i, \hat{\alpha}_i)} \tag{5.2}$$

Once the quality factor is known for an event i, it can then be recorded and the analysis can loop over the next event and repeat the sequence all over again. Once all events have been run over, the quality factors for each event are used as a weight for plotting inside histograms. If the quality factor is correctly calculated for each event, the method should be able to separate signal from background. More specifically, if a histogram of the K^+K^- invariant mass is plotted with Q_i as the weight for the i^{th} event, one should see a 'pure' ϕ peak with absolutely no background. In addition, if the K^+K^- invariant mass is plotted with $1 - Q_i$ as the weight for the i^{th} event, one should see all background and absolutely no ϕ peak. Therefore, the sum of the signal histogram plus the background histogram should be equal to the K^+K^- invariant mass with all events having a weight of 1.

Determining the Number of Nearest Neighbors. After the kinematic distances are calculated for all events with respect to the i^{th} event, they are the sorted in order from smallest kinematic distance to largest kinematic distance. Only the the nearest neighbors, or the set of events with the smallest kinematic distance, will be used to determine the quality factor of a given event. For this analysis, there were a total of 16,981 events after selection cuts, and the number of nearest neighbors used was 500. This number was chosen somewhat arbitrarily; it is important to pick the smallest number possible such that the events used truly are those which share the most similar kinematic features to the event that is being considering. If the number was extremely large with respect to the total number of events, the analysis will not work properly. Events that

are background will have some nearest neighbors that are signal, and vice versa. Furthermore, the number number of nearest neighbors needs to be large enough such that a fit can converge with the filled histogram. If the number of nearest neighbors is too small, ROOT will fail to provide any signal or background information inside the histogram, and therefore calculation of a quality factor will be impossible. Considering these two constraints and testing with different values, it was found that the smallest number which did not result in *any* fitting failures was 500.

Fitting the K^+K^- Invariant Mass. Upon determining the nearest neighbors of the i^{th} event, the next step is to plot and fit the set of K^+K^- and $\gamma_1\gamma_2$ invariant mass distributions. As mentioned above, it is extremely difficult to model the invariant mass distribution for the K^+K^- final state. Simply picking a signal distribution plus a polynomial background is not enough to properly parameterize the K^+K^- invariant mass near or around the ϕ peak. After attempting several different combinations of signal and background functions, it was found that the best way to accurately describe both the ϕ and the background near it is to use convoluted functions. A convolution is the operation between two functions which expresses how the shape of one function is modified by the other. The purpose for utilizing a convoluted function when attempting to fit an invariant mass histogram is to describe both the shape of the distribution as well as the inherent resolution of the data. Since both the ϕ peak and the background surrounding it contain similar resolutions, it is appropriate to fit the K^+K^- invariant mass distribution with the summation of a signal function plus a background function, both of which are then convoluted by a third function which manages the resolution.

The signal function chosen to describe the ϕ peak is a relativistic Breit-Wigner (Equation 5.3).

$$|Q_1(m)|^2 = A * |F_1(m) * \Delta_1(m)|^2 \tag{5.3}$$

Contained within this equation is a fit parameter, A, which simply scales the function in order to match the distribution. Also contained in this equation are two functions of mass, the Blatt-Weisskopf centrifugal-barrier factor for a spin 1 particle (Equation 5.4),

$$F_1(m) = \sqrt{\frac{2 * \sqrt{m^2 - m_K^2}}{\sqrt{m^2 - m_K^2} + 1}} \tag{5.4}$$

and a standard Breit-Wigner (Equation 5.5) for a particle with spin 1.

$$\Delta_1(m) = \frac{m_o * \Gamma_o}{m_o^2 - m^2 - i m_o \Gamma_1(m)} \tag{5.5}$$

The Blatt-Weisskopf function plays an important role in the fit since it forces the signal function to be equal to zero when the K^+K^- mass is at threshold. It should be noted that $\sqrt{m^2 - m_K^2}$ appears throughout many of the equations mentioned. This smaller function represents the magnitude of the breakup momentum for either the K^+ or K^- daughter particle, given some parent mass m, in the rest frame of the parent particle. Additionally, the mass dependent width (Equation 5.6) also helps to describe the changing width of the ϕ due to the K^+K^- mass near threshold.

$$\Gamma_1(m) = \Gamma_o \frac{m_o}{m} \frac{\sqrt{m^2 - m_K^2}}{\sqrt{m_o^2 - m_K^2}} \frac{F_1^2(m)}{F_1^2(m_o)} \tag{5.6}$$

Finally, in many of the equations, m_K is the mass of a $K^{+/-}$, m_o is the ϕ mass value as determined by the fit, and Γ_o is the natural width of the ϕ. The value chosen for this parameter was taken from the PDG and is $\Gamma_o = 0.004266 \frac{GeV}{c^2}$.

Plotted along with the signal function is the background function which is simply a third degree polynomial, given by Equation (5.7).

$$b(m) = C_1 * (m - C_0)^3 + C_2 * (m - C_0)^2 + C_3 * (m - C_0) \tag{5.7}$$

The background equation has three free parameters and one fixed parameter. The free parameters are the coefficients in front of the powered terms of m; specifically C_1, C_2, and C_3. Since the background shape can drastically change due to the event and its nearest neighbors, these parameters are not given any restriction on their values (Table 5.1). The one fixed parameter is C_0 which is set to $0.987354 \frac{GeV}{c^2}$. This value is the smallest possible mass which can produce the K^+K^- final state, and is easily derived by simply performing the calculation $m_{K^+} + m_{K^-} = 2 * m_{K^\pm} = 0.987354 \frac{GeV}{c^2}$. The purpose of fixing this parameter is force the polynomial background to have a root at the K^+K^- threshold. While attempting different fit functions to describe the K^+K^- invariant mass, it was found that the polynomial function often exaggerated, or over fit the area near the K^+K^- threshold. This caused an effect which resulted in weighted histograms that took away good events near the low mass side of the ϕ peak. Forcing the background function to be equal to zero at the K^+K^- threshold fixed this issue.

To complete the fit of the K^+K^- invariant mass, the signal and background function are added together, then convoluted by a Gaussian in order to compensate for the kaon resolution of the GlueX spectrometer. Although the signal and background functions mentioned above had to be programmed by hand, the convolution of these functions with a Gaussian could be fed into the ROOT library using the TF1Convolution object. More precisely, the total function used to describe the K^+K^- invariant mass for all events is given in Equation (5.8).

$$T(m) = \int \left[s(m') + b(m')\right] G(m - m')dm' \tag{5.8}$$

In the equation above, m' is simply a dummy variable for integration, and m represents the K^+K^- invariant mass. The function $s(m')$ is a relativistic Breit-Wigner (Equation 5.3), and the $b(m')$ is the polynomial background function referenced in Equation (5.7). Finally, $G(m - m')$ is the Gaussian function which is responsible for describing the resolution. This particular Gaussian function has one free parameter, and one fixed parameter. The free parameter is the width of the Gaussian, and the fixed parameter is the mean of the Gaussian which is simply set to zero. Because the Gaussian is being convoluted over the range of the fit, the value of the mean in this instance does not matter. Adding all things together, the total function listed in Equation (5.8) has one independent variable, two fixed parameters, and six free parameters, half of which are restricted (Table 5.1). Once a fit has converged, the parameters of the total function can be extracted and used to plot a signal function and a background function. This procedure is mathematically allowed due to the distributive property of convolutions; and therefore the final background and signal function can be written in Equation (5.9) and Equation (5.10), respectively.

$$B(m) = \int b(m')G(m - m')dm' \tag{5.9}$$

$$S(m) = \int s(m')G(m - m')dm' \tag{5.10}$$

Examples of different fits of the K^+K^- invariant mass distributions have been provided in Figures[5.8][5.9][5.10]. Each figure contains a blue line which represents the total fit of the data (Equation 5.8), a green line which represents the signal portion of the fit (Equation 5.10), and a red line which represents the background portion of the fit (Equation 5.9). Located within each

plot is also a vertical arrow which is pointed in the downward direction. This arrow represents the invariant mass value of the event for which the quality factor is being calculated. Also contained within each figure is a legend with the values of the parameters for each fit.

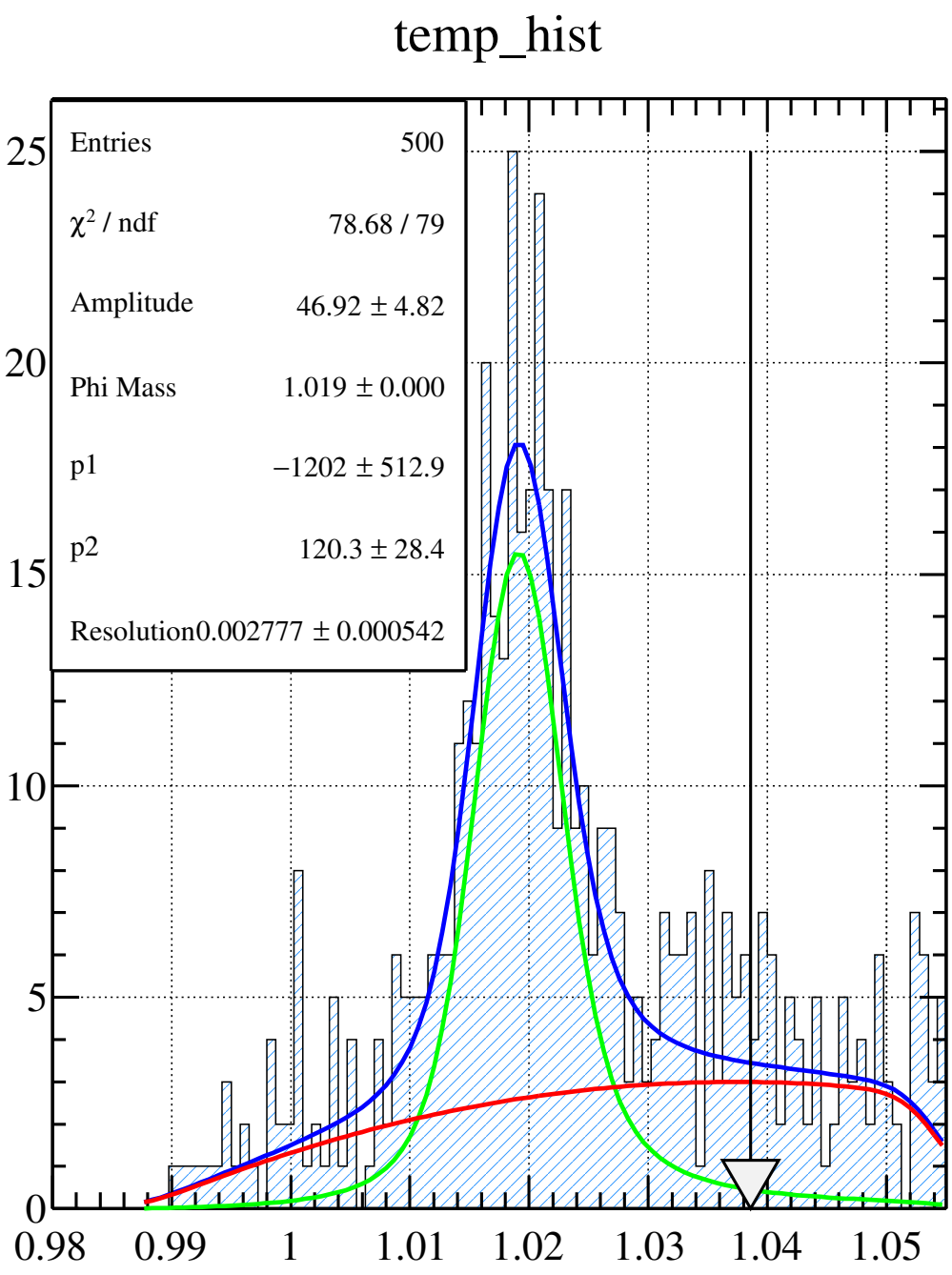

Figure 5.8: A fit which will result in an extremely low quality factor due to the very few signal events in comparison to background events at the location of the arrow, or invariant mass of the event being considered.

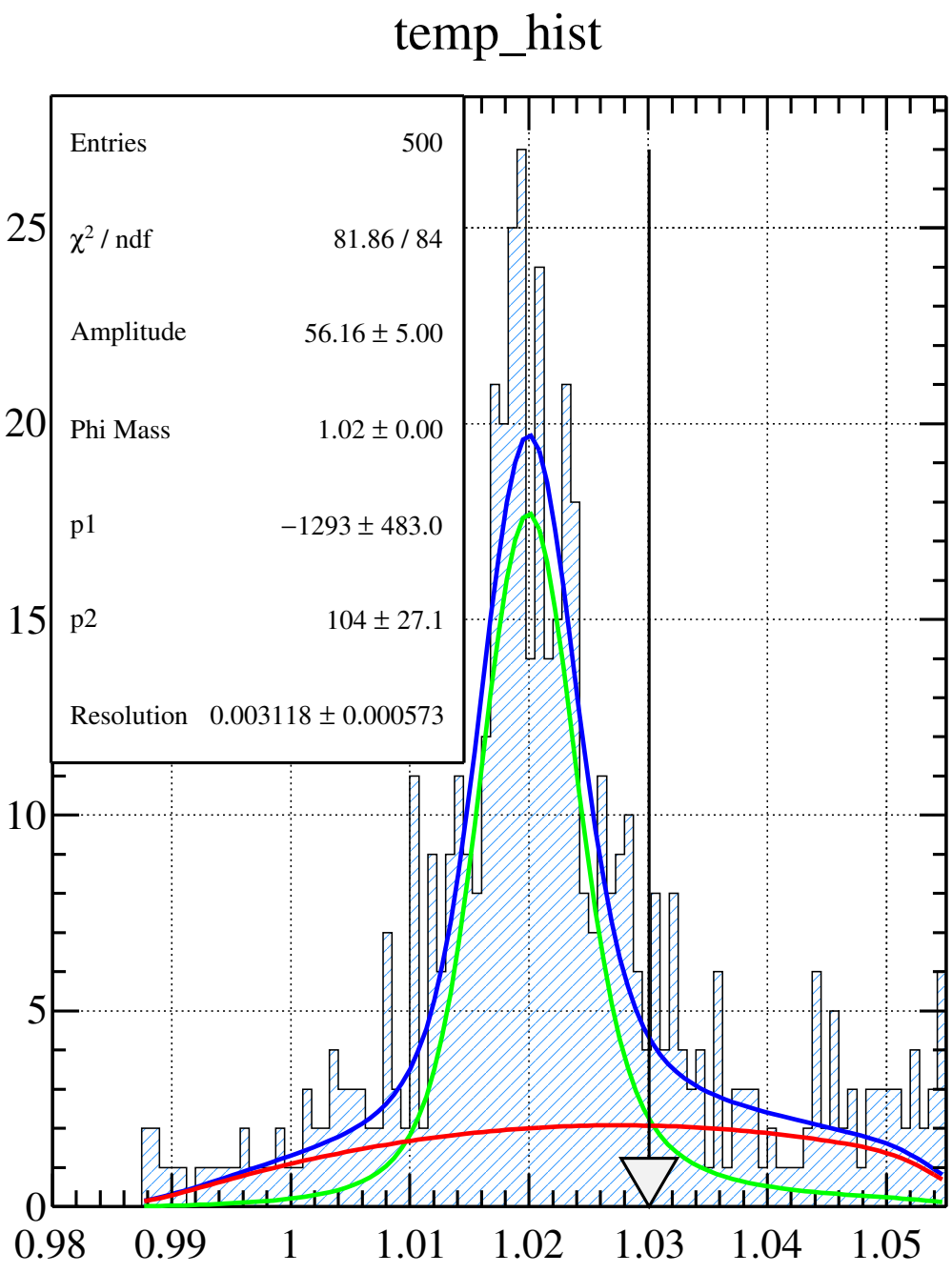

Figure 5.9: A fit which will result in a quality factor around 0.5, due to the fact that there are roughly the same signal and background events at the location of the arrow, or invariant mass of the event being considered.

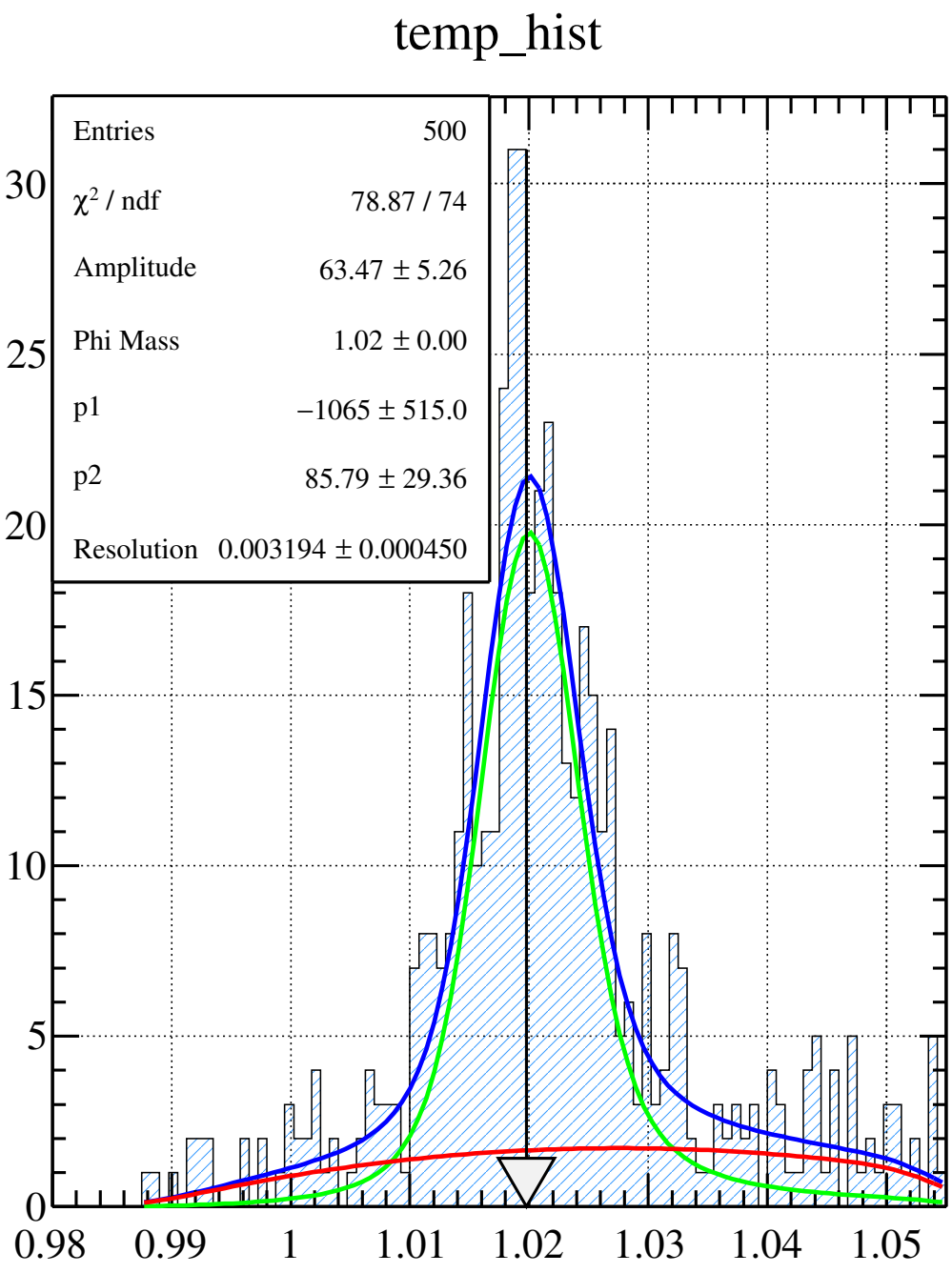

Figure 5.10: A fit which will result in a very high quality factor due to the large number signal events in comparison to background events at the location of the arrow, or invariant mass of the event being considered.

K^+K^- Invariant Mass Functions:

Function	Parameters	Initial Values	Restricted Range
Relativistic B.W.	Amplitude	10	$0-100$
	m_ϕ	1.019	$1.01-1.03$
3^{rd} Degree Polynomial	C_0	0.987354	Fixed
	C_1, C_2, C_3	$-1200, 200, 200$	Free
Gaussian	μ	0	Fixed
	σ	0.005	$0-0.05$

Table 5.1: A table which summarizes the parameters and functions used to fit the K^+K^- invariant mass histograms.

Fitting the $\gamma_1\gamma_2$ Invariant Mass. On top of fitting the K^+K^- invariant mass, it is also necessary to fit the $\gamma_1\gamma_2$ invariant mass. Fitting this distribution is far more simple than what was needed to describe the K^+K^- invariant mass. The η resonance sits on top of a simple background, and is far enough away from the dominant π^0 peak that further inspection of the background is not necessary. In addition, since the η resonance is nowhere near the threshold for $\gamma\gamma$, performing any type of advanced fit to include breakup momentum and resolution effect is not necessary. Therefore, the $\gamma_1\gamma_2$ invariant mass spectra was fit by utilizing the summation of a signal function and a background function. The signal function is a Voigtian (Equation 5.12), which is technically a non relativistic Breit-Wigner (Equation 5.11) convoluted with a Gaussian. This convolution is necessary because the GlueX resolution of the η resonance is much greater than the natural width of the η meson, which is on the order of a keV. In the total signal function (Equation 5.12) there is one independent variable, and three fit parameters, and one fixed parameter. The independent variable is the $\gamma_1\gamma_2$ invariant mass, and the fixed parameter is the natural width of the η meson which is listed in the PDG as $\Gamma_o = 1.31keV$. The fit parameters of the function are the amplitude, A which simply scales the function to fit the statistics, the mass value of the η for the fit μ, and the resolution of the η. The limits and starting values of all parameters are summarized in Table 5.2.

$$|\Delta(m)|^2 = \frac{\Gamma_o}{(m-\mu)^2 + \frac{\Gamma_o^2}{4}} \tag{5.11}$$

$$S(m) = A \int |\Delta(m')|^2 G(m-m')dm' \tag{5.12}$$

The background function that was chosen to describe the $\gamma\gamma$ background was a Chebyshev polynomial (Equation 5.13). It should be noted that the functional form of this third order polynomial is different than the one that was used to describe the K^+K^- because there is no threshold effect that has to be accounted for in the $\gamma_1\gamma_2$ invariant mass. This function has four free fit parameters with no restrictions on value due to the variability of background shapes in this analysis.

$$B(m) = C_3 * x^3 + C_2 * x^2 + C_1 * x + C_0 \tag{5.13}$$

Finally, the total function that was used to ultimately fit the $\gamma_1\gamma_2$ invariant mass distributions was the sum of Equation 5.12 and Equation 5.13. A summary of all parameters and functions used to fit the $\gamma_1\gamma_2$ invariant mass is given in Table 5.2.

Examples of different fits of the $\gamma_1\gamma_2$ invariant mass distributions have been provided in Figures[5.11][5.12][5.13]. Just like the examples given for the K^+K^- invariant mass fits, each figure contains a blue line which represents the total fit of the data. The total fit in this particular instance is simply the sum of a Voigtian and a third degree Chebyshev polynomial. The figures also contain a green line which represents the signal portion of the fit and a red line which represents the background portion of the fit. These are described by a Voigtian and third degree Chebyshev polynomial, respectively. Located within each plot is also a vertical arrow which is pointed in the downward direction. This arrow represents the invariant mass value of the event for which the quality factor is being calculated. Also contained within each figure is a legend with the values of the parameters for each fit.

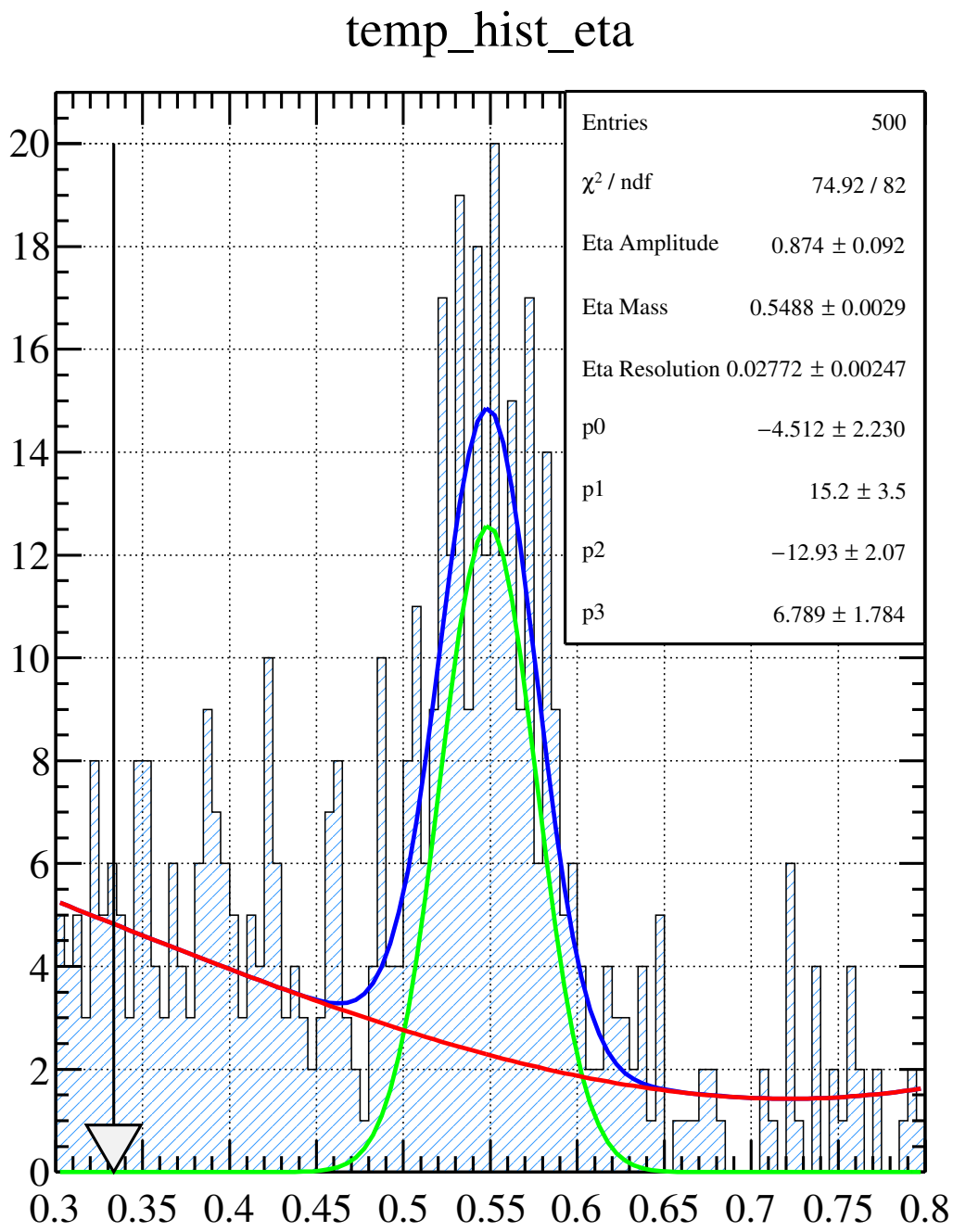

Figure 5.11: A fit which will result in an extremely low quality factor due to the very few signal events in comparison to background events at the location of the arrow, or invariant mass of the event being considered.

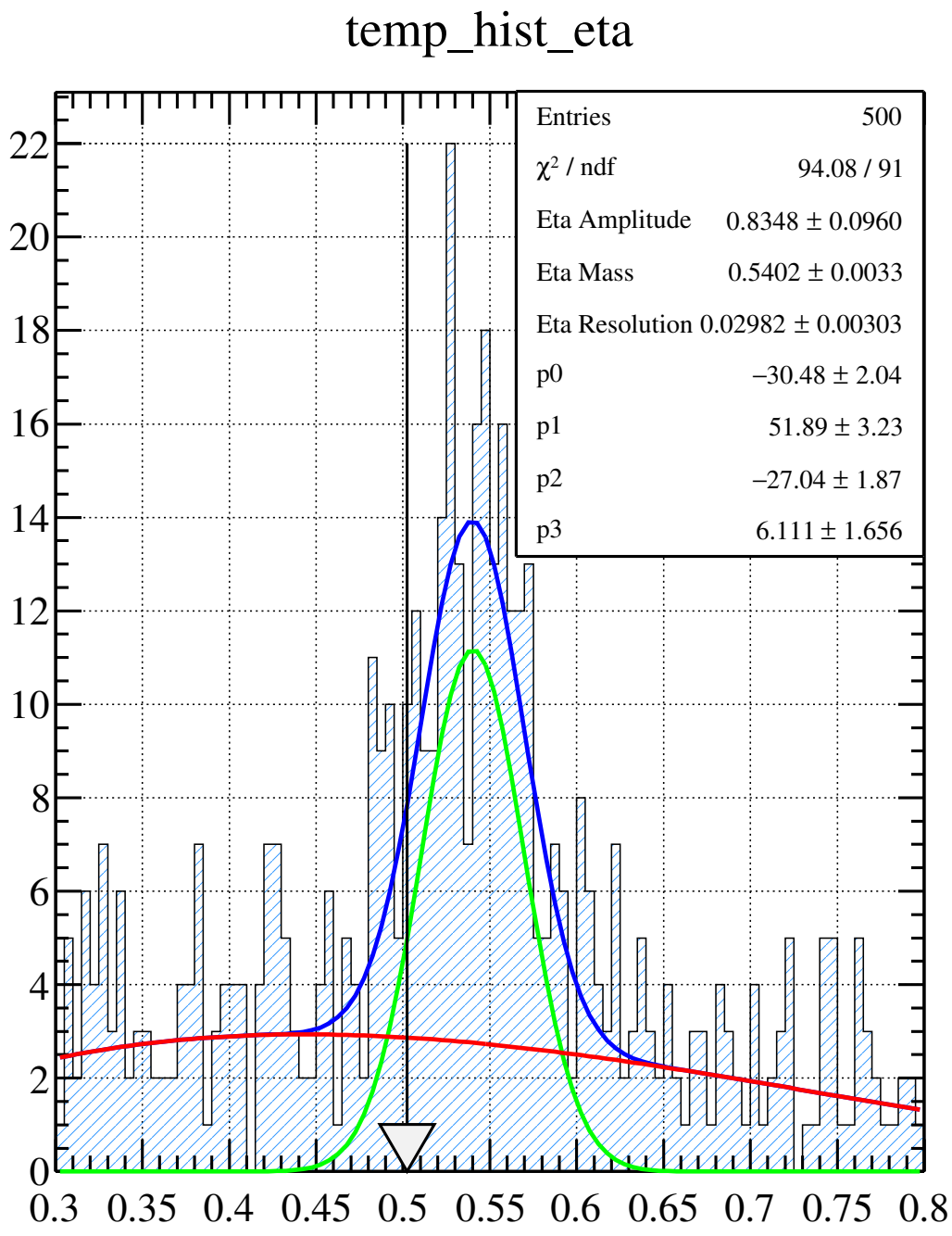

Figure 5.12: A fit which will result in a quality factor somewhat above 0.5, due to the fact that there are slightly more signal events as compared to background events at the location of the arrow, or invariant mass of the event being considered.

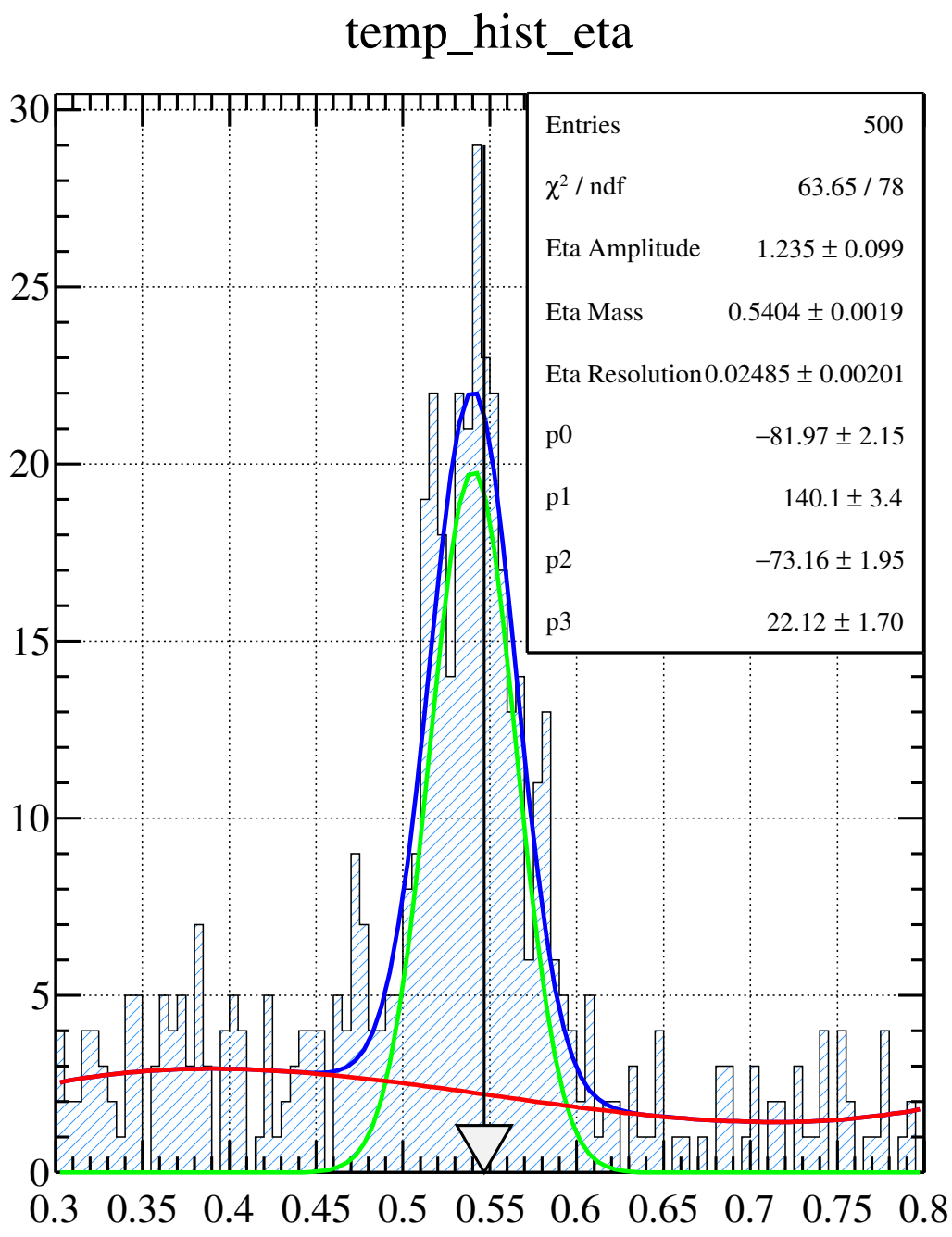

Figure 5.13: A fit which will result in a very high quality factor due to the large number signal events in comparison to background events at the location of the arrow, or invariant mass of the event being considered.

$\gamma_1\gamma_2$ Invariant Mass Functions:

Function	Parameters	Initial Values	Restricted Range
Voigtian	Amplitude	2	$0-5$
	m_η	0.547	$0.52-0.56$
	σ	0.02	$0.001-0.1$
	Γ	0.00000131	Fixed
3^{rd} Chebyshev Polynomial	C_0, C_1, C_2, C_3	None	Free

Table 5.2: A table which summarizes the parameters and functions used to fit the $\gamma_1\gamma_2$ invariant mass histograms.

5.2.2 Three Quality Factor Methods

In order to thoroughly study the $\phi\eta$ final state, a total of three unique quality factor methods were attempted. Each of these analyses follow the standard quality factor prescription detailed in Subsection 5.2.1. Each analysis is unique because a different set of kinematic observables was used to find the set nearest neighbors for each event.

1. (ϕ Only) The first quality factor method considered the kinematic observables of the $K+K-$ system, and therefore can only separate the ϕ signal from the $K+K-$ background. The quality factor for this analysis will be denoted with Q_ϕ.

2. (η Only) The second quality factor method only considered the kinematics observables of the $\gamma\gamma$ system, and therefore only separates the η signal from the $\gamma\gamma$ background. The quality factor for this analysis will be denoted with Q_η.

3. ($\phi\eta$) The third and final quality factor analysis considered the kinematics observables for *both* the $K+K-$ system and the $\gamma\gamma$ system. The quality factor for this analysis will be denoted with $Q_{\phi\eta}$.

The specific list of kinematic observables and how a quality factor was calculated for each analysis is detailed in Subsections 5.2.2 and 5.2.2, respectively. It should be noted that all three analyses use the same fit functions for the K^+K^- invariant mass distribution (Subsection 5.2.1), and $\gamma\gamma$ invariant mass distribution (Subsection 5.2.1). In addition, all three analyses only accept the 500 nearest neighbors (Subsection 5.2.1).

Calculating the Kinematic Distance Between Events. As mentioned in Subsection 5.2.2 , there are a total of three unique quality factor analyses attempted in this thesis, and therefore there are three unique calculations to find the kinematic distance between events.

ϕ **Only.** The list of kinematic observables used to identify the ϕ meson and to ultimately calculate Q_ϕ are given in Table 5.3.

ξ_k	Coordinate	Maximum Range of Coordinate
ξ_0	$K^+_{HE\cos(\theta)}$	2
ξ_1	$K^+_{HE\phi}$	2π radians
ξ_2	$GJ, \cos(\theta)$	2
ξ_3	GJ, ϕ	2π radians
ξ_4	γ_E	4 GeV
ξ_5	t	$3.3\frac{GeV^2}{c^4}$
ξ_r	K^+K^- Invariant Mass	Reference Coordinate

Table 5.3: A table which summarizes the coordinates used to describe the $\gamma p \to pX$; $X \to \phi Y$ $\phi \to K^+K^-$; final state. This set of coordinates will ultimately lead to the calculation of Q_ϕ The coordinates ξ_0 through ξ_5 are used in the kinematic distance equation, described by Equation (5.1). The last coordinate is the reference coordinate for this analysis.

Since this quality factor analysis is only attempting to separate the ϕ from K^+K^- background, there is no need to include any information about the η or its decay products, $\gamma\gamma$. Therefore, in order to properly identify the $\gamma p \to pX$; $X \to \phi Y$ $\phi \to K^+K^-$ final state, a total of six coordinates are needed. Two of the six coordinates come from the angular distributions of the daughter states of ϕ: $K^+_{HE\cos(\theta)}$, $K^+_{HE\phi}$; where the angles ϕ and θ are the polar coordinates in the helicity reference frame, or the rest frame of the ϕ. Two more of the eight total coordinates will come from the angular distributions of ϕ. Much like the kaons, these coordinates will be $GJ, \cos(\theta)$ and GJ, ϕ; where ϕ and $\cos(\theta)$ are polar angles in the Gottfried-Jackson frame; or the rest frame of the $K^+K^-\gamma\gamma$ parent state. The last two coordinates needed are the beam energy (γ_E), and the momentum transfer, t. Since t is the well known Mandelstam variable, t is related to the beam energy and the four momentum of the $\phi\eta$ parent state, such that $t^2 = (\gamma^\mu - X^\mu)^2$; where γ^μ is the energy-momentum four vector for the beam, and X^μ is the energy-momentum four vector for the $\phi\eta$ parent state. Since t, the beam energy γ_E, and the mass of the $K^+K^-\gamma\gamma$ parent state is known, the magnitude of the $K^+K^-\gamma\gamma$ parent state momentum is directly proportional to these measurements. Knowing the magnitude of the momentum and the mass of the $K^+K^-\gamma\gamma$ parent state allows us to fully describe the $\gamma p \to pX$; $X \to \phi Y$ $\phi \to K^+K^-$ reaction. The final detail that needs to be mentioned is the reference coordinates that are used in this quality factor analysis. Because it is imperative

to have a pure ϕ signal, the reference coordinate for this procedure will be the K^+K^- invariant mass. Although this coordinate do not play a role in the calculation of the kinematic distance, it is imperative to define it as the reference coordinate which will ultimately serve as the tool to separate signal events from background events, and to calculate Q_ϕ.

η **Only.** The list of kinematic observables used to identify the η meson and to ultimately calculate Q_η are given in Table 5.4.

ξ_k	Coordinate	Maximum Range of Coordinate
ξ_0	$\gamma_{HE\cos(\theta)}$	2
ξ_1	$\gamma_{HE\phi}$	2π radians
ξ_2	$GJ, \cos(\theta)$	2
ξ_3	GJ, ϕ	2π radians
ξ_4	γ_E	4 GeV
ξ_5	t	$3.3\frac{GeV^2}{c^4}$
ξ_r	$\gamma_1\gamma_2$ Invariant Mass	Reference Coordinate

Table 5.4: A table which summarizes the coordinates used to describe the $\gamma p \to pX$; $X \to \eta Y$; $\eta \to \gamma\gamma$ final state. This set of coordinates will ultimately lead to the calculation of Q_η The coordinates ξ_0 through ξ_5 are used in the kinematic distance equation, described by Equation (5.1). The last coordinate is the reference coordinate for this analysis.

This quality factor analysis is only attempting to separate the η from $\gamma\gamma$ background, there is no need to include any information about the ϕ or its decay products, K^+K^-. Therefore, in order to properly identify the $\gamma p \to pX$; $X \to \eta Y$; $\eta \to \gamma\gamma$ final state, a total of six coordinates are needed. Two of the six coordinates come from the angular distributions of the daughter states of η: $\gamma_{HE\cos(\theta)}$, $\gamma_{HE\phi}$; where the angles ϕ and θ are the polar coordinates in the helicity reference frame, or the rest frame of the η. Two more of the eight total coordinates will come from the angular distributions of η. Much like the photon, these coordinates will be $GJ, \cos(\theta)$ and GJ, ϕ; where ϕ and $\cos(\theta)$ are polar angles in the Gottfried-Jackson frame; or the rest frame of the $K^+K^-\gamma\gamma$ parent state. The last two coordinates needed are the beam energy (γ_E), and the momentum transfer, t. Since t is the well known Mandelstam variable, t is related to the beam energy and the four momentum of the $\phi\eta$ parent state, such that $t^2 = (\gamma^\mu - X^\mu)^2$; where γ^μ is the energy-momentum four vector for the beam, and X^μ is the energy-momentum four vector for the $\phi\eta$ parent state. Since t, the beam energy γ_E, and the mass of the $K^+K^-\gamma\gamma$ parent state is known, the magnitude of the

$K^+K^-\gamma\gamma$ parent state momentum is directly proportional to these measurements. Knowing the magnitude of the momentum and the mass of the $K^+K^-\gamma\gamma$ parent state allows us to fully describe the $\gamma p \to pX$; $X \to \eta Y$; $\eta \to \gamma\gamma$ reaction. The final detail that needs to be mentioned is the reference coordinates that are used in this quality factor analysis. Because it is imperative to have a pure η signal, the reference coordinate for this procedure will be the $\gamma\gamma$ invariant mass. Although this coordinate does not play a role in the calculation of the kinematic distance, it is imperative to define it as the reference coordinate which will ultimately serve as the tool to separate signal events from background events, and to calculate Q_η.

$\phi\eta$. The list of kinematic observables used to identify the ϕ meson and the η meson; and to ultimately calculate $Q_{\phi\eta}$ are given in Table 5.5.

ξ_k	Coordinate	Maximum Range of Coordinate
ξ_0	$K^+_{HE\cos(\theta)}$	2
ξ_1	$K^+_{HE\phi}$	2π radians
ξ_2	$\gamma_{HE\cos(\theta)}$	2
ξ_3	$\gamma_{HE\phi}$	2π radians
ξ_4	$GJ, \cos(\theta)$	2
ξ_5	GJ, ϕ	2π radians
ξ_6	γ_E	4 GeV
ξ_7	t	$3.3\frac{GeV^2}{c^4}$
ξ_r	K^+K^- Invariant Mass	Reference Coordinate
ξ_r	$\gamma_1\gamma_2$ Invariant Mass	Reference Coordinate

Table 5.5: A table which summarizes the coordinates used to describe the $\gamma p \to pX$; $X \to \phi\eta$ $\phi \to K^+K^-$; $\eta \to \gamma\gamma$ final state. This set of coordinates will ultimately lead to the calculation of $Q_{\phi\eta}$ The coordinates ξ_0 through ξ_7 are used in the kinematic distance equation, described by Equation (5.1). The last two coordinates are the reference coordinates for this analysis.

The final quality factor analysis is attempting to identify both the ϕ and η mesons and to also reject any background. It should be noted that the backgrounds for this analysis are different and include $\phi\gamma\gamma$, ηK^+K^-, and $K^+K-\gamma\gamma$. Therefore, in order to properly identify the $\gamma p \to pX$; $X \to \phi\eta$ $\phi \to K^+K^-$; $\eta \to \gamma\gamma$ final state, a total of eight coordinates are needed. Four of the eight coordinates come from the angular distributions of the daughter states of ϕ and η. More specifically, the four coordinates are $K^+_{HE\cos(\theta)}$, $K^+_{HE\phi}$, $\gamma_{HE\cos(\theta)}$, $\gamma_{HE\phi}$; where the angles ϕ and θ are the polar coordinates in the helicity reference frame. It should be noted that since the K^+ and γ particles

are daughters of different parent states, they will have different helicity frames which are relative to the rest frames of ϕ and η mesons, respectively. Two more of the eight total coordinates will come from the angular distributions of ϕ and η. Much like the K^+ and γ particles, these coordinates will be $GJ, \cos(\theta)$ and GJ, ϕ; where ϕ and $\cos(\theta)$ are polar angles in the Gottfried-Jackson frame; or the rest frame of the $\phi\eta$ parent state. The last two coordinates needed to describe the $\gamma p \to p\phi\eta$ final state is the beam energy (γ_E), and the momentum transfer, t. Since t is the well known Mandelstam variable, t is related to the beam energy and the four momentum of the $\phi\eta$ parent state, such that $t^2 = (\gamma^\mu - X^\mu)^2$; where γ^μ is the energy-momentum four vector for the beam, and X^μ is the energy-momentum four vector for the $\phi\eta$ parent state. Since t, the beam energy γ_E, and the mass of the $\phi\eta$ parent state is known, the magnitude of the $\phi\eta$ parent state momentum is directly proportional to these measurements. Knowing the magnitude of the momentum and the mass of the $\phi\eta$ parent state allows us to fully describe the $\gamma p \to p\phi\eta$ reaction. The final detail that needs to be mentioned is the reference coordinates that are used in this quality factor analysis. Because it is imperative to have a pure ϕ and η signal, there will be two reference coordinates for this procedure. One of them will be the K^+K^- invariant mass, and the other will be the $\gamma_1\gamma_2$ invariant mass. Although these coordinates do not play a role in the calculation of the kinematic distance, it is imperative to define them as the reference coordinates which will ultimately serve as the tool to separate signal events from background events, and to calculate $Q_{\phi\eta}$.

Calculating the Quality Factor. Once the fits of the K^+K^- and $\gamma_1\gamma_2$ invariant mass histograms have converged, the final step of calculating a quality factor can be performed. This is done by knowing the signal and background functions, as well as their fitted parameters, for both the K^+K^- and $\gamma_1\gamma_2$ distributions. Knowing the parameters of the fit will allow the user to accurately estimate the number of signal events and the number of background events for a given invariant mass value. The invariant mass value that should be used is the one which corresponds to the event that is being studied, and the parameters are determined by the fit of the invariant mass distribution of nearest neighbors. More specifically, the quality factor associated with the K^+K^- invariant mass distribution will be Equation 5.14.

$$Q_\phi = \frac{S(m_{KK})}{S(m_{KK}) + B(m_{KK})} \tag{5.14}$$

In Equation (5.14), the function $S(m)$ is the convoluted relativistic Breit-Wigner described by Equation (5.10), and the function $B(m)$ is the convoluted third degree polynomial described by Equation (5.9). Lastly, the m_{KK} variable describes the K^+K^- mass of the event being considered. The quality factor associated with the $\gamma_1\gamma_2$ invariant mass distribution will be Equation 5.15.

$$Q_\eta = \frac{S(m_{\gamma\gamma})}{S(m_{\gamma\gamma}) + B(m_{\gamma\gamma})} \tag{5.15}$$

In Equation 5.15, the function $S(m)$ is a Voigtian function, which is the convolution of a non-relativistic Breit-Wigner with a Gaussian, described by Equation 5.12. The function $B(m)$ is the simply a third degree Chevyshev polynomial described by Equation 5.13. Lastly, the $m_{\gamma\gamma}$ variable describes the $\gamma\gamma$ invariant mass of the event being considered. The last quality factor which considers both the kinematics of the ϕ and the η is given in Equation (5.16).

$$Q_{\phi\eta} = \frac{S(m_{KK})}{S(m_{KK}) + B(m_{KK})} * \frac{S(m_{\gamma\gamma})}{S(m_{\gamma\gamma}) + B(m_{\gamma\gamma})} \tag{5.16}$$

In Equation (5.16), the signal and background functions for the K^+K^- and $\gamma\gamma$ invariant mass distributions are the same as those mentioned in Equation 5.14 and Equation 5.15, respectively.

The key difference between all three quality factor calculations comes from the fact that they are all using a different set of kinematic variables to determine a set of nearest neighbors. Therefore, the K^+K^- invariant mass distribution using the ϕ Only method will be different from the K^+K^- invariant mass distribution using the $\phi\eta$ method. Conversely, the $\gamma\gamma$ invariant mass distribution using the η Only method will be different from the $\gamma\gamma$ invariant mass distribution using the $\phi\eta$ method. This subtlety will result in different $\phi\eta$ invariant mass yields, depending on the quality factor method that is being considered.

Quality Factor Highlights. The effectiveness of the quality factor approach is highlighted in Figure 5.14 and Figure 5.15. Figure 5.14 shows what the K^+K^- invariant mass distribution looks like when plotting events with weights Q_ϕ and with weights $1 - Q_\phi$. One can clearly see that the quality factor effectively separated the signal ϕ meson from the K^+K^- background. Figure 5.15 shows what the $\gamma\gamma$ invariant mass distribution looks like when plotting events with weights Q_η and with weights $1 - Q_\eta$. One can clearly see that the quality factor effectively separated the signal η meson from the $\gamma\gamma$ background.

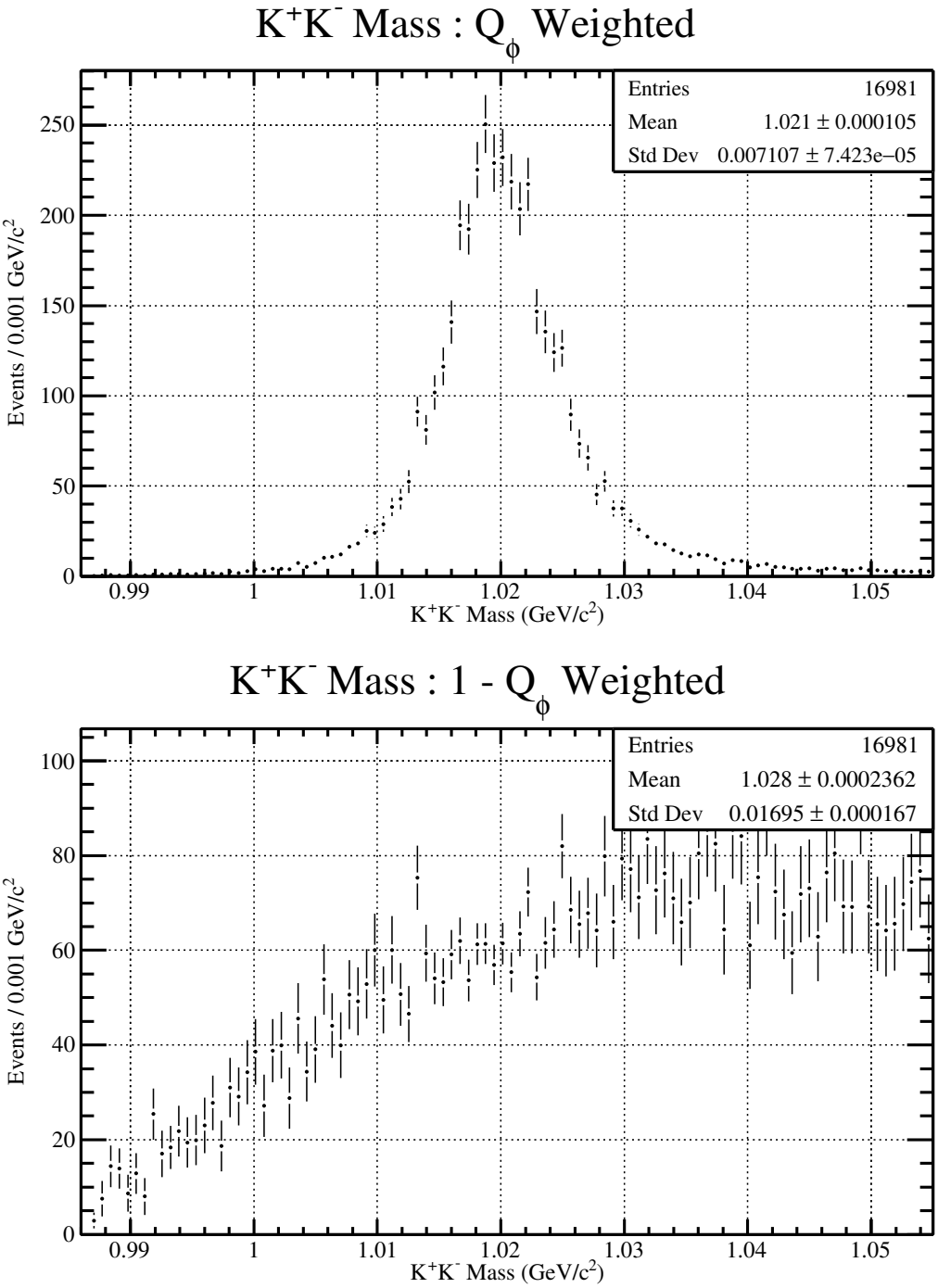

Figure 5.14: The K^+K^- invariant mass distribution plotted with the signal weight, Q_ϕ and the background weight $1 - Q_\phi$.

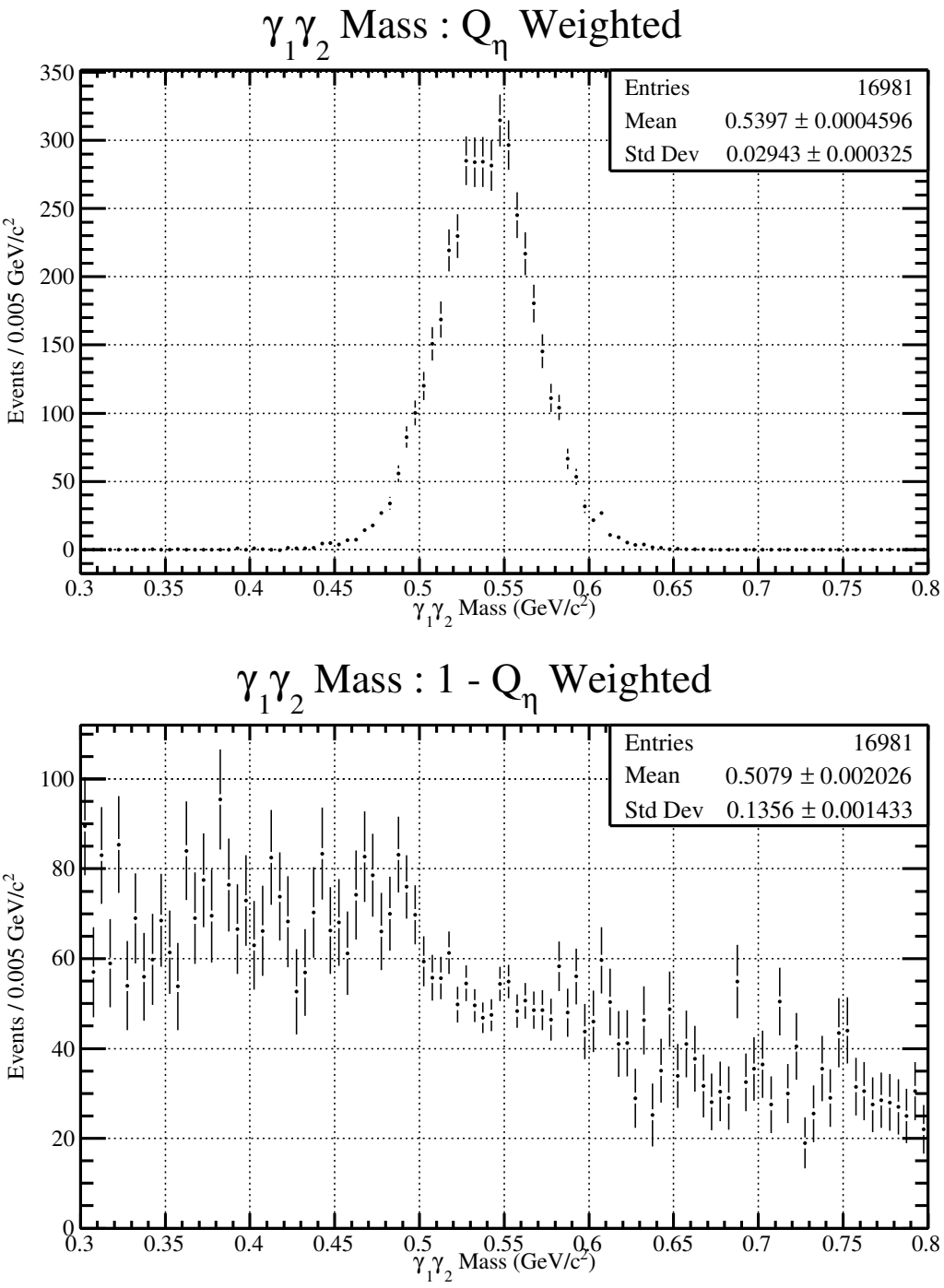

Figure 5.15: The $\gamma\gamma$ invariant mass distribution plotted with the signal weight, Q_η and the background weight $1 - Q_\eta$.

5.3 Analysis of $\phi\eta$ Invariant Mass Plot

After performing all cuts on the input data and establishing quality factors for three different nearest neighbor approaches, the $\phi\eta$ invariant mass can be studied. In order to study this distribution, a total of five different methods were used to identify a $\phi\eta$ final state. Each approach, along with supporting plots, are given in the subsections of this chapter.

5.3.1 Elliptical Mass Approach

There was no weighting method used for this approach. Every event has a relative weight of 1. This analysis has three sets of histograms, one of them is signal plus background, another is just background and the third is the difference between the previous two, which can be interpreted at a signal distribution.

5.3.2 $Q_\phi * w_\eta$ Weighting

This analysis uses the quality factor weights for the ϕ only method described in Subsection 5.2.2. Since this method only separates ϕ signal from K^+K^- background, there can be additional background in the $\gamma\gamma$ invariant mass plot. Therefore, an additional *weight for the* η, or w_η is applied to all events. This weight is determined by plotting the $\gamma\gamma$ invariant mass and fitting a signal plus background distribution to the data. Knowing the functional form of the signal distribution and the background distribution allows each event to carry an extra weight given its $\gamma\gamma$ invariant mass. It should be noted that this approach is different from the quality factor method because it considers all data and does not utilize a nearest neighbors approach.

5.3.3 $Q_\eta * w_\phi$ Weighting

This analysis uses the quality factor weights for the η only method described in Subsection 5.2.2. Since this method only separates η signal from $\gamma\gamma$ background, there can be additional background in the K^+K^- invariant mass plot. Therefore, an additional *weight for the* ϕ, or w_ϕ is applied to all events. This weight is determined by plotting the K^+K^- invariant mass and fitting a signal plus background distribution to the data. Knowing the functional form of the signal distribution and the background distribution allows each event to carry an extra weight given its K^+K^- invariant mass. It should be noted that this approach is different from the quality factor method because it considers all data and does not utilize a nearest neighbors approach.

5.3.4 $Q_{\phi\eta}$ Weighting

This analysis uses the quality factor weights for the $\phi\eta$ only method described in Subsection 5.2.2. Since this method separates both η signal from $\gamma\gamma$ background, and ϕ signal from K^+K^- background, the only weight that is needed event by event is $Q_{\phi\eta}$.

5.3.5 $Q_\phi * Q_\eta$ Weighting

This analysis simply multiplies the quality factor from the ϕ only analysis with the quality factor from the η only analysis.

CHAPTER 6

SUMMARY

I will write my summary here.

BIBLIOGRAPHY

[1] https://www.jlab.org/accelerator-science.

[2] GlueX/Hall D Calorimeter Final Design and Safety Review, Feb 2008. https://halldweb.jlab.org/DocDB/0009/000988/001/fcal.pdf.

[3] The GlueX / HallD Central Drift Chamber, Jul 2008. https://halldweb.jlab.org/DocDB/0009/000990/011/cdc_dr.pdf.

[4] Nov 2013. https://gluex.phys.uregina.ca/pictures.

[5] *Modern Particle Physics*. Cambridge University Press, 2013.

[6] Diamond on goniometer, Jan 2015. https://logbooks.jlab.org/book/halld.

[7] Hall D / GlueX Technical Construction Report, Jul 2017. https://halldweb.jlab.org/DocDB/0025/002511/006/tcr.pdf.

[8] Jan 2018. JLab Picture Exchange - https://www.jlab.org.

[9] Exploring the nature of matter, Jan 2018. https://www.jlab.org/about.

[10] Hall D Superconducting Solenoid - Technical Note, Mar 2018. https://halldweb.jlab.org/DocDB/0023/002378/005/sol_note.pdf.

[11] Kapton HN general-purpose polyimide film, Sep 2018. http://www.dupont.com/products-and-services/membranes-films/polyimide-films/brands/kapton-polyimide-film/products/kapton-hn.html.

[12] James Chadwick. Nobel lecture: The neutron and its properties, Aug 2017. http://www.nobelprize.org/nobel_prizes/physics/laureates/1935/chadwick-lecture.html.

[13] Murray Gell-Mann. The eightfold way: A theory of strong interaction symmetry. Technical report, California Institute of Technology, 1961.

[14] David Griffiths. *Introduction to Elementary Particle Physics*. WILEY-VCH, 2010.

[15] K.Okada I. Iizuka and O. Shito. Systematics and phenomenology of boson mass levels. *Prog. Theor. Phys.*, 1966.

[16] C.D. Keith. HallD LH2 Cryotarget, Jan 2014. https://halldweb1.jlab.org/wiki/images/b/b8/HallD_Target_Table.

[17] S. Okubo. ϕ-meson and unitary symmetry model. *Phys. Lett.*, 1963.

[18] Mukesh S. Saini. *Search for new and unusual strangeonia in photoproduction using CLAS.* PhD thesis, Florida State University, 2013.

[19] N. Black T. Barnes and P.R. Page. Strong decays of stange quarkonia. *Physical Review D*, 2003.

[20] A. Somov *et al.* Performance of the pair spectrometer of the gluex experiment. *International Conference on Particle Physics and Astrophysics*, 2015.

[21] B. Aubert *et al. Physical Review D*, 2008.

[22] Bernard Aubert *et al.* (SLAC). *Phys. Rev. D*, 2006.

[23] D. Aston *et al.* (Omega Photon). *Phys. Lett.*, 1981.

[24] E. Pooser *et al.* The GlueX Start Counter Detector. *Nuclear Instruments and Methods in Physics Research Section A: Accelerators, Spectrometers, Detectors and Associated Equipment*, 2018.

[25] F. Mané *et al.* (DM1). *Phys. Lett.*, 1981.

[26] Georges Aad *et al.* Observation of a new particle in the search for the Standard Model Higgs boson with the ATLAS detector at the LHC. *Phys. Lett. B*, 2012.

[27] Gui-Jun Ding *et al.* A candidate for 1– stangeonium hybrid. *Phys. Lett.*, 2007.

[28] H. Al Ghoul *et al.* Measurement of the beam asymmetry Σ for π^0 and η photoproduction on the proton at E_γ=9 GeV. *Phys. Rev. C*, 2017.

[29] J.M. Link *et al.* (FOCUS). *Phys. Lett. B.*, 2002.

[30] K.A. Olive *et al. (Particle Data Group).* Chin. Phys. C, 38, 090001, (2014).

[31] M. Atkinson *et al.* (Omega Photon). *Phys. Lett.*, 1985.

[32] M. Dugger *et al.* Design and construction of a high-energy photon polarimeter. *Nuclear Instruments and Methods in Physics Research Section A: Accelerators, Spectrometers, Detectors and Associated Equipment*, 2017.

[33] M. G. Alekseev *et al.* Observation of a $J^{PC} = 1^+$ exotic resonance in diffractive dissociation of 190 GeV/c π^- into $\pi^-\pi^-\pi^+$. *Phys. Rev. Lett.*, 2010.

[34] R. Kazimi *et al.* Cebaf injector achieved world's best beam quality for three simultaneous beams with a wide range of bunch charges. *Proceedings EPAC 2004*, 2004.

[35] R.R. Crittenden *et al.* A 3000 element lead-glass electromagnetic calorimeter. *Nuclear Instruments and Methods in Physics Research Section A: Accelerators, Spectrometers, Detectors and Associated Equipment*, 1997.

[36] J.J. Thomson. Nobel lecture: Carriers of negative electricity, July 2017. http://www.nobelprize.org/nobel_prizes/physics/laureates/1906/thomson-lecture.html.

[37] G. Zweig. Report no. s419/th412. Technical report, CERN, 1964.

BIOGRAPHICAL SKETCH

Bradford Emerson Cannon was raised in the small and quiet town of New Boston, New Hampshire. He attended New Boston Central School for his elementary education; then continued his education in Goffstown, New Hampshire for middle school and high school. After graduating from Goffstown High School in 2009, he attended the University of New Hampshire where he earned a Bachelor of Science degree in Physics. After graduation, he immediately began his pursue of a Doctoral degree in physics at Florida State University. Upon graduation, he intends to pursue a career in Data Science or Research and Development.